Mapping Ice Sheet Elevation and Elevation Change Using CryoSat-2 Radar Altimetry

Thomas Slater

School of Earth and Environment

University of Leeds

A thesis submitted for the degree of

Doctor of Philosophy

July 2019

Declaration

The candidate confirms that the work submitted is their own, except where work which has formed part of jointly authored publications has been included. The contribution of the candidate and the other authors to this work has been explicitly indicated below. The candidate confirms that appropriate credit has been given within the thesis where reference has been made to the work of others.

The research described in Chapter 2 has been published as: Slater, T., Shepherd, A., McMillan, M., Muir, A., Gilbert, L., Hogg, A. E., Konrad, H., and Parrinello, T.: A new digital elevation model of Antarctica derived from CryoSat-2 altimetry, The Cryosphere, 12, 1551-1562, https://doi.org/10.5194/tc-12-1551-2018, 2018. T. Slater led the study, supervised by A. Shepherd and M. McMillan. A. Muir, L. Gilbert, A. E. Hogg and H. Konrad helped with data processing. All authors commented on the manuscript.

The research described in Chapter 3 has been accepted for publication as: Slater, T., Shepherd, A., McMillan, M., Armitage, T. W. K., Otosaka, T. and Arthern, R.: Compensating changes in the penetration depth of pulse limited radar altimetry over the Greenland Ice Sheet, Transactions in Geoscience and Remote Sensing, https://doi.org/10.1109/TGRS.2019.2928232, 2019. T. Slater led the study, supervised by A. Shepherd and M. McMillan. M. McMillan, T. W. K. Armitage and I. Otosaka helped with data processing. All authors commented on the manuscript.

The research described in Chapter 4 is prepared as a manuscript to be submitted as: Slater, T., Shepherd, A., McMillan, M., Leeson, A., Hogg, A. E., Gilbert, L., Muir, A., Briggs, K.: Seasonal elevation changes in the Greenland Ice Sheet from CryoSat-2 altimetry. T. Slater led the study, supervised by A. Shepherd and M. McMillan. M.McMillan, A. Leeson, A. E. Hogg, L. Gilbert and A. Muir helped with data processing. A. Shepherd and M. McMillan commented on the manuscript.

The research included in Chapter 5 has been published as: Slater, T., Shepherd, A.:

Antarctic ice losses tracking high, Nature Climate Change, https://doi.org/10.1038/s41558-018-0284-9. T. Slater led the study, A. Shepherd commented on the manuscript.

Acknowledgements

This work was funded by the UK Natural Environment Research Council (NERC) and hosted in the Centre for Polar Observation and Modelling (CPOM) at the University of Leeds.

Thank you to my supervisors Andy Shepherd and Mal McMillan for your endless support, advice and encouragement. This thesis has been greatly improved by your contributions — it has been a pleasure to work together over the past four years and I look forward to continuing to do so in the future.

Thank you to the many friends I have met at CPOM for keeping me going, sharing icy knowledge and making coming in to work fun: Anna, Rach, Kate, Hannes, Adriano, Tom, Isobel, Inès and Heather.

Thank you to my examiners Louise Sandberg Sørensen and Piers Forster for their time and effort in reading and examining my thesis.

Mum, Dad, Fay, Josie and Ray — thank you for everything. This is for you.

Abstract

In this thesis I develop novel methods and datasets, based on the processing of CryoSat-2 satellite radar altimeter data, to improve the understanding of retrieving measurements of surface elevation and elevation change over the Antarctic and Greenland ice sheets.

First, I used 6 years of CryoSat-2 altimetry to create a model of the surface height of the Antarctic Ice Sheet and ice shelves. Posted at a resolution of 1 km, 94 % of the grounded ice sheet and 98 % of the floating ice shelves are observed, and the remaining grid cells North of 88 ° S are interpolated using ordinary kriging. Taking into account slope-dependent errors and the distribution of slopes across the ice sheet, I estimated the average accuracy of the DEM to be 9.5 m — a value that is comparable to, or better than that of other models derived from satellite radar and laser altimetry.

Next, I developed a new technique to retrieve estimates of the depth distribution of radar backscatter from CryoSat-2 altimeter waveforms using a backscatter model. I then applied this model to chart spatial and temporal variatibility in radar backscatter and, for the first time, explicitly estimate radar penetration depth across the interior of the Greenland Ice Sheet. I then used this information to correct for artefacts in elevation trends derived from Cryosat-2 pulse-limited altimetry resulting from an episodic melt event which reset the radar scattering horizon. Incorporating the penetration depth into the surface height retrieval, I find improved agreement when compared to independent airborne laser altimeter data recorded over the same time period.

Finally, I used CryoSat-2 altimetry to estimate seasonal elevation changes in

the Greenland Ice Sheet. Using regional climate model simulations of height fluctuations due to surface process alone, I demonstrate that CryoSat-2 observations track elevation changes driven by melting and snowfall accumulation in the ice sheet ablation zone. I then mapped spatial and temporal variations in seasonal elevation change, demonstrating the ability of CryoSat-2 to monitor changes in Greenland which arise due to its meteorology.

Abbreviations

ACC	Antarctic Circumpolar Current
ATM	Airborne Topographic Mapper
AW	Atlantic Water
CDW	Circumpolar Deepwater
DEM	Digital Elevation Model
GIA	Glacial Isostatic Adjustment
IMAU-FDM	Institute for Marine and Atmospheric Research Utrecht Firn Densification Model
IW	Irminger Water
LRM	Low Resolution Mode
NAC	North Atlantic Current
NAO	North Atlantic Oscillation
OCOG	Offset Center of Gravity
POCA	Point of Closest Approach
PIG	Pine Island Glacier
PRF	Pulse Repetition Frequency
RLA	Riegl Laser Altimeter
RMS	Root Mean Square
SAR	Synthetic Aperture Radar
SARIn	Synthetic Aperture Radar Interferometric
SIRAL	Synthetic Aperture Interferometric Radar Altimeter
SMB	Surface Mass Balance
TCOG	Threshold Offset Center of Gravity

Contents

List of Figures

List of Tables

Chapter 1

Introduction and background

Here I introduce Earth's principal ice sheets — Antarctica and Greenland — and the importance of continued monitoring in understanding their evolution and informing appropriate climate policy. In the first part of the chapter, I review the current mass balance of Earth's ice sheets, and provide an overview of the satellite techniques used to measure them. I then examine how interactions with the ocean and with the atmosphere, and processes at the ice sheet base, affect ice sheet surface elevation, and I summarise recent observations of ice sheet change. I then provide a more focussed description of the principles of satellite radar altimetry — the technique that forms the basis of this thesis — to measure ice sheet surface height and height trends, and the challenges associated with observing land ice in this way.

1.1 Factors affecting changes in ice sheet elevation and mass

The Antarctic and Greenland ice sheets hold enough water to raise global sea levels by 58 m and 7 m, respectively (Fretwell et al., 2013; Morlighem et al., 2017). Ice losses from both ice sheets have increased over the past three decades (Shepherd et al., 2012; The IMBIE Team, 2018); of the 3.2 ± 0.4 mm/yr sea level rise measured between 1993 and 2010, Antarctica and Greenland have contributed 0.27 ± 0.11 mm/yr and 0.33 ± 0.08 mm/yr , respectively (Church et al., 2013). Since then, the observed sea level contribution has risen to 0.61 ± 0.12 mm/yr from Antarctica between 2012 and 2017 (The IMBIE Team, 2018), and 0.79 ± 0.06 mm/yr from Greenland between 2010 and 2018

(Mouginot et al., 2019). As key components of the global sea level budget, continued monitoring of Earth's polar ice sheets is significant in allowing policymakers to plan climate change adaptations with confidence (Shepherd and Nowicki, 2017; Slater and Shepherd, 2018).

Changes in the mass of grounded ice sheets arise primarily because of fluctuations in ice flow into the ocean (e.g. (Joughin et al., 2010; Mouginot et al., 2014)), snowfall accumulation (e.g. (Davis et al., 2005; Medley and Thomas, 2019)) and runoff of surface meltwater (e.g. (Enderlin et al., 2014; van den Broeke et al., 2016)). Mass loss in Antarctica is governed by ice flow into the ocean and is accelerating: between 1992 and 2017, rates of ice loss from Antarctica increased from 49 $\pm$ 67 Gt/yr to 219 $\pm$ 43 Gt/yr (The IMBIE Team, 2018). The Greenland Ice Sheet lost mass at an average rate of 142 $\pm$ 49 Gt/yr between 1992 and 2011 (Shepherd et al., 2012), which increased to 269 $\pm$ 51 Gt/yr between 2011 and 2014 (McMillan et al., 2016). This increase has been mainly driven by widespread surface melting owing to changes in atmospheric circulation enhancing warming in the summer months (Trusel et al., 2018; van den Broeke et al., 2016).

Ice imbalance can be determined through satellite observations of changes in (1) ice sheet surface elevation (e.g. (McMillan et al., 2016, 2014)) (2) ice flow (e.g. (Rignot et al., 2019, 2011; van den Broeke et al., 2009)) and (3) gravitational attraction (e.g. (Forsberg et al., 2017)). Estimates of ice sheet mass balance derived from these techniques agree when used over equivalent spatial and temporal domains, and with common surface mass balance and glacial isostatic adjustment models (The IMBIE Team, 2018). Uniquely, satellite altimeter measurements of elevation change are capable of resolving patterns of imbalance at a high spatial (kilometre scale) resolution, and provide measurements at approximately monthly temporal sampling over multi-decadal timescales, allowing short-term variability to be separated from long-term trends (e.g. (Konrad et al., 2017; Schröder et al., 2019; Shepherd et al., 2018, 2019)). In addition to quantifying ice sheet mass balance, observations from satellite altimeters have improved our understanding of the geophysical processes which can bring about ice sheet elevation change: meteorology (e.g. (McMillan et al., 2016; Shepherd et al., 2012)), ice dynamics (e.g. (Flament and Rémy, 2012; Konrad et al., 2017; Shepherd et al., 2002)),

subglacial hydrology (e.g. (McMillan et al., 2013; Siegfried and Fricker, 2018)) and vertical motion of the underlying bedrock in response to ice unloading (e.g. (Barletta et al., 2018; Riva et al., 2009)). In the following sections I review studies of each of these processes in turn, and summarise recent observations of ice sheet change.

1.1.1 Ice dynamics

In recent years, a number of marine-terminating ice streams in Antarctica have accelerated (Hogg et al., 2017; Joughin et al., 2003; Rignot, 2001) and thinned (McMillan et al., 2014; Schröder et al., 2019; Shepherd et al., 2019, 2002). Since 1992 the thinning of grounded ice has predominantly occurred in glacier systems draining West Antarctica into the Amundsen and Bellingshausen Seas, where warm Circumpolar Deepwater intrudes onto the continental shelf and melt ice shelves at their base (Jacobs et al., 2011; Paolo et al., 2015; Shepherd et al., 2004) (Figure 1.1), reducing lateral traction (buttressing) and accelerating ice flow (Pritchard et al., 2012; Shepherd et al., 2004). In addition, ocean-driven melting has caused widespread retreat of the grounding line (the boundary between grounded and floating ice along the sea floor, Figure 1.2) (Konrad et al., 2018; Park et al., 2013), which also destabilises grounded ice inland, causing speedup, ice drawdown, and the thinning of the glacier upstream. Dynamically induced surface lowering due to changes in oceanic forcing has been observed hundreds of kilometres inland from the grounding line (Flament and Rémy, 2012; Shepherd et al., 2002, 2001); long-term time series of surface elevation change available in the multi-mission satellite altimeter record allows the onset and speed at which thinning propagates inland to be determined and the response of individual neighbouring glaciers to be investigated (Konrad et al., 2017). For example, 25 years of satellite altimeter observations have shown that 24 % of the West Antarctic Ice Sheet (415,000 km^2) is now in a state of dynamical imbalance (Shepherd et al., 2019). At the Antarctic Peninsula, rapid regional atmospheric warming, in tandem with ocean-driven melting, has caused ice shelf collapse (Cook and Vaughan, 2010; Scambos et al., 2013; Shepherd et al., 2003; van den Broeke, 2005) and surging of contiguous glaciers as a consequence of reduced ice shelf buttressing (De Angelis and Skvarca, 2003; Rignot et al., 2004).

Dynamic ice losses in Greenland are localised to several marine-terminating glaciers which have recently accelerated (Joughin et al., 2014; Rignot and Kanagaratnam, 2006)

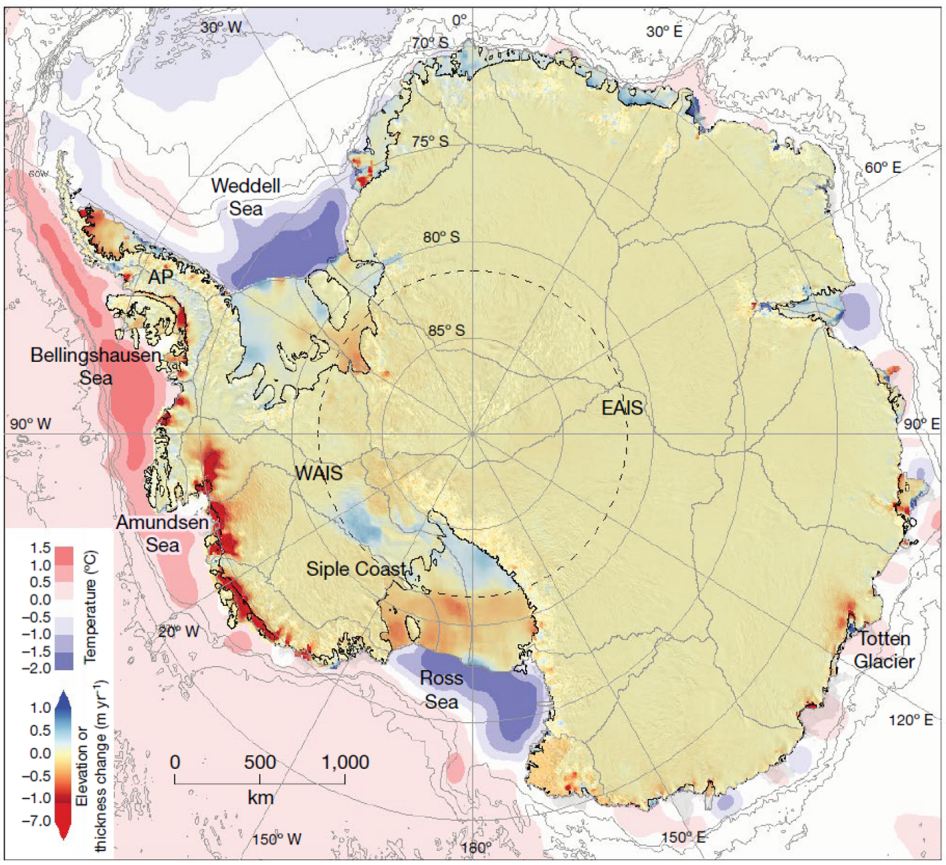

Figure 1.1: Average trend in elevation and thickness of the grounded Antarctic Ice Sheet and floating ice shelves, respectively, determined from repeat satellite radar altimetry between 1992 and 2017 north of 81.5 ° S (dashed grey circle), and between 2010 and 2017 everywhere else. Also shown is the estimated ocean temperature at the sea floor. Extracted from (Shepherd et al., 2018).

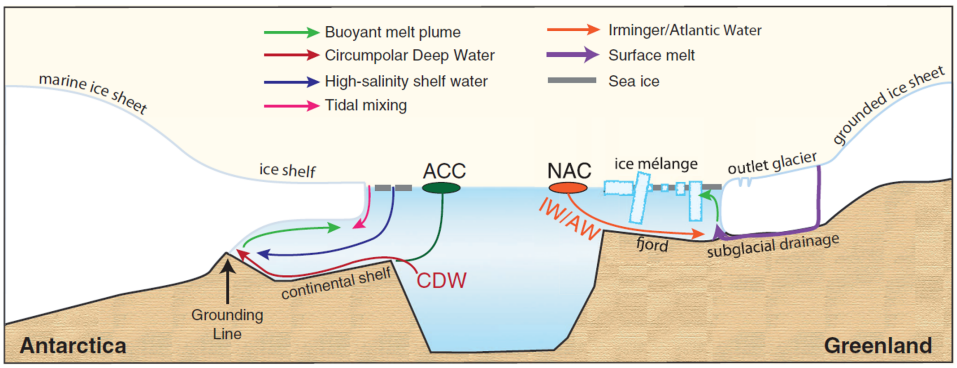

Figure 1.2: Schematic of ocean processes influencing ice shelves and outlet glaciers. Melting beneath ice shelves in Antarctica (left) occurs through (1) the formation of high-salinity water near the ice shelf front during winter sea ice growth, (2) tidal mixing of seasonally warm water and (3) the intrusion of warm Circumpolar Deepwater (CDW) from the Antarctic Circumpolar Current (ACC). Ocean melting of outlet glaciers in Greenland (right) is similarly caused by the influx of warm Irminger Water (IW) and Atlantic Water (AW) masses, which originate from the North Atlantic Current (NAC). Extracted from (Joughin et al., 2012).

and thinned (Helm et al., 2014; McMillan et al., 2016; Nilsson et al., 2016; Sandberg Sørensen et al., 2018) as a result of recent changes in coastal ocean circulation bringing warm water into glacier fjords (Figure 1.2) (Holland et al., 2008; Seale et al., 2011), reducing resistive stresses through calving front retreat (Bondzio et al., 2017). Pronounced changes in ice speed and surface elevation have been observed at many marine-terminating glaciers in Greenland (King et al., 2018), perhaps most notably at Jakobshavn Isbræ, which is particularly susceptible to oceanic conditions in the deep fjord it feeds (Holland et al., 2008) and has slowed since 2016, after two decades of acceleration and thinning (Khazendar et al., 2019). When compared to Antarctica, atmospheric temperatures across Greenland are relatively high and surface melting in the summertime influences ice flow on a variety of timescales through basal lubrication (Hanna et al., 2012; Lemos et al., 2018; Zwally et al., 2002). Elsewhere, surface meltwater drainage has been linked to changes in ice velocity: inducing both seasonal speedup in glaciers through basal lubrication (Hoffman et al., 2011; Zwally et al., 2002), and interannual slowdown in land-terminating sectors where it is concluded that efficient

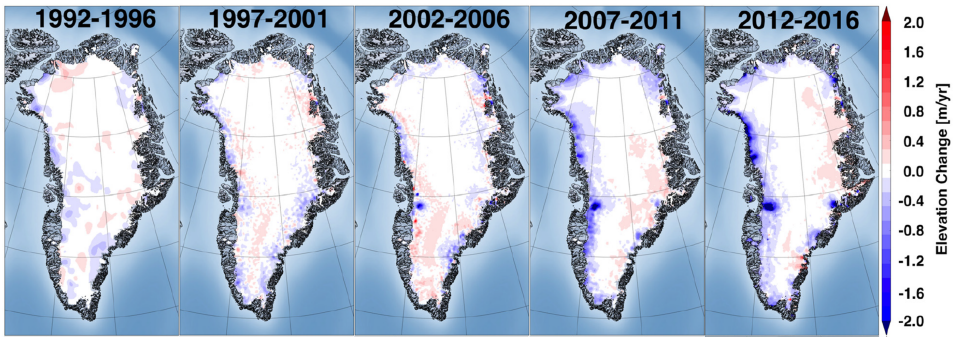

Figure 1.3: Average trend in surface elevation of the Greenland Ice Sheet determined from repeat satellite radar altimetry, determined over successive 5 year periods between 1992 and 2016. Extracted from (Sandberg Sørensen et al., 2018).

subglacial drainage systems have evolved (Sundal et al., 2011; Tedstone et al., 2015).

1.1.2 Meteorology

In addition to dynamic processes and basal melting, ice sheets change in mass due to increases in precipitation (snow, rain) and ablation (surface melt runoff, wind erosion, sublimation), respectively. The net balance between these two processes is defined as the surface mass balance (SMB). In Antarctica, snowfall is the largest component of the SMB (Boening et al., 2012; Medley et al., 2018); sublimation and drifting snow erosion remove a small percentage of surface mass gains, and spatially integrated surface runoff is close to zero as almost all meltwater refreezes locally (Lenaerts et al., 2012). Satellites have demonstrated their ability to resolve mass gains due to large meteorological events, for example between 2009 and 2012, extreme snowfall deposited around 200 Gt of additional mass in Dronning Maud Land, equivalent to the mean annual snow accumulation in this sector (Lenaerts et al., 2013; Shepherd et al., 2012).

In contrast, trends in surface mass changes in Greenland have been largely driven by surface meltwater runoff, which accounts for the majority (60 %) of the total ice loss since 1991 (van den Broeke et al., 2016). Between 2008 and 2013, a series of anomalously warm summers (Hanna et al., 2012; van Angelen et al., 2014) promoted widespread episodes of surface melting (Enderlin et al., 2014; Nghiem et al., 2012;

Tedesco et al., 2013) and corresponding thinning in the ice sheet margins (McMillan et al., 2016; Sandberg Sørensen et al., 2018; Simonsen and Sørensen, 2017) (e.g. Figure 1.3). Recent changes in atmospheric forcing have tracked the phase of the North Atlantic Oscillation (NAO), which in its negative phase advects southerly air over west Greenland, enhancing warming and reducing snowfall (Ahlstrøm et al., 2017; Fettweis et al., 2013). Between 2013 and 2016, an abrupt shift to a positive phase of the NAO brought about cooler atmospheric conditions and a reduction in ice losses (Bevis et al., 2019)).

1.1.3 Ice sheet hydrology and basal processes

Satellite observations have resolved coherent regions of ice uplift and subsidence as a result of the episodic movement of water underneath the Antarctic Ice Sheet (e.g. (Fricker et al., 2007; McMillan et al., 2013; Siegfried and Fricker, 2018; Smith et al., 2009; Wingham et al., 2006c)). Subglacial lake drainage induces elevation changes of the order of several metres over tens of square kilometres and sub-decadal timescales (e.g. Figure 1.4), indicating the movement of large volumes of water. For example, a single subglacial lake in East Antarctica was observed to discharge 6 Gt of water during a 20 month period between 2007 and 2009 (McMillan et al., 2013); it is estimated that 65 Gt of water is generated annually in Antarctica through subglacial melting (Pattyn, 2010). In such drainage events, water can be exchanged between other subglacial lakes (e.g. (Wingham et al., 2006c)), or routed to the ice sheet margin and into the ocean, raising sea levels (Siegert et al., 2007). Satellite altimeters have now mapped over a hundred active subglacial lakes in Antarctica (Smith et al., 2009) with some being monitored for over a decade (Siegfried and Fricker, 2018), revealing that the subglacial water system can enhance ice flow through basal lubrication (Bell et al., 2007; Stearns et al., 2008). Although a well-established component of the basal hydrological system of the Antarctic Ice Sheet, the first subglacial lakes were not reported in Greenland until 2013, fed by surface meltwater and formed in regions of inefficient subglacial drainage (Palmer et al., 2013). Recent observations of collapse basins tens of metres deep and over areas of 2 km^2 below the equilibrium line have provided evidence of long-term storage and the sudden drainage of meltwater below the Greenland Ice Sheet (Howat et al., 2015; Palmer et al., 2015).

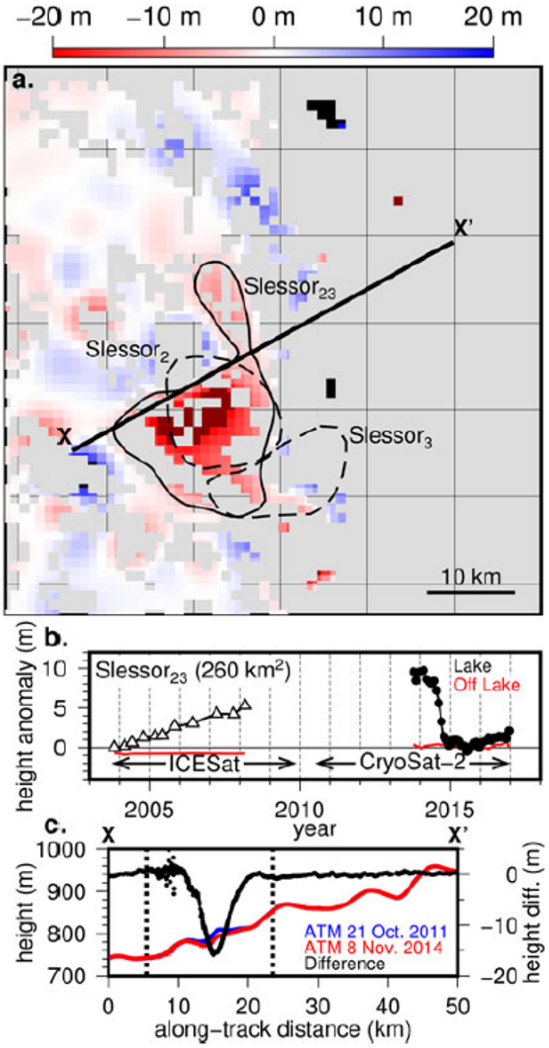

Figure 1.4: Subglacial lake drainage at Slessor Glacier, Antarctica. (a) Relative height change between December 2013 and March 2014, and November 2014 and February 2015 at Slessor_2 and Slessor_3 subglacial lakes. (b) Height change time series from IceSat (triangles) and CryoSat-2 (circles) satellite altimetry. (c) Heights from Operation IceBridge laser altimetry in October 2011 (blue) and November 2014 (red) along the profile X-X'. Extracted from (Siegfried and Fricker, 2018).

In addition to basal hydrology, measurements of ice sheet thickness are affected by vertical motion of the underlying bedrock, which deforms due to a combination of the delayed viscoelastic response to past deglaciation, and the instantaneous elastic response to present day ice loss (Peltier, 1974). Glacial Isostatic Adjustment (GIA) is the vertical uplift of the solid Earth previously burdened by ice at the Last Glacial Maximum: in Antarctica and Greenland, present day surface height changes due to GIA occur at rates in the order of millimetres per year (Milne et al., 2018; Riva et al., 2009). In regions of rapid ice loss, for example in the Amundsen Sea Embayment of West Antarctica, the instantaneous elastic rebound of the solid Earth causes rapid uplift of the order of tens of millimetres per year (Barletta et al., 2018), and has the potential to delay or prevent unstable ice sheet retreat Konrad et al. (2015). Uplift of the solid Earth will cause uplift of the overlying ice column; the total ice sheet surface elevation change can be attributed to a combination of the solid Earth deformation and ice volume change (i.e. the surface elevation would still increase even if there were no change in ice volume) (Wahr et al., 2000). As a result, the vertical motion of the bedrock must be considered when estimating ice sheet mass balance from satellite altimeters (Shepherd et al., 2012); this is typically achieved using modelled estimates of the solid Earths' viscoelastic response (e.g. (A et al., 2012; Whitehouse et al., 2012)).

1.2 Altimetric principle

Satellite radar altimeters utilise the ability of microwave systems to transmit large-power pulses which actively illuminate the target surface and measure precise echo-delay timings. Transmitting at microwave frequencies allows the signal to penetrate through clouds, and be independent of solar illumination.

1.2.1 Range measurement

Radar altimeters transmit a pulse of duration t at nadir, which will travel at close to the speed of light, c, through Earth's atmosphere. The two-way range distance from the antenna to target and back is therefore:

$$R_{two-way} = ct \tag{1.1}$$

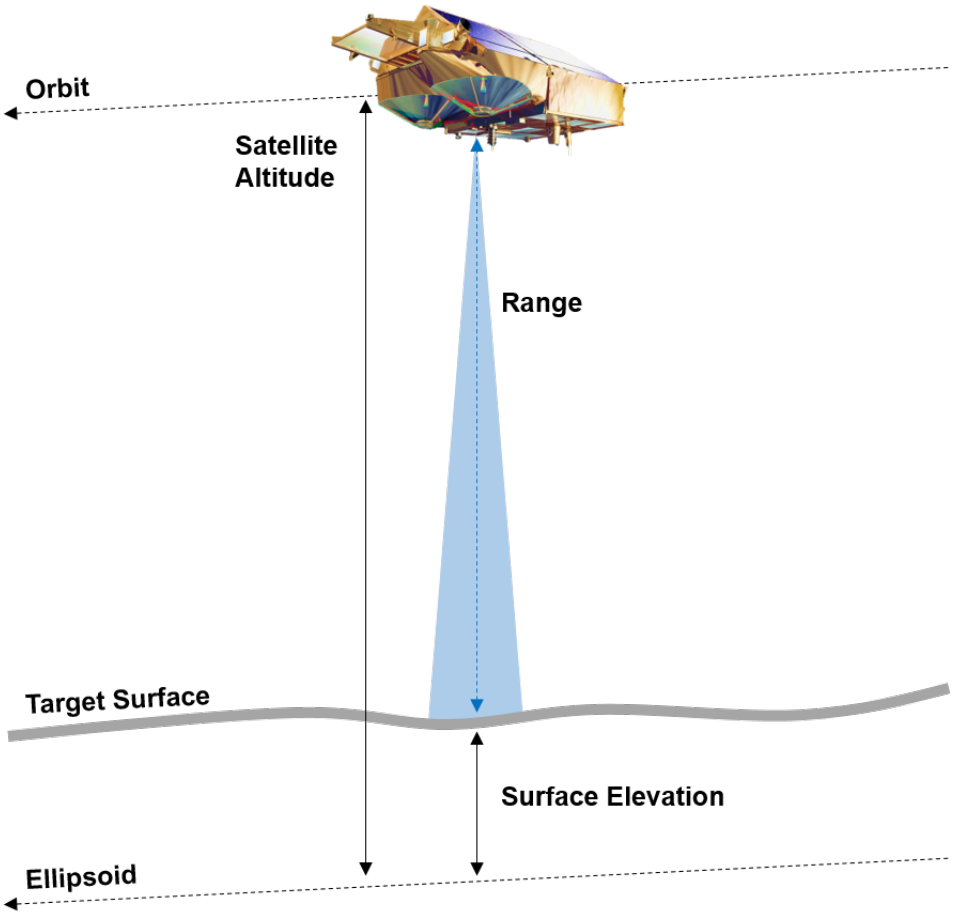

Figure 1.5: Schematic of basic principle and geometry of a satellite radar altimeter.

And the range distance to the target (satellite-to-surface) is half of this:

$$R = \frac{ct}{2} \tag{1.2}$$

The elevation of the target E is then determined by removing the range from the satellite's altitude A with respect to a reference ellipsoid (a mathematical approximation of Earth's surface) (Figure 1.5):

$$E = A - R \tag{1.3}$$

The resolution at which an altimeter is able separate the range between two point targets is dependent on the pulse duration τ, and can be improved through the use of chirped pulses which sweep a signal over a small range (Bandwidth, B) of frequencies, allowing individual returns to be more precisely located within the received signal (Woodhouse, 2005):

$$\Delta R = \frac{c\tau}{2} = \frac{c}{2B} \tag{1.4}$$

In this way, satellite altimeters can be precise to a few centimetres whilst orbiting approximately 800 km above Earth. The accuracy of the range measurement is limited by knowledge of the instrument location, the precision with which the scattering horizon can be determined within the echo, and factors affecting the delay time, which include variability in the speed of light as it propagates through the ionosphere and troposphere (Fu and Cazenave, 2001).

1.2.2 Ground footprint

Spaceborne radar altimeters have a large beam-limited footprint, F_b which is dependent on the satellite altitude and antenna beam width, θ:

$$F_b = 2Atan\left(\frac{\theta}{2}\right) \tag{1.5}$$

A satellite altimeter operating at an altitude of $\sim$ 800 km with a beam width of $\sim 1\,^{\circ}$ will illuminate a $\sim$ 14 km diameter footprint on the ground. Altimeters transmit a spherical pulse as a beam of increasing radius as it travels towards Earth. Since altimeters measure time delay and operate at nadir, it can be assumed (for a flat Earth) that the initial backscattered power will come from directly below the instrument: therefore the measured footprint is determined by the duration of the emitted pulse. This reduced

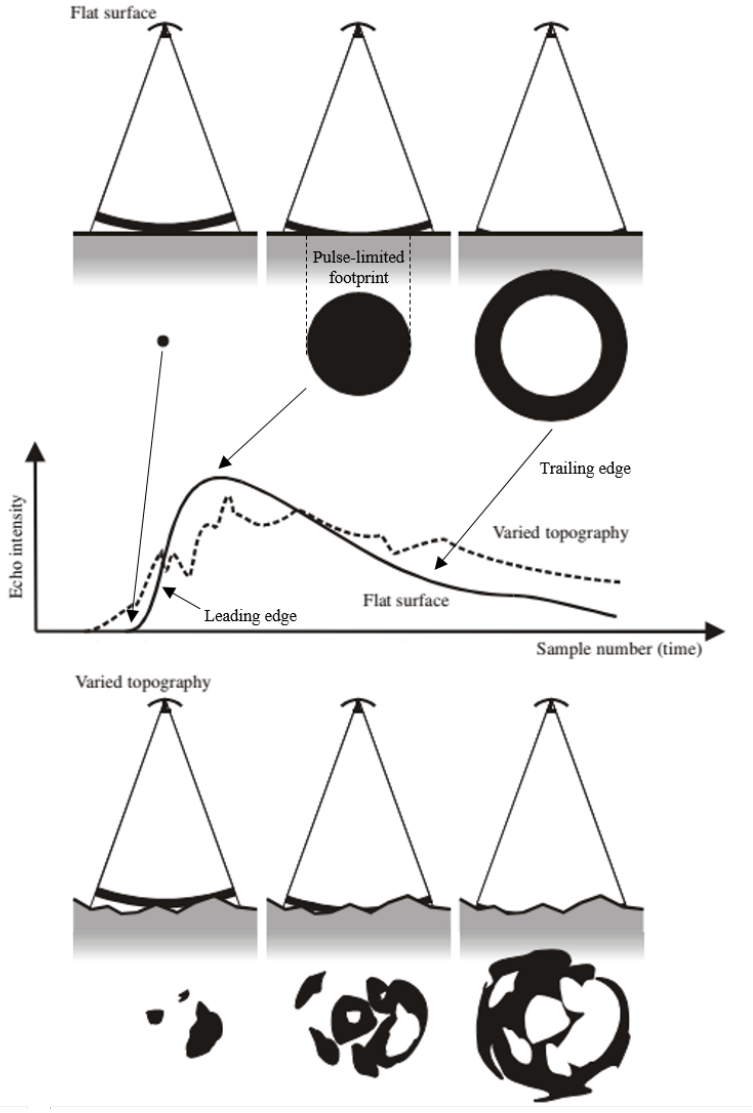

Figure 1.6: Development of a radar pulse over (top) an ideal non-penetrating planar surface and (bottom) a non-penetrating rough surface (e.g. a rough ocean), and correspondence to waveform shape. Adapted from (Woodhouse, 2005).

pulse-limited footprint F_p (Figure 1.6) is defined as the surface area illuminated by the leading edge (front) of the pulse before the trailing edge (rear) reaches the surface:

$$F_p = \sqrt{Ac\tau} = \sqrt{\frac{Ac}{B}} \tag{1.6}$$

An altimeter operating with $F_b > F_p$ is defined as being pulse-limited; a typical pulse-limited footprint is $\sim$ 2 km over a flat surface. The altimeter echo (or waveform) is the sum of scattering contributions from all surface and subsurface features illuminated within the ground footprint.

1.2.3 Radar altimeter waveforms

Satellite altimeters record the signal reflected from Earth's surface within a fixed 'analysis window'. Because the elevation of the target surface is not known, this period is defined by the on-board tracker to ensure the returned signal remains centred in range and power within this window. During the analysis window, an altimeter records the distribution of backscattered power as a function of time, binned into a number of range gates. From this power distribution — or 'waveform' — the range to the surface can be determined. Over an idealised flat, non-penetrating surface the waveform has a characteristic shape (Figure 1.6). The spherical pulse illuminates a circular region of linearly increasing area, until the trailing edge of the pulse interacts with the surface. At this time the illuminated area is defined as the pulse-limited footprint. When the trailing edge intersects the surface, the waveform reaches its peak power and begins to decay. From this point the illuminated region is an annulus which expands outwards towards the edge of the beam footprint (the trailing edge). Although the area of the annulus is constant, the returned power is attenuated by antenna pattern.

1.2.4 Impact of surface and volume scattering

In addition to the range, the altimeter waveform also contains information regarding the scattering properties of the target surface. Over homogeneous non-penetrating scattering surfaces (e.g. ocean), the shape of the altimeter echo is governed by the shape of the original pulse, and the scattering characteristics and height variations of the target surface within the footprint. A given waveform can be described as the

convolution of three functions:

$$P_R(t) = P_T(t) * P_{FS}(t) * P_d(t) \tag{1.7}$$

where $P_R(t)$ is the pulse received at the antenna as a function of time, t, $P_T(t)$ is the transmitted pulse shape, $P_{FS}(t)$ is the flat surface response and $P_d(t)$ is the height distribution of local scatterers and their scattering properties (Brown, 1977).

Over increasingly rough surfaces, where there is more height variability within the radar footprint, energy is scattered in diffuse directions and the echo shape deviates from the idealised flat surface return (Figure 1.6). In such cases it is unclear which delay time corresponds to the surface height, as the leading edge is no longer at nadir. Over the ocean, height variations are the main influence on waveform shape. Height variability reduces the slope of the leading edge (e.g. Figure 1.6); the width of the leading edge is proportional to the root-mean square height of the surface. Over ice sheets, the microwave frequencies typically used by satellite radar altimeters will penetrate into the snowpack — therefore the echo shape is a combination of surface and volume scatterers (Ridley and Partington, 1988) dependent on the surface topography and roughness, and on the scattering properties of the snowpack (controlled by e.g. snow grain size, density, liquid water content) (Matzler, 1996). The degree of penetration can be characterised by the slope of the trailing edge.

1.2.5 Waveform retracking and elevation retrieval

Over topographic surfaces — and in particular over Earth's ice sheets — the received waveform is misaligned relative to the nominal tracking point defined by the on-board tracker. To precisely measure the surface elevation it is necessary to compute the offset between the nominal tracking point and waveform leading edge (the power returned from the surface): this process is called retracking. To determine the offset, retracking algorithms fit models to altimeter waveforms in order to identify an instrument-independent position on the leading edge which corresponds to the range of the illuminated surface. The retracking of pulse-limited altimeter echoes can be broadly split into two categories: empirically- (e.g. (Davis, 1997; Helm et al., 2014; Martin et al., 1983; Nilsson et al., 2016; Wingham et al., 1986)) and physically-based (e.g. (Legrésy et al., 2005; Legrésy and Rémy, 1997)).

Physically-based retrackers include a theoretical model which describes the altimeter return, accounting for the interaction of the microwave pulse with the scattering properties of the target surface. Over oceans this response can be described through a convolution of the height probability density of scatterers, the flat surface impulse response and transmitted pulse shape (e.g. Equation 1.7 (Brown, 1977)). Over ice sheets a theoretical description of the radar return is more challenging due to scattering from (1) slope and rugged terrain within the footprint and (2) penetration of the pulse into the snowpack (Ridley and Partington, 1988).

As a result, empirically-based retrackers are more commonly applied to ice sheet echoes. Examples of empirical retrackers include (1) the Offset Centre of Gravity (OCOG) retracker, which locates the true centre of the waveform within the analysis window and assumes the leading edge to lie half the echo width to the left Wingham et al. (1986) and (2) threshold retrackers, which determine the retracking point according to a predefined threshold of the peak power (e.g. (Davis, 1997; Helm et al., 2014; Nilsson et al., 2016)). Empirical retrackers are designed to be adaptable to a wide variety of pulse shapes and provide a solution which is robust to echo variations induced by ice sheet topography and variable snowpack scattering properties. This is key when measuring elevation change, as it is important to use an algorithm that is consistent in its derivation of the retracking offset (Davis, 1997; Helm et al., 2014). The optimal retracking approach is still an open area of research: despite being less sensitive to variations in snowpack scattering properties, by focussing on the first leading edge threshold algorithms do not appropriately consider complex multi-peaked waveforms which can be returned from areas of complex terrain (e.g. subglacial lakes).

1.2.6 Correcting for the effects of surface slope

Over sloped or undulating surfaces the first signal returned is not reflected from nadir, but from the point of closest approach (POCA) relative to the satellite. This point will be located off-nadir and up-slope; the lateral offset is proportional to the magnitude of the slope and is in the direction of the steepest gradient. Ice sheet surface slopes are large enough to laterally displace the POCA by several kilometres, inducing a height error in the order of up to 100 m (Brenner et al., 1983). For conventional pulse-limited

altimetry three techniques are commonly used to correct for slope-induced height errors: the direct method (Brenner et al., 1983), the intermediate method (Rèmy et al., 1989) and the relocation method Bamber (2004) (Figure 1.7). Each technique uses external data to determine the surface slope magnitude and direction. The direct method calculates a range correction based upon the surface slope between the POCA and nadir (Figure 1.7a). Instead of correcting the range, the intermediate method finds the off-nadir location on the surface which corresponds to the measured range (Figure 1.7b). The relocation method uses slope information to estimate the location of the POCA and determines the surface elevation at that point (Figure 1.7c). In each case the error is primarily associated with the quality of the slope information used. Although height errors cancel out when determining elevation changes from repeat measurements, as the magnitude of the slope correction is time-invariant, these measurements are in the wrong locations and lead to an underestimation of area-integrated estimates (Hurkmans et al., 2012). As such, the relocation method can be considered the preferable approach, as it represents the true measurement location; however, it can result in inhomogeneous data sampling as altimeters tend to oversample elevated regions in comparison to topographic depressions (Bamber et al., 1998). Recent improvements to slope correction methods use external Digital Elevation Models, accounting for the topography within the beam-limited footprint, to determine the POCA and associated range correction (Roemer et al., 2007).

1.2.7 Synthetic aperture radar altimetry

Exploiting concepts used by synthetic aperture radar (SAR) imagers, SAR (or delay/Doppler) altimeters utilise Doppler shifts in the frequency of the echo, caused by the forward movement of the satellite, to reduce the along-track footprint size to ~ 300 m (Raney, 1998). In the across-track plane, the footprint size is the same as the pulse-limited footprint. Compared to conventional pulse-limited altimeters, SAR altimeters emit phase-coherent pulses at a higher rate (~ 18 kHz compared to ~ 2 kHz); a Fast Fourier Transform applied to the received signal from each burst (a series of consecutive pulses) separates the conventional beam-limited footprint into multiple synthetic beams in the along-track direction according to their Doppler frequency (Figure 1.8). In a process known as 'multi-looking', echoes from beams directed in the same location from successive bursts are incoherently summed to reduce radar speckle (Wingham

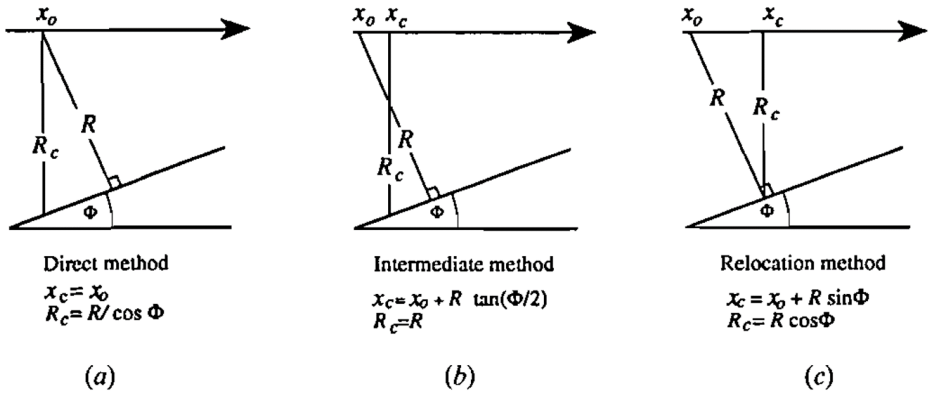

Figure 1.7: Illustration of (a) direct, (b) intermediate and (c) relocation slope correction methods used in conventional pulse-limited altimetry. In each case, x_0 and R are the initial satellite position along-track and range, respectively, and x_c and R_c are the corrected along-track position and range, respectively. Extracted from (Bamber, 2004).

et al., 2006a). As a result of the multi-looking processing, the flat surface response of a SAR altimeter has an impulse-like shape (Figure 1.8e).

1.3 The CryoSat-2 mission

Launched in 2010, CryoSat-2 is the first satellite capable of performing SAR altimetry over the cryosphere (Wingham et al., 2006a). Operating at an orbital inclination of 92 °, CryoSat-2 observes to latitudes of ± 88 °: closer to the poles than previous missions which were originally developed to measure the ocean geoid (Table 1.3). As a result of this unique long-period, drifting orbit (369-day repeat period with a 30-day subcycle) CryoSat-2 provides uniform coverage of the of the Arctic Ocean and Antarctic continent each month, with a high orbit cross-over density at polar latitudes compared to previous altimeters (Wingham et al., 2006a).

The main payload — the Synthetic Aperture Interferometric Radar Altimeter (SIRAL) — is a normal incidence, Ku band (13.6 GHz) radar altimeter, comprising of two nadir looking antennas separated by 1 m in the across-track direction (Wingham et al., 2006a). SIRAL operates in three modes, each suited for observing particular terrain

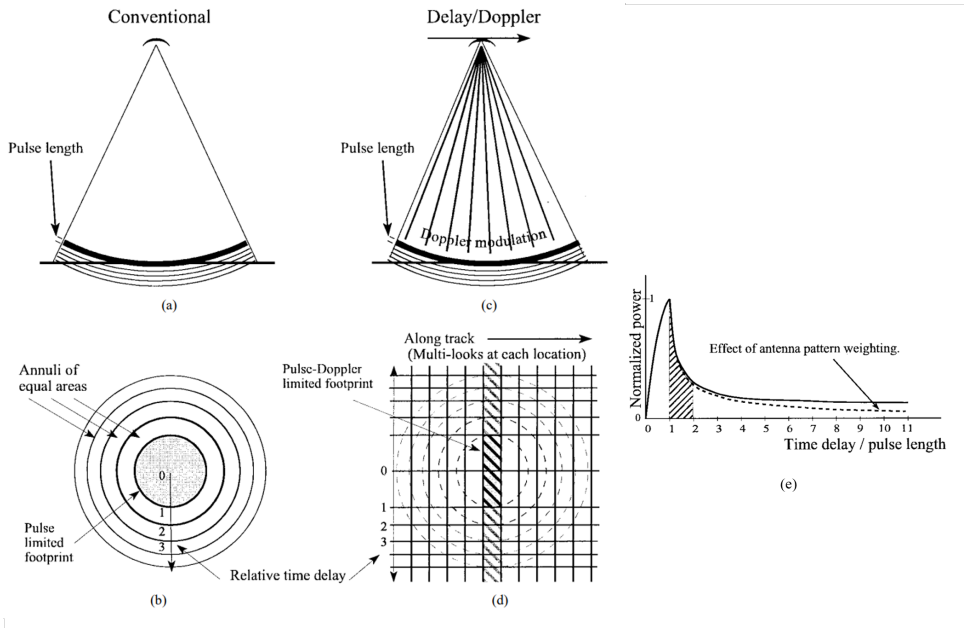

Figure 1.8: Illumination geometry in side view for (a) conventional pulse-limited and (c) synthetic aperture radar altimetry, and footprint plan view for (b) pulse-limited and (d) synthetic aperture radar altimetry. (e) Typical flat surface response waveform for a synthetic aperture radar altimeter. Adapted from (Raney, 1998).

(Figure 1.9). Over open oceans and the interior of the Antarctic and Greenland ice sheets, where the surface topography is relatively smooth, CryoSat-2 operates in low resolution mode (LRM), using a single antenna as a conventional pulse-limited altimeter (Section 1.2). In LRM, like earlier altimeters, CryoSat-2 uses a relatively low pulse repetition frequency (PRF) (2 kHz) and incoherent averaging to reduce instrument noise and radar speckle; the pulse-limited footprint over a flat surface is $\sim$ 1.6 km (Wingham et al., 2006a). Over Earth's sea ice and coastal regions CryoSat-2 operates in SAR mode, using a single antenna as a SAR altimeter (Section 1.2.7): an increased PRF of 20 kHz allows delay-Doppler processing and multi-looking of coherent echoes to reduce the along-track footprint to $\sim$ 300 m (Wingham et al., 2006a). This allows CryoSat-2 to better resolve sea ice leads and floes when compared to previous pulse-limited altimeters (e.g. (Tilling et al., 2018)).

Over complex terrain found in ice sheet margins, ice caps and mountain glaciers,

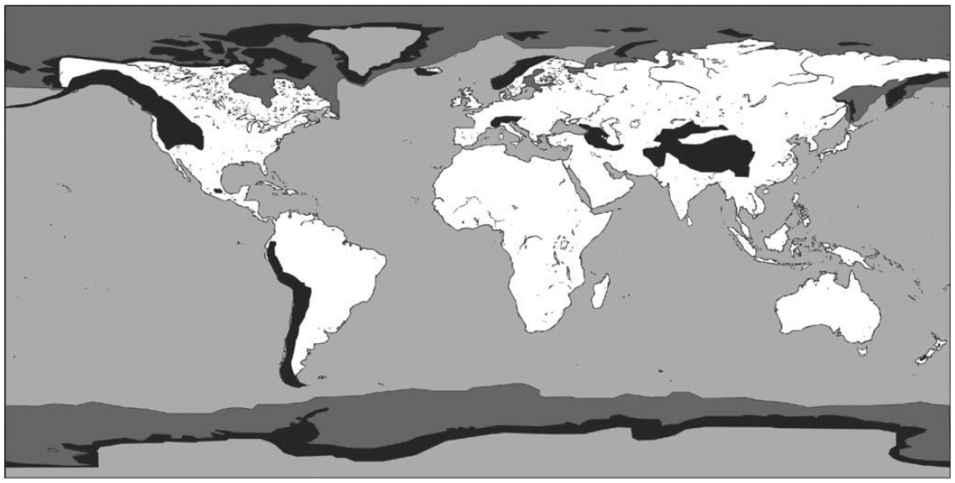

Figure 1.9: Example of SIRAL mode acquisition mask. SARIn mode areas are highlighted in black, SAR mode dark grey and LRM in light grey. Extracted from (Wingham et al., 2006a).

Satellite/mission	Dates of operation	Ground spatial coverage (degree latitude)	Frequency band	Operating mode	Repeat period (days)
Seasat	1978	± 72	Ku	Pulse-limited	3
GeoSat	1985-1986	± 72	Ku	Pulse-limited	17.5
ERS-1	1991-1996	± 81.5	Ku	Pulse-limited	35*
ERS-2	1992-2011	± 81.5	Ku	Pulse-limited	35
Envisat	2002-2012	± 81.5	Ku	Pulse-limited	35
CryoSat-2	2010 - present	± 88	Ku	Pulse-limited/SAR	369 (30 sub-cycle)
AltiKa	2013 - present	± 81.5	Ka	Pulse-limited	35**
Sentinel-3	2016 - present	± 81.35	Ku	SAR	27

*Followed other orbits with repeat cycles of 3 days and 168 days.

**Switched to drifting orbit in 2015.

Table 1.1: Summary of satellite radar altimeters used to monitor Earth's cryosphere.

CryoSat-2 operates in SAR interferometric (SARIn) mode. In SARIn mode, CryoSat-2 utilises the same along-track processing as in SAR mode. In addition, the second receive antenna is used to perform interferometry: differences in path lengths detected by each antenna, induced by off-nadir scatterers, allow the echo to be precisely located in the across-track plane — negating the need for external slope information to determine the slope-induced error (Jensen, 1999).

Nearly 9 years after launch, CryoSat-2 has successfully met its mission objectives, providing data that has been fundamental to our understanding of recent changes in Arctic sea ice thickness and volume (e.g. (Laxon et al., 2013; Ricker et al., 2015; Tilling et al., 2016, 2015)), and in Antarctic and Greenland elevation and mass (e.g. (Helm et al., 2014; McMillan et al., 2016, 2014; Nilsson et al., 2016)).

1.4 Determining ice sheet elevation change

Satellite radar altimeter data acquired over land ice are primarily used to study ice sheet elevation change. The kilometre scale spatial and approximately monthly temporal sampling of such data make them key to many estimates of ice sheet mass balance and sea level contribution (e.g. (McMillan et al., 2016, 2014; Schröder et al., 2019; Shepherd et al., 2019, 2012; The IMBIE Team, 2018)). Historically, ice sheet elevation change has been most commonly determined using the crossover (e.g.(Davis et al., 2005; Khvorostovsky, 2012; Wingham et al., 1998; Zwally et al., 2005)) and repeat-track/plane-fit (e.g. (Flament and Rémy, 2012; McMillan et al., 2016, 2014; Sandberg Sørensen et al., 2018; Schröder et al., 2019; Simonsen and Sørensen, 2017)) techniques.

1.4.1 Measuring ice sheet elevation change using crossover analysis

Early estimates of ice sheet elevation change derived from satellite radar altimeters analysed elevation differences at crossing points between ascending and descending ground tracks from successive orbits (Figure 1.10). Satellite altimeters acquire measurements every few hundred metres along the ground track — as a result crossover point elevations are determined by linearly interpolating adjacent elevation measurements to the exact crossover location. Elevation differences at a given crossover location can be computed as either ascending minus descending or descending minus ascending: elevation differences from successive cycles are taken as the average of the two crossover differences (e.g. (Wingham et al., 1998, 2006b)). Time series of height change are generated by differencing successive orbit cycles from a reference cycle at a particular crossover location. Elevation differences from satellite crossovers within a defined region are then averaged to reduce uncorrelated noise. Changes in backscatter result in

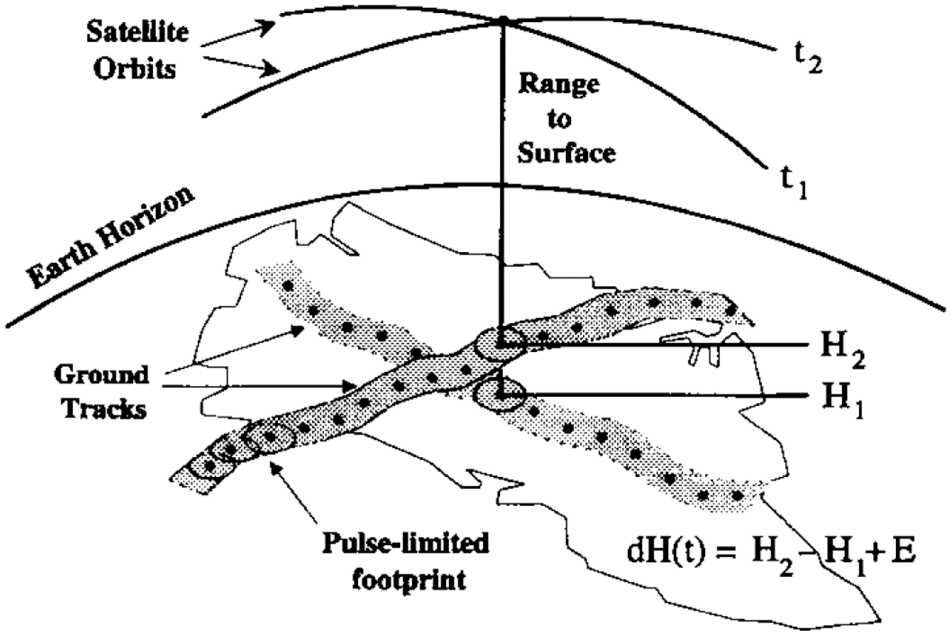

Figure 1.10: Illustration of crossover technique: successive altimeter orbits at times t_1 and t_2 are used to measure the change in elevation $dH(t) = H_2 - H_1 + E$ where H_1 and H_2 correspond to the measured height at times t_1 and t_2, respectively, and E is the random measurement error, which includes satellite orbit, altimeter range measurement and retracking errors. Extracted from (Davis, 1995)

spurious changes in elevation (Arthern et al., 2001), so it is common to apply an empirical backscatter correction which accounts for correlated fluctuations in backscattered power and elevation (e.g. (Davis and Ferguson, 2004; Wingham et al., 1998)). Elevation trends are then retrieved by fitting a model to the elevation time series, which typically takes the form of a linear plus sinusoidal function to account for seasonal cycles in elevation (e.g. (Shepherd et al., 2012; Wingham et al., 1998, 2006b)).

Because crossover elevation differences are determined at the intersection of ground tracks, direct slope-induced errors are reduced. The spatial resolution of crossover solutions is dependent on the orbital pattern and crossover density varies as a function of latitude (i.e. decreasing towards the equator). As a result, estimates of elevation change

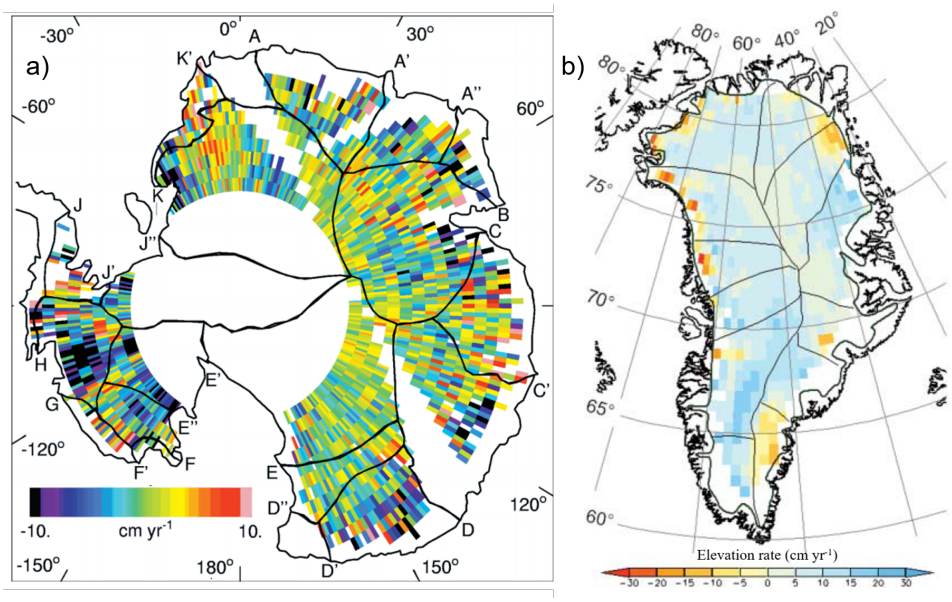

Figure 1.11: Rate of elevation change of the (a) Antarctic and (b) Greenland ice sheets between 1992 and 2003, determined from crossover analysis of ERS-1 and ERS-2 satellite altimeter data. Extracted from (a) (Wingham et al., 1998) and (b) (Johannessen et al., 2005).

derived from crossover analysis (e.g. Figure 1.11) do not provide complete coverage of the ice sheets, particularly where ground tracks are sparse, and require interpolation to avoid introducing bias into spatially-integrated trends.

1.4.2 Measuring ice sheet elevation change using repeat-track/plane-fit method

Unlike crossover analysis, the repeat-track method utilises all elevation data along the satellite track. Satellite tracks are split into kilometre-scale segments (e.g. (Flament and Rémy, 2012)), within which all elevation measurements acquired over successive cycles are grouped. Available measurements within a $\sim$ 500 m radius of the mean ground track are processed together to allow for across-track scatter due to satellite drift. The distribution of data can then be used to separate the spatial (i.e. topography) and temporal contributions to the measured elevation fluctuations within each defined region. This is achieved by fitting a model which typically describes the topography as a

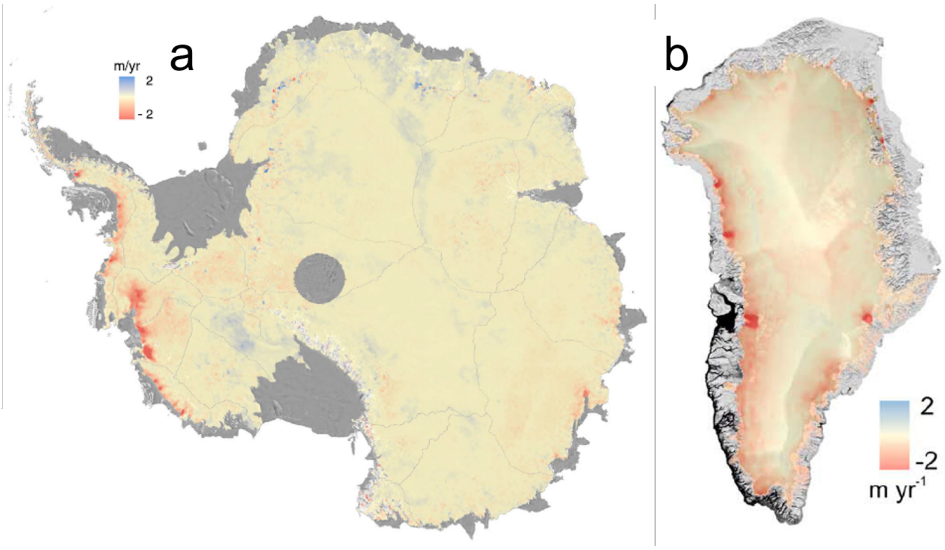

Figure 1.12: Rate of elevation change of the (a) Antarctic Ice Sheet between 2010 and 2013 and (b) Greenland Ice Sheet between 2011 and 2014 derived from the application of the plane-fit approach to CryoSat-2 satellite altimeter data. Extracted from (a) (McMillan et al., 2014) and (b) (McMillan et al., 2016).

second order polynomial and temporal change as a linear function of time (e.g. (Flament and Rémy, 2012; McMillan et al., 2014; Nilsson et al., 2016; Sandberg Sørensen et al., 2015)). Additional parameters may be introduced (e.g. (McMillan et al., 2014)) to account for additional factors which influence elevation, such as anisotropy in the retrieved elevation dependent on the satellite direction (Armitage et al., 2014). Like with crossover analysis it is necessary to account for spurious elevation changes introduced by fluctuations in backscattered power, either through an empirical backscatter correction (e.g. (McMillan et al., 2014; Sandberg Sørensen et al., 2018)) or through including waveform parameters such as the leading edge in the model fit (e.g. (Flament and Rémy, 2012; Sandberg Sørensen et al., 2018; Simonsen and Sørensen, 2017)).

By using all elevation data acquired along the ground track, the repeat-track method provides increased data volume and spatial coverage. This is of particular importance over the ice sheet margins where the dynamic signal is strong and where spatial coverage from crossover analysis is poorer due to only considering track intersections rather

than the full tracks themselves, and altimeters losing lock over tracks which pass from ocean to coast (Flament and Rémy, 2012). Recent modifications to the repeat-track approach do not distinguish between satellite tracks, but group data based on their spatial proximity before fitting to a model. This 'plane-fit' method (e.g. (McMillan et al., 2016, 2014; Sandberg Sørensen et al., 2018; Shepherd et al., 2019)) is particularly suited to the drifting orbit of CryoSat-2, which samples along a dense network of ground tracks with few coincident repeats (e.g. Figure 1.12).

1.5 Principal challenges for land ice altimetry

The principal challenges for observing land ice with satellite radar altimeters are primarily associated with the heterogeneous topography illuminated within the ground footprint, and the complex interaction between the radar pulse and spatially and temporally variable snowpack scattering characteristics. Rugged terrain can distort the waveform shape (Section 1.2.5), affecting the retracked height, and slope-induced errors (Section 1.2.6) must be accounted for (Brenner et al., 1983) (Figure 1.7). In regions of highly complex terrain (e.g. the ice sheet margins) the on-board tracker can fail, resulting in the loss of data; such regions tend to be where the most pronounced changes occur (e.g. narrow outlet glaciers). These issues are exacerbated for pulse-limited altimeters which have a larger footprint; delay-Doppler processing in SAR altimeters (e.g. (McMillan et al., 2019)) improves coverage in rugged terrain, and is even better in SARIn mode (Wingham et al., 2006a) which can precisely locate the echoes.

The depth to which the Ku band frequency, primarily used by altimeters, penetrates beyond the ice sheet surface is influenced by the physical properties of the snowpack: temperature, snow grain size, liquid water content (Matzler, 1996), and the subsurface stratigraphy between interannual accumulation layers (e.g. (Hawley et al., 2006)). Theoretically, Ku band radar can travel to a depth of approximately 10 m in a dry snowpack (Arthern et al., 2001). The interaction between radar pulse is also dependent on the orientation of the satellite antenna; radar scattering is influenced by the interaction between the linearly polarised radar wave and wind-induced features of the firn (Armitage et al., 2014; Arthern et al., 2001). In the interior of the Greenland Ice Sheet, meteorological events have induced changes in snowpack scattering properties:

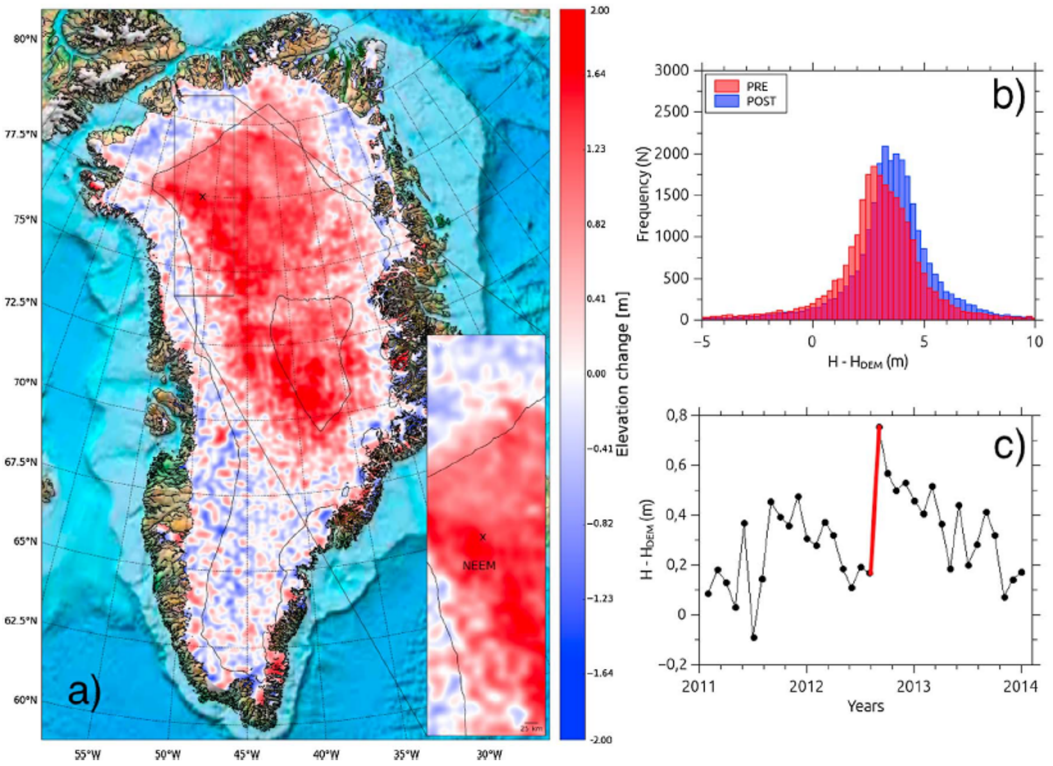

Figure 1.13: (a) Surface elevation differences between May - June and August - September 2012 from CryoSat-2 L2i data acquired either side of a melt event in 2012 which abruptly changed the scattering properties in the interior of the ice sheet from a regime dominated by volume scattering to one dominated by surface scattering. Black lines indicate 2000 and 3000 m elevation contours. (b) Histograms and (c) time series of changes in surface elevation around the North Greenland Eemian Ice Drilling Project site (black box) from CryoSat-2 L1b data. Extracted from (Nilsson et al., 2015).

an episode of widespread surface melting during the anomalously warm summer of 2012 formed ice lenses near to the surface which reset the radar scattering horizon and manifested in spurious elevation increases retrieved from radar altimetry (McMillan et al., 2016; Nilsson et al., 2015). Studies of ice sheet elevation change from satellite altimetry have attempted to mitigate the effects of variable radar backscatter through a combination of (1) applying an empirical correction which accounts for correlated fluctuations in backscattered power and elevation (e.g. (Davis and Ferguson, 2004; McMillan et al., 2016, 2014; Shepherd et al., 2019)), (2) accounting for changes in waveform parameters induced by changes in penetration depth (e.g. (Sandberg Sørensen et al., 2018; Simonsen and Sørensen, 2017)) and (3) the use of threshold retrackers which are less sensitive to variations in volume scattering (e.g. (Helm et al., 2014; Nilsson et al., 2016)).

In future, appealing to altimeters operating at different frequencies may afford insight into the nature of radar scattering within the snowpack. For example, the AltiKa mission (Table 1.3) is equipped with a Ka band (36 GHz) radar altimeter which will return from near to the surface: Ka band frequencies penetrate to depths of less than 1 m in the snowpack and volume scattering is mostly dependent on ice grain size alone (Verron et al., 2015). A study of Ku and Ka band measurements is an opportunity to compare their respective penetration depths and better characterise the uncertainties in the Ku band altimeter record.

1.6 Thesis aim

This thesis aims to develop novel methods and datasets, based upon the processing of CryoSat-2 satellite radar altimetry data, to improve the understanding of retrieving elevation and elevation change over Earth's polar ice sheets.

1.7 Thesis objectives

The following list of objectives have been defined in order to address the aim of this thesis:

1. Develop a new Digital Elevation Model (DEM) of the Antarctic Ice Sheet using the extensive CryoSat-2 data record to increase the accuracy and data coverage

when compared to previous DEMs derived from satellite altimeters

2. Develop a technique to retrieve estimates of the depth distribution of radar backscatter from CryoSat-2 altimeter waveforms using a backscatter model.

3. Apply this technique to characterise the spatial and temporal changes in radar backscatter across the Greenland Ice Sheet.

4. Evaluate how variability in radar backscatter affects elevation change estimates obtained from satellite radar altimetry using different retracking techniques.

5. Utilise the high spatial coverage and accuracy of CryoSat-2 in areas of complex terrain to quantify seasonal elevation changes in the ablation zone of the Greenland Ice Sheet.

1.8 Thesis structure

The remainder of this thesis can be summarised as follows: in Chapter 2, I present a new Digital Elevation Model of Antarctica, derived from 6 years of CryoSat-2 observations. In Chapter 3, I characterise spatial and temporal variations in radar backscatter, and estimate changes in the effective penetration depth, of CryoSat-2 Ku band altimetry over the Greenland Ice Sheet between 2011 and 2017. Using this information I then examine the effects of this variability on CryoSat-2 elevation trends derived over the same period, and develop a technique to effectively compensate for changes in radar penetration depth. In Chapter 4, I develop time series of elevation change for the ablation zone of the Greenland Ice Sheet from CryoSat-2 satellite radar altimetry, and in combination with results from a regional climate model, investigate seasonal rates of elevation change driven by melting and snowfall accumulation. In Chapter 5, I synthesise the thesis findings, place these results within a wider context and discuss potential avenues for future research.

References

A, G., Wahr, J., and Zhong, S. (2012). Computations of the viscoelastic response of a 3-D compressible Earth to surface loading: an application to Glacial Isostatic Adjustment in Antarctica and Canada. *Geophysical Journal International*, 192(2):557–572. 9

Ahlstrøm, A. P., Petersen, D., Langen, P. L., Citterio, M., and Box, J. E. (2017). Abrupt shift in the observed runoff from the southwestern Greenland ice sheet. *Science Advances*, 3(12):e1701169. 7

Armitage, T. W. K., Wingham, D. J., and Ridout, A. L. (2014). Meteorological origin of the static crossover pattern present in low-resolution-mode CryoSat-2 data over central Antarctica. *IEEE Geoscience and Remote Sensing Letters*, 11(7):1295–1299. 23, 24

Arthern, R. J., Wingham, D. J., and Ridout, A. L. (2001). Controls on ERS altimeter measurements over ice sheets: Footprint-scale topography, backscatter fluctuations, and the dependence of microwave penetration depth on satellite orientation. *Journal of Geophysical Research: Atmospheres*, 106(D24):33471–33484. 21, 24

Bamber, J. L. (2004). Ice sheet altimeter processing scheme. *International Journal of Remote Sensing*, 15(4):925–938. xi, 16, 17

Bamber, J. L., Ekholm, S., and Krabill, W. (1998). The accuracy of satellite radar altimeter data over the Greenland Ice Sheet determined from airborne laser data. *Geophysical Research Letters*, 25(16):3177–3180. 16

Barletta, V. R., Bevis, M., Smith, B. E., Wilson, T., Brown, A., Bordoni, A., Willis, M., Khan, S. A., Rovira-Navarro, M., Dalziel, I., Smalley, R., Kendrick, E., Konfal, S.,

Caccamise, D. J., Aster, R. C., Nyblade, A., and Wiens, D. A. (2018). Observed rapid bedrock uplift in Amundsen Sea Embayment promotes ice-sheet stability. *Science*, 360(6395):1335. 3, 9

Bell, R. E., Studinger, M., Shuman, C. A., Fahnestock, M. A., and Joughin, I. (2007). Large subglacial lakes in East Antarctica at the onset of fast-flowing ice streams. *Nature*, 445:904. 7

Bevis, M., Harig, C., Khan, S. A., Brown, A., Simons, F. J., Willis, M., Fettweis, X., van den Broeke, M. R., Madsen, F. B., Kendrick, E., Caccamise, D. J., van Dam, T., Knudsen, P., and Nylen, T. (2019). Accelerating changes in ice mass within Greenland, and the ice sheet's sensitivity to atmospheric forcing. *Proceedings of the National Academy of Sciences*, page 201806562. 7

Boening, C., Lebsock, M., Landerer, F., and Stephens, G. (2012). Snowfall-driven mass change on the East Antarctic Ice Sheet. *Geophysical Research Letters*, 39(21). 6

Bondzio, J. H., Morlighem, M., Seroussi, H., Kleiner, T., Rückamp, M., Mouginot, J., Moon, T., Larour, E. Y., and Humbert, A. (2017). The mechanisms behind Jakobshavn Isbræ's acceleration and mass loss: A 3-D thermomechanical model study. *Geophysical Research Letters*, 44(12):6252–6260. 5

Brenner, A. C., Blndschadler, R. A., Thomas, R. H., and Zwally, H. J. (1983). Slope-induced errors in radar altimetry over continental ice sheets. *Journal of Geophysical Research*, 88(C3):1617. 15, 16, 24

Brown, G. (1977). The average impulse response of a rough surface and its applications. *IEEE Transactions on Antennas and Propagation*, 25(1):67–74. 14, 15

Church, J., Clark, P., Cazenave, A., Gregory, J., Jevrejeva, S., Levermann, A., Merrifield, M., Milne, G., Nerem, R., Nunn, P., Payne, A., Pfeffer, W., Stammer, D., and Unnikrishnan, A. (2013). *Sea Level Change*, book section 13, page 1137–1216. Cambridge University Press, Cambridge, United Kingdom and New York, NY, USA. 1

Cook, A. J. and Vaughan, D. G. (2010). Overview of areal changes of the ice shelves on the Antarctic Peninsula over the past 50 years. *The Cryosphere*, 4(1):77–98. 3

Davis, C. H. (1995). Growth of the Greenland Ice Sheet: a performance assessment of altimeter retracking algorithms. *IEEE Transactions on Geoscience and Remote Sensing*, 33(5):1108–1116. xi, 21

Davis, C. H. (1997). A robust threshold retracking algorithm for measuring ice-sheet surface elevation change from satellite radar altimeters. *IEEE Transactions on Geoscience and Remote Sensing*, 35(4):974–979. 14, 15

Davis, C. H. and Ferguson, A. C. (2004). Elevation change of the Antarctic ice sheet, 1995-2000, from ERS-2 satellite radar altimetry. *IEEE Transactions on Geoscience and Remote Sensing*, 42(11):2437–2445. 21, 26

Davis, C. H., Li, Y., McConnell, J. R., Frey, M. M., and Hanna, E. (2005). Snowfall-driven growth in East Antarctic Ice Sheet mitigates recent sea-level rise. *Science*, 308(5730):1898. 2, 20

De Angelis, H. and Skvarca, P. (2003). Glacier surge after ice shelf collapse. *Science*, 299(5612):1560–1562. 3

Enderlin, E. M., Howat, I. M., Jeong, S., Noh, M.-J., Angelen, J. H., and Broeke, M. R. (2014). An improved mass budget for the Greenland Ice Sheet. *Geophysical Research Letters*, 41(3):866–872. 2, 6

Fettweis, X., Hanna, E., Lang, C., Belleflamme, A., Erpicum, M., and Gallée, H. (2013). Brief communication: Important role of the mid-tropospheric atmospheric circulation in the recent surface melt increase over the Greenland ice sheet. *The Cryosphere*, 7(1):241–248. 7

Flament, T. and Rémy, F. (2012). Dynamic thinning of Antarctic glaciers from along-track repeat radar altimetry. *Journal of Glaciology*, 58(211):830–840. 2, 3, 20, 22, 23, 24

Forsberg, R., Sørensen, L., and Simonsen, S. (2017). Greenland and Antarctica Ice Sheet mass changes and effects on global sea level. *Surveys in Geophysics*, 38(1):89–104. 2

Fretwell, P., Pritchard, H. D., Vaughan, D. G., Bamber, J. L., Barrand, N. E., Bell, R., Bianchi, C., Bingham, R. G., Blankenship, D. D., Casassa, G., Catania, G., Callens, D., Conway, H., Cook, A. J., Corr, H. F. J., Damaske, D., Damm, V., Ferraccioli, F., Forsberg, R., Fujita, S., Gim, Y., Gogineni, P., Griggs, J. A., Hindmarsh, R. C. A., Holmlund, P., Holt, J. W., Jacobel, R. W., Jenkins, A., Jokat, W., Jordan, T., King, E. C., Kohler, J., Krabill, W., Riger-Kusk, M., Langley, K. A., Leitchenkov, G., Leuschen, C., Luyendyk, B. P., Matsuoka, K., Mouginot, J., Nitsche, F. O., Nogi, Y., Nost, O. A., Popov, S. V., Rignot, E., Rippin, D. M., Rivera, A., Roberts, J., Ross, N., Siegert, M. J., Smith, A. M., Steinhage, D., Studinger, M., Sun, B., Tinto, B. K., Welch, B. C., Wilson, D., Young, D. A., Xiangbin, C., and Zirizzotti, A. (2013). Bedmap2: improved ice bed, surface and thickness datasets for Antarctica. *The Cryosphere*, 7(1):375–393. 1

Fricker, H. A., Scambos, T., Bindschadler, R., and Padman, L. (2007). An active subglacial water system in West Antarctica mapped from space. *Science*, 315(5818):1544. 7

Fu, L. and Cazenave, A. (2001). *Satellite Altimetry and Earth Sciences*. Academic Press, San Diego, CA, USA. 11

Hanna, E., Mernild, S. H., Cappelen, J., and Steffen, K. (2012). Recent warming in Greenland in a long-term instrumental (1881–2012) climatic context: I. Evaluation of surface air temperature records. *Environmental Research Letters*, 7(4):045404. 5, 6

Hawley, R. L., Morris, E. M., Cullen, R., Nixdorf, U., Shepherd, A. P., and Wingham, D. J. (2006). ASIRAS airborne radar resolves internal annual layers in the dry-snow zone of Greenland. *Geophysical Research Letters*, 33(4). 24

Helm, V., Humbert, A., and Miller, H. (2014). Elevation and elevation change of Greenland and Antarctica derived from CryoSat-2. *The Cryosphere*, 8(4):1539–1559. 5, 14, 15, 20, 26

Hoffman, M. J., Catania, G. A., Neumann, T. A., Andrews, L. C., and Rumrill, J. A. (2011). Links between acceleration, melting, and supraglacial lake drainage

of the western Greenland Ice Sheet. *Journal of Geophysical Research: Earth Surface*, 116(F4). 5

Hogg, A. E., Shepherd, A., Cornford, S. L., Briggs, K. H., Gourmelen, N., Graham, J. A., Joughin, I., Mouginot, J., Nagler, T., Payne, A. J., Rignot, E., and Wuite, J. (2017). Increased ice flow in Western Palmer Land linked to ocean melting. *Geophysical Research Letters*, 44(9):4159–4167. 3

Holland, D. M., Thomas, R. H., de Young, B., Ribergaard, M. H., and Lyberth, B. (2008). Acceleration of Jakobshavn Isbræ triggered by warm subsurface ocean waters. *Nature Geoscience*, 1:659. 5

Howat, I. M., Porter, C., Noh, M. J., Smith, B. E., and Jeong, S. (2015). Brief communication: sudden drainage of a subglacial lake beneath the Greenland Ice Sheet. *The Cryosphere*, 9(1):103–108. 7

Hurkmans, R. T. W. L., Bamber, J. L., and Griggs, J. A. (2012). Brief communication: importance of slope-induced error correction in volume change estimates from radar altimetry. *The Cryosphere*, 6(2):447–451. 16

Jacobs, S. S., Jenkins, A., Giulivi, C. F., and Dutrieux, P. (2011). Stronger ocean circulation and increased melting under Pine Island Glacier ice shelf. *Nature Geoscience*, 4:519. 3

Jensen, J. R. (1999). Angle measurement with a phase monopulse radar altimeter. *IEEE Transactions on Antennas and Propagation*, 47(4):715–724. 19

Johannessen, O. M., Khvorostovsky, K., Miles, M. W., and Bobylev, L. P. (2005). Recent ice-sheet growth in the interior of Greenland. *Science*, 310(5750):1013–1016. xii, 22

Joughin, I., Alley, R. B., and Holland, D. M. (2012). Ice-sheet response to oceanic forcing. *Science*, 338(6111):1172. x, 5

Joughin, I., Rignot, E., Rosanova, C. E., Lucchitta, B. K., and Bohlander, J. (2003). Timing of recent accelerations o Pine Island Glacier, Antarctica. *Geophysical Research Letters*, 30(13). 3

Joughin, I., Smith, B. E., Howat, I. M., Scambos, T., and Moon, T. (2010). Greenland flow variability from ice-sheet-wide velocity mapping. *Journal of Glaciology*, 56(197):415–430. 2

Joughin, I., Smith, B. E., Shean, D. E., and Floricioiu, D. (2014). Brief communication: Further summer speedup of Jakobshavn Isbræ. *The Cryosphere*, 8(1):209–214. 3

Khazendar, A., Fenty, I. G., Carroll, D., Gardner, A., Lee, C. M., Fukumori, I., Wang, O., Zhang, H., Seroussi, H., Moller, D., Noël, B. P. Y., van den Broeke, M. R., Dinardo, S., and Willis, J. (2019). Interruption of two decades of Jakobshavn Isbræ acceleration and thinning as regional ocean cools. *Nature Geoscience*, 12(4):277–283. 5

Khvorostovsky, K. S. (2012). Merging and analysis of elevation time series over Greenland ice sheet from satellite radar altimetry. *IEEE Transactions on Geoscience and Remote Sensing*, 50(1):23–36. 20

King, M. D., Howat, I. M., Jeong, S., Noh, M. J., Wouters, B., Noël, B., and van den Broeke, M. R. (2018). Seasonal to decadal variability in ice discharge from the Greenland Ice Sheet. *The Cryosphere*, 12(12):3813–3825. 5

Konrad, H., Gilbert, L., Cornford, S. L., Payne, A., Hogg, A., Muir, A., and Shepherd, A. (2017). Uneven onset and pace of ice-dynamical imbalance in the Amundsen Sea Embayment, West Antarctica. *Geophysical Research Letters*, 44(2):910–918. 2, 3

Konrad, H., Sasgen, I., Pollard, D., and Klemann, V. (2015). Potential of the solid-Earth response for limiting long-term West Antarctic Ice Sheet retreat in a warming climate. *Earth and Planetary Science Letters*, 432:254–264. 9

Konrad, H., Shepherd, A., Gilbert, L., Hogg, A. E., McMillan, M., Muir, A., and Slater, T. (2018). Net retreat of Antarctic glacier grounding lines. *Nature Geoscience*, 11(4):258–262. 3

Laxon, S. W., Giles, K. A., Ridout, A. L., Wingham, D. J., Willatt, R., Cullen, R., Kwok, R., Schweiger, A., Zhang, J., Haas, C., Hendricks, S., Krishfield, R., Kurtz, N., Farrell, S., and Davidson, M. (2013). CryoSat-2 estimates of Arctic sea ice thickness and volume. *Geophysical Research Letters*, 40(4):732–737. 20

Legrésy, B., Papa, F., Rémy, F., Vinay, G., van den Bosch, M., and Zanife, O.-Z. (2005). ENVISAT radar altimeter measurements over continental surfaces and ice caps using the ICE-2 retracking algorithm. *Remote Sensing of Environment*, 95(2):150–163. 14

Legrésy, B. and Rémy, F. (1997). Altimetric observations of surface characteristics of the Antarctic Ice Sheet. *Journal of Glaciology*, 43(144):265–275. 14

Lemos, A., Shepherd, A., McMillan, M., Hogg, A. E., Hatton, E., and Joughin, I. (2018). Ice velocity of Jakobshavn Isbræ, Petermann Glacier, Nioghalvfjerdsfjorden, and Zachariæ isstrøm, 2015–2017, from Sentinel 1-a/b SAR imagery. *The Cryosphere*, 12(6):2087–2097. 5

Lenaerts, J. T. M., van den Broeke, M. R., van de Berg, W. J., van Meijgaard, E., and Kuipers Munneke, P. (2012). A new, high-resolution surface mass balance map of Antarctica (1979-2010) based on regional atmospheric climate modeling. *Geophysical Research Letters*, 39(4). 6

Lenaerts, J. T. M., van Meijgaard, E., van den Broeke, M. R., Ligtenberg, S. R. M., Horwath, M., and Isaksson, E. (2013). Recent snowfall anomalies in Dronning Maud Land, East Antarctica, in a historical and future climate perspective. *Geophysical Research Letters*, 40(11):2684–2688. 6

Martin, T. V., Zwally, H. J., Brenner, A. C., and Bindschadler, R. A. (1983). Analysis and retracking of continental ice sheet radar altimeter waveforms. *Journal of Geophysical Research: Oceans*, 88(C3):1608–1616. 14

Matzler, C. (1996). Microwave permittivity of dry snow. *IEEE Transactions on Geoscience and Remote Sensing*, 34(2):573–581. 14, 24

McMillan, M., Corr, H., Shepherd, A., Ridout, A., Laxon, S., and Cullen, R. (2013). Three-dimensional mapping by CryoSat-2 of subglacial lake volume changes. *Geophysical Research Letters*, 40(16):4321–4327. 3, 7

McMillan, M., Leeson, A., Shepherd, A., Briggs, K., Armitage, T. W. K., Hogg, A., Kuipers Munneke, P., van den Broeke, M., Noël, B., van de Berg, W. J., Ligtenberg, S., Horwath, M., Groh, A., Muir, A., and Gilbert, L. (2016). A high-resolution record of Greenland mass balance. *Geophysical Research Letters*, 43(13):7002–7010. xii, 2, 5, 7, 20, 23, 24, 26

McMillan, M., Muir, A., Shepherd, A., Escolà, R., Roca, M., Aublanc, J., Thibaut, P., Restano, M., Ambrozio, A., and Benveniste, J. (2019). Sentinel-3 delay-doppler altimetry over Antarctica. *The Cryosphere*, 13(2):709–722. 24

McMillan, M., Shepherd, A., Sundal, A., Briggs, K., Muir, A., Ridout, A., Hogg, A., and Wingham, D. (2014). Increased ice losses from Antarctica detected by CryoSat-2. *Geophysical Research Letters*, 41(11):3899–3905. xii, 2, 3, 20, 23, 24, 26

Medley, B., McConnell, J. R., Neumann, T. A., Reijmer, C. H., Chellman, N., Sigl, M., and Kipfstuhl, S. (2018). Temperature and snowfall in Western Queen Maud Land increasing faster than climate model projections. *Geophysical Research Letters*, 45(3):1472–1480. 6

Medley, B. and Thomas, E. R. (2019). Increased snowfall over the Antarctic Ice Sheet mitigated twentieth-century sea-level rise. *Nature Climate Change*, 9(1):34–39. 2

Milne, G. A., Latychev, K., Schaeffer, A., Crowley, J. W., Lecavalier, B. S., and Audette, A. (2018). The influence of lateral Earth structure on glacial isostatic adjustment in Greenland. *Geophysical Journal International*, 214(2):1252–1266. 9

Morlighem, M., Williams, C. N., Rignot, E., An, L., Arndt, J. E., Bamber, J. L., Catania, G., Chauché, N., Dowdeswell, J. A., Dorschel, B., Fenty, I., Hogan, K., Howat, I., Hubbard, A., Jakobsson, M., Jordan, T. M., Kjeldsen, K. K., Millan, R., Mayer, L., Mouginot, J., Noël, B. P. Y., O'Cofaigh, C., Palmer, S., Rysgaard, S., Seroussi, H., Siegert, M. J., Slabon, P., Straneo, F., van den Broeke, M. R., Weinrebe, W., Wood, M., and Zinglersen, K. B. (2017). BedMachine v3: Complete bed topography and ocean bathymetry mapping of Greenland from multibeam echo sounding combined with mass conservation. *Geophysical Research Letters*, 44(21):11,051–11,061. 1

Mouginot, J., Rignot, E., Bjørk, A. A., van den Broeke, M., Millan, R., Morlighem, M., Noël, B., Scheuchl, B., and Wood, M. (2019). Forty-six years of Greenland Ice Sheet mass balance from 1972 to 2018. *Proceedings of the National Academy of Sciences*, page 201904242. 2

Mouginot, J., Rignot, E., and Scheuchl, B. (2014). Sustained increase in ice discharge from the Amundsen Sea Embayment, West Antarctica, from 1973 to 2013. *Geophysical Research Letters*, 41(5):1576–1584. 2

Nghiem, S. V., Hall, D. K., Mote, T. L., Tedesco, M., Albert, M. R., Keegan, K., Shuman, C. A., DiGirolamo, N. E., and Neumann, G. (2012). The extreme melt across the Greenland ice sheet in 2012. *Geophysical Research Letters*, 39(20). 6

Nilsson, J., Gardner, A., Sandberg Sørensen, L., and Forsberg, R. (2016). Improved retrieval of land ice topography from CryoSat-2 data and its impact for volume-change estimation of the Greenland ice sheet. *The Cryosphere*, 10(6):2953–2969. 5, 14, 15, 20, 23, 26

Nilsson, J., Vallelonga, P., Simonsen, S. B., Sørensen, L. S., Forsberg, R., Dahl-Jensen, D., Hirabayashi, M., Goto-Azuma, K., Hvidberg, C. S., Kjaer, H. A., and Satow, K. (2015). Greenland 2012 melt event effects on CryoSat-2 radar altimetry. *Geophysical Research Letters*, 42(10):3919–3926. xii, 25, 26

Palmer, S. J., Dowdeswell, J. A., Christoffersen, P., Young, D. A., Blankenship, D. D., Greenbaum, J. S., Benham, T., Bamber, J., and Siegert, M. J. (2013). Greenland subglacial lakes detected by radar. *Geophysical Research Letters*, 40(23):6154–6159. 7

Palmer, S. J., McMillan, M., and Morlighem, M. (2015). Subglacial lake drainage detected beneath the Greenland Ice Sheet. *Nature Communications*, 6:8408. 7

Paolo, F. S., Fricker, H. A., and Padman, L. (2015). Volume loss from Antarctic ice shelves is accelerating. *Science*, 348(6232):327. 3

Park, J. W., Gourmelen, N., Shepherd, A., Kim, S. W., Vaughan, D. G., and Wingham, D. J. (2013). Sustained retreat of the Pine Island Glacier. *Geophysical Research Letters*, 40(10):2137–2142. 3

Pattyn, F. (2010). Antarctic subglacial conditions inferred from a hybrid ice sheet/ice stream model. *Earth and Planetary Science Letters*, 295(3):451–461. 7

Peltier, W. R. (1974). The impulse response of a Maxwell Earth. *Reviews of Geophysics*, 12(4):649–669. 9

Pritchard, H. D., Ligtenberg, S. R., Fricker, H. A., Vaughan, D. G., van den Broeke, M. R., and Padman, L. (2012). Antarctic ice-sheet loss driven by basal melting of ice shelves. *Nature*, 484(7395):502–5. 3

Raney, R. K. (1998). The delay/doppler radar altimeter. *IEEE Transactions on Geoscience and Remote Sensing*, 36(5):1578–1588. xi, 16, 18

Rèmy, F., Mazzega, P., Houry, S., Brossier, C., and Minster, J. F. (1989). Mapping of the topography of continental ice by inversion of satellite-altimeter data. *Journal of Glaciology*, 35(119):98–107. 16

Ricker, R., Hendricks, S., Perovich, D. K., Helm, V., and Gerdes, R. (2015). Impact of snow accumulation on CryoSat-2 range retrievals over Arctic sea ice: An observational approach with buoy data. *Geophysical Research Letters*, 42(11):4447–4455. 20

Ridley, J. K. and Partington, K. C. (1988). A model of satellite radar altimeter return from ice sheets. *International Journal of Remote Sensing*, 9(4):601–624. 14, 15

Rignot, E. (2001). Evidence for rapid retreat and mass loss of Thwaites Glacier, West Antarctica. *Journal of Glaciology*, 47(157):213–222. 3

Rignot, E., Casassa, G., Gogineni, P., Krabill, W., Rivera, A., and Thomas, R. (2004). Accelerated ice discharge from the Antarctic Peninsula following the collapse of Larsen B ice shelf. *Geophysical Research Letters*, 31(18). 3

Rignot, E. and Kanagaratnam, P. (2006). Changes in the velocity structure of the Greenland Ice Sheet. *Science*, 311(5763):986. 3

Rignot, E., Mouginot, J., Scheuchl, B., van den Broeke, M., van Wessem, M. J., and Morlighem, M. (2019). Four decades of Antarctic Ice Sheet mass balance from 1979–2017. *Proceedings of the National Academy of Sciences*, page 201812883. 2

Rignot, E., Velicogna, I., van den Broeke, M. R., Monaghan, A., and Lenaerts, J. T. M. (2011). Acceleration of the contribution of the Greenland and Antarctic ice sheets to sea level rise. *Geophysical Research Letters*, 38(5). 2

Riva, R. E. M., Gunter, B. C., Urban, T. J., Vermeersen, B. L. A., Lindenbergh, R. C., Helsen, M. M., Bamber, J. L., van de Wal, R. S. W., van den Broeke, M. R., and Schutz, B. E. (2009). Glacial Isostatic Adjustment over Antarctica from combined ICESat and GRACE satellite data. *Earth and Planetary Science Letters*, 288(3):516–523. 3, 9

Roemer, S., Legrésy, B., Horwath, M., and Dietrich, R. (2007). Refined analysis of radar altimetry data applied to the region of the subglacial Lake Vostok/Antarctica. *Remote Sensing of Environment*, 106(3):269–284. 16

Sandberg Sørensen, L., Simonsen, S. B., Forsberg, R., Khvorostovsky, K., Meister, R., and Engdahl, M. E. (2018). 25 years of elevation changes of the Greenland ice sheet from ERS, Envisat, and CryoSat-2 radar altimetry. *Earth and Planetary Science Letters*, 495:234–241. x, 5, 6, 7, 20, 23, 24, 26

Sandberg Sørensen, L., Simonsen, S. B., Meister, R., Forsberg, R., Levinsen, J. F., and Flament, T. (2015). Envisat-derived elevation changes of the Greenland Ice Sheet, and a comparison with ICESat results in the accumulation area. *Remote Sensing of Environment*, 160:56 – 62. 23

Scambos, T., Hulbe, C., and Fahnstock, M. (2013). *Climate-Induced Ice Shelf Disintegration in the Antarctic Peninsula*. 3

Schröder, L., Horwath, M., Dietrich, R., Helm, V., van den Broeke, M. R., and Ligtenberg, S. R. M. (2019). Four decades of Antarctic surface elevation changes from multi-mission satellite altimetry. *The Cryosphere*, 13(2):427–449. 2, 3, 20

Seale, A., Christoffersen, P., Mugford, R. I., and O'Leary, M. (2011). Ocean forcing of the Greenland Ice Sheet: Calving fronts and patterns of retreat identified by automatic satellite monitoring of eastern outlet glaciers. *Journal of Geophysical Research: Earth Surface*, 116(F3). 5

Shepherd, A., Fricker, H. A., and Farrell, S. F. (2018). Trends and connections across the Antarctic cryosphere. *Nature*, 558(7709):223–232. x, 2, 4

Shepherd, A., Gilbert, L., Muir, A. S., Konrad, H., McMillan, M., Slater, T., Briggs, K. H., Sundal, A. V., Hogg, A. E., and Engdahl, M. (2019). Trends in Antarctic Ice Sheet elevation and mass. *Geophysical Research Letters*. 2, 3, 20, 24, 26

Shepherd, A., Ivins, E. R., A, G., Barletta, V. R., Bentley, M. J., Bettadpur, S., Briggs, K. H., Bromwich, D. H., Forsberg, R., Galin, N., Horwath, M., Jacobs, S., Joughin, I., King, M. A., Lenaerts, J. T. M., Li, J., Ligtenberg, S. R. M., Luckman, A., Luthcke, S. B., McMillan, M., Meister, R., Milne, G., Mouginot, J., Muir, A.,

Nicolas, J. P., Paden, J., Payne, A. J., Pritchard, H., Rignot, E., Rott, H., Sørensen, L. S., Scambos, T. A., Scheuchl, B., Schrama, E. J. O., Smith, B., Sundal, A. V., van Angelen, J. H., van de Berg, W. J., van den Broeke, M. R., Vaughan, D. G., Velicogna, I., Wahr, J., Whitehouse, P. L., Wingham, D. J., Yi, D., Young, D., and Zwally, H. J. (2012). A reconciled estimate of ice-sheet mass balance. *Science*, 338(6111):1183. 1, 2, 6, 9, 20, 21

Shepherd, A. and Nowicki, S. (2017). Improvements in ice-sheet sea-level projections. *Nature Climate Change*, 7(10):672–674. 2

Shepherd, A., Wingham, D., Payne, T., and Skvarca, P. (2003). Larsen Ice Shelf has progressively thinned. *Science*, 302(5646):856. 3

Shepherd, A., Wingham, D., and Rignot, E. (2004). Warm ocean is eroding West Antarctic Ice Sheet. *Geophysical Research Letters*, 31(23). 3

Shepherd, A., Wingham, D. J., and Mansley, J. A. D. (2002). Inland thinning of the Amundsen Sea sector, West Antarctica. *Geophysical Research Letters*, 29(10):2–1–2–4. 2, 3

Shepherd, A., Wingham, D. J., Mansley, J. A. D., and Corr, H. F. J. (2001). Inland thinning of Pine Island Glacier, West Antarctica. *Science*, 291(5505):862–864. 3

Siegert, M. J., Le Brocq, A. M., and Payne, A. J. (2007). *Hydrological Connections between Antarctic Subglacial Lakes, the Flow of Water beneath the East Antarctic Ice Sheet and Implications for Sedimentary Processes*, pages 3–10. 7

Siegfried, M. R. and Fricker, H. A. (2018). Thirteen years of subglacial lake activity in Antarctica from multi-mission satellite altimetry. *Annals of Glaciology*, 59(76pt1):42–55. xi, 3, 7, 8

Simonsen, S. B. and Sørensen, L. S. (2017). Implications of changing scattering properties on Greenland ice sheet volume change from CryoSat-2 altimetry. *Remote Sensing of Environment*, 190:207–216. 7, 20, 23, 26

Slater, T. and Shepherd, A. (2018). Antarctic ice losses tracking high. *Nature Climate Change*. 2

Smith, B. E., Fricker, H. A., Joughin, I. R., and Tulaczyk, S. (2009). An inventory of active subglacial lakes in Antarctica detected by ICESat (2003–2008). *Journal of Glaciology*, 55(192):573–595. 7

Stearns, L. A., Smith, B. E., and Hamilton, G. S. (2008). Increased flow speed on a large East Antarctic outlet glacier caused by subglacial floods. *Nature Geoscience*, 1:827. 7

Sundal, A. V., Shepherd, A., Nienow, P., Hanna, E., Palmer, S., and Huybrechts, P. (2011). Melt-induced speed-up of Greenland Ice Sheet offset by efficient subglacial drainage. *Nature*, 469(7331):521–4. 6

Tedesco, M., Fettweis, X., Mote, T., Wahr, J., Alexander, P., Box, J. E., and Wouters, B. (2013). Evidence and analysis of 2012 Greenland records from spaceborne observations, a regional climate model and reanalysis data. *The Cryosphere*, 7(2):615–630. 7

Tedstone, A. J., Nienow, P. W., Gourmelen, N., Dehecq, A., Goldberg, D., and Hanna, E. (2015). Decadal slowdown of a land-terminating sector of the Greenland Ice Sheet despite warming. *Nature*, 526:692. 6

The IMBIE Team (2018). Mass balance of the Antarctic Ice Sheet from 1992 to 2017. *Nature*, 558(7709):219–222. 1, 2, 20

Tilling, R. L., Ridout, A., and Shepherd, A. (2016). Near-real-time Arctic sea ice thickness and volume from CryoSat-2. *The Cryosphere*, 10(5):2003–2012. 20

Tilling, R. L., Ridout, A., and Shepherd, A. (2018). Estimating Arctic sea ice thickness and volume using CryoSat-2 radar altimeter data. *Advances in Space Research*, 62(6):1203–1225. 18

Tilling, R. L., Ridout, A., Shepherd, A., and Wingham, D. J. (2015). Increased Arctic sea ice volume after anomalously low melting in 2013. *Nature Geoscience*, 8:643. 20

Trusel, L. D., Das, S. B., Osman, M. B., Evans, M. J., Smith, B. E., Fettweis, X., McConnell, J. R., Noël, B. P. Y., and van den Broeke, M. R. (2018). Nonlinear rise in Greenland runoff in response to post-industrial Arctic warming. *Nature*, 564(7734):104–108. 2

van Angelen, J. H., van den Broeke, M. R., Wouters, B., and Lenaerts, J. T. M. (2014). Contemporary (1960–2012) evolution of the climate and surface mass balance of the Greenland Ice Sheet. *Surveys in Geophysics*, 35(5):1155–1174. 6

van den Broeke, M. (2005). Strong surface melting preceded collapse of Antarctic Peninsula ice shelf. *Geophysical Research Letters*, 32(12). 3

van den Broeke, M., Bamber, J., Ettema, J., Rignot, E., Schrama, E., van de Berg, W. J., van Meijgaard, E., Velicogna, I., and Wouters, B. (2009). Partitioning recent Greenland mass loss. *Science*, 326(5955):984–6. 2

van den Broeke, M., Enderlin, E. M., Howat, I. M., Kuipers Munneke, P., Noël, B. P. Y., van de Berg, W. J., van Meijgaard, E., and Wouters, B. (2016). On the recent contribution of the Greenland Ice Sheet to sea level change. *The Cryosphere*, 10(5):1933–1946. 2, 6

Verron, J., Sengenes, P., Lambin, J., Noubel, J., Steunou, N., Guillot, A., Picot, N., Coutin-Faye, S., Sharma, R., Gairola, R. M., Murthy, D. V. A. R., Richman, J. G., Griffin, D., Pascual, A., Rémy, F., and Gupta, P. K. (2015). The SARAL/AltiKa altimetry satellite mission. *Marine Geodesy*, 38(sup1):2–21. 26

Wahr, J., Wingham, D., and Bentley, C. (2000). A method of combining ICESat and GRACE satellite data to constrain Antarctic mass balance. *Journal of Geophysical Research: Solid Earth*, 105(B7):16279–16294. 9

Whitehouse, P. L., Bentley, M. J., Milne, G. A., King, M. A., and Thomas, I. D. (2012). A new Glacial Isostatic Adjustment model for Antarctica: calibrated and tested using observations of relative sea-level change and present-day uplift rates. *Geophysical Journal International*, 190(3):1464–1482. 9

Wingham, D. J., Francis, C. R., Baker, S., Bouzinac, C., Brockley, D., Cullen, R., de Chateau-Thierry, P., Laxon, S. W., Mallow, U., Mavrocordatos, C., Phalippou, L., Ratier, G., Rey, L., Rostan, F., Viau, P., and Wallis, D. W. (2006a). CryoSat: A mission to determine the fluctuations in Earth's land and marine ice fields. *Advances in Space Research*, 37(4):841–871. xi, 16, 17, 18, 19, 24

Wingham, D. J., Rapley, C. G., and Griffiths, H. (1986). New techniques in satellite altimeter tracking systems. In *18th IGARSS Symposium*. 14, 15

Wingham, D. J., Ridout, A. J., Scharroo, R., Arthern, R. J., and Shum, C. K. (1998). Antarctic elevation change from 1992 to 1996. *Science*, 282(5388):456–458. xii, 20, 21, 22

Wingham, D. J., Shepherd, A., Muir, A., and Marshall, G. J. (2006b). Mass balance of the Antarctic Ice Sheet. *Philosophical Transactions of the Royal Society A: Mathematical, Physical and Engineering Sciences*, 364(1844):1627–1635. 20, 21

Wingham, D. J., Siegert, M. J., Shepherd, A., and Muir, A. S. (2006c). Rapid discharge connects Antarctic subglacial lakes. *Nature*, 440:1033. 7

Woodhouse, I. H. (2005). *Introduction to Microwave Remote Sensing*. CRC Press Taylor & Francis Group, Boca Raton, FL, USA. xi, 11, 12

Zwally, H. J., Abdalati, W., Herring, T., Larson, K., Saba, J., and Steffen, K. (2002). Surface melt-induced acceleration of Greenland Ice Sheet flow. *Science*, 297(5579):218–222. 5

Zwally, H. J., Giovinetto, M. B., Li, J., Cornejo, H. G., Beckley, M. A., Brenner, A. C., Saba, J. L., and Yi, D. (2005). Mass changes of the Greenland and Antarctic ice sheets and shelves and contributions to sea-level rise: 1992–2002. *Journal of Glaciology*, 51(175):509–527. 20

Chapter 2

A new Digital Elevation Model of Antarctica derived from CryoSat-2 altimetry

Authors: **Thomas Slater, Andrew Shepherd, Malcolm McMillan, Alan Muir, Lin Gilbert, Anna E. Hogg, Hannes Konrad, Tommaso Parrinello**

Abstract

We present a new Digital Elevation Model (DEM) of the Antarctic Ice Sheet and ice shelves based on 2.5 x 10^8 observations recorded by the CryoSat-2 satellite radar altimeter between July 2010 and July 2016. The DEM is formed from spatio-temporal fits to elevation measurements accumulated within 1, 2 and 5 km grid cells, and is posted at the modal resolution of 1 km. Altogether, 94 % of the grounded ice sheet and 98 % of the floating ice shelves are observed, and the remaining grid cells North of 88 ° S are interpolated using ordinary kriging. The median and root mean square difference between the DEM and 2.3 x 10^7 airborne laser altimeter measurements acquired during NASA Operation IceBridge campaigns are −0.30 m and 13.50 m, respectively. The DEM uncertainty rises in regions of high slope — especially where elevation measurements were acquired in Low Resolution Mode — and, taking this into account, we estimate the average accuracy to be 9.5 m — a value that is comparable to or better than that of other models derived from satellite radar and laser altimetry.

2.1 Introduction

Digital Elevation Models (DEMs) of Antarctica are important datasets required for the planning of fieldwork, numerical ice sheet modelling, and the tracking of ice motion. Measurements of ice sheet topography are needed as a boundary condition for numerical projections of ice dynamics and potential sea level contributions (Cornford et al., 2015; Ritz et al., 2015). Accurate knowledge of surface elevation can be used for both the delineation of drainage basins and estimation of grounding line ice thickness, necessary for estimates of Antarctic mass balance calculated via the mass budget method (Rignot et al., 2011b; Shepherd et al., 2012; Sutterley et al., 2014). Furthermore, detailed and up-to-date DEMs are required to distinguish between phase differences caused by topography and ice motion when estimating ice velocity using interferometric synthetic aperture radar (Mouginot et al., 2012; Rignot et al., 2011a).

Previously published DEMs of Antarctica have been derived from satellite radar altimetry (Fei et al., 2017; Helm et al., 2014), laser altimetry (DiMarzio et al., 2007), a combination of both radar and laser altimetry (Bamber et al., 2009; Griggs and Bamber, 2009), and through the integration of several sources of remote sensing and cartographic data (Fretwell et al., 2013; Liu et al., 2001). In addition, high resolution regional DEMs of the marginal areas of the ice sheet have been generated from stereoscopic (Korona et al., 2009) and radiometer surveys (Cook et al., 2012). Although these photogrammetric models perform well over regions of bare rock and steep slope found in the margins, their accuracy is considerably reduced in ice covered areas.

CryoSat-2, launched in 2010, is specifically designed to overcome the challenges of performing pulse-limited altimetry over Earth's polar regions. With a high inclination, drifting orbit, and novel instrumentation which exploits interferometry to obtain high spatial resolution measurements in areas of steep terrain, CryoSat-2 provides a high density network of elevation measurements up to latitudes of 88 degrees (Wingham et al., 2006). Here, we utilise a 6-year time series of elevation measurements acquired by CryoSat-2 between July 2010 and July 2016 to derive a comprehensive and contemporary DEM of Antarctica at a spatial resolution of 1 km, with high data coverage in both the ice sheet interior and its complex marginal areas. We then evaluate the

accuracy of the generated DEM against a set of contemporaneous airborne laser altimeter measurements, obtained during NASA Operation IceBridge campaigns, in several locations covering Antarctica's ice sheet and ice shelves. The DEM we describe here features several improvements over the preliminary ESA CryoSat-2 Antarctic DEM distributed in March 2017, and should be used in its place. These improvements include an increase in resolution from 2 km to 1 km, an increase in data coverage on the grounded ice sheet from 91 % to 94 %, and the use of a more robust ordinary kriging interpolation scheme to provide a continuous elevation dataset.

2.2 Data and methods

2.2.1 CryoSat-2 elevation measurements

We use 6 years of CryoSat-2 Baseline-C Level 2 measurements of surface elevation recorded by the SIRAL (SAR Interferometer Radar Altimeter) instrument, mounted on the CryoSat-2 satellite, between July 2010 and July 2016. Over Antarctica, SIRAL samples the surface in two operating modes: Low Resolution Mode (LRM) and Synthetic Aperture Radar Interferometric mode (SARIn). In LRM, Cryosat-2 operates as a conventional pulse-limited altimeter (Wingham and Wallis, 2010), illuminating an area of approximately 2.2 km^2, with an across track width of roughly 1.5 km. LRM is used in the interior of the ice sheet, where low slopes and homogenous topography on the footprint scale are generally well suited for pulse-limited altimetry.

In SARIn, SIRAL uses two receive antennae to perform interferometry, allowing the location of the point of closest approach (POCA) to be precisely determined in the across-track plane (Wingham et al., 2004). Bursts of 64 pulses are emitted at a high Pulse Repetition Frequency, and Doppler processing is then used to reduce the along-track footprint to approximately 300 m (Wingham et al., 2006). This increased sampling density, and ability to calculate the along- and across-track location of the POCA, make SARIn well suited for measuring the steep and complex topography found in the ice sheet margins.

The CryoSat-2 Level 2 elevation product has a series of geophysical corrections applied to correct the selected measurements for the following: off-nadir ranging due to slope,

dry atmospheric propagation, wet atmospheric propagation, ionosphere propagation, solid earth tide and ocean loading tide (ESA, 2012). As part of the Level 2 processing chain, elevation measurements recorded in LRM are slope corrected by relocating the echoing point away from nadir in accordance with the surface slope, determined using an external DEM (Radarsat Antarctic Mapping Project version 2 DEM, posted at 200 m) (ESA, 2012; Liu et al., 2001). SARIn acquisitions are slope corrected using the interferometric phase difference calculated at the location of the elevation measurement. For the ice shelves, additional inverse barometric and ocean tide corrections are also applied.

Within the LRM mode mask area we select Level 2 elevation estimates retrieved using the Offset Centre of Gravity (OCOG) retracking algorithm, which defines a rectangular box around the centre of gravity of an altimeter waveform based upon its power distribution (Wingham et al., 1986). The OCOG retracking point is taken to be the point on the leading edge of the waveform which first exceeds 30 % of the rectangle's amplitude (Davis, 1997). We use the OCOG retracker as it offers robust retracking over a wide range of surfaces, and is adaptable to a variety of pulse shapes (Armitage et al., 2014; Davis, 1997; Wingham et al., 1986). For the SARIn area, where CryoSat-2 operates as a SAR altimeter and waveform characteristics differ from those acquired in LRM, elevations are retrieved using the ESA Level 2 SARIn retracker, which determines the retracking correction from fitting the measured waveform to a modelled SAR waveform (ESA, 2012; Wingham et al., 2006). Over the ice sheet and ice shelves, we use approximately 2.5 x 10^8 CryoSat-2 elevation measurements to derive the new DEM.

2.2.2 DEM generation

To compute elevation, we separate the input CryoSat-2 elevation measurements into approximately 1.4 x 10^7 regularly spaced 1 km^2 geographical regions. We then use a model fit method to separate the various contributions to the measured elevation fluctuations within each region (Flament and Rémy, 2012; McMillan et al., 2014). This method best suits CryoSat-2's 369-day orbit cycle, which samples along a dense network of ground tracks with few coincident repeats. We model the elevation Z (Eq. 2.1) as a quadratic function of local surface terrain (x,y), a time invariant term h accounting

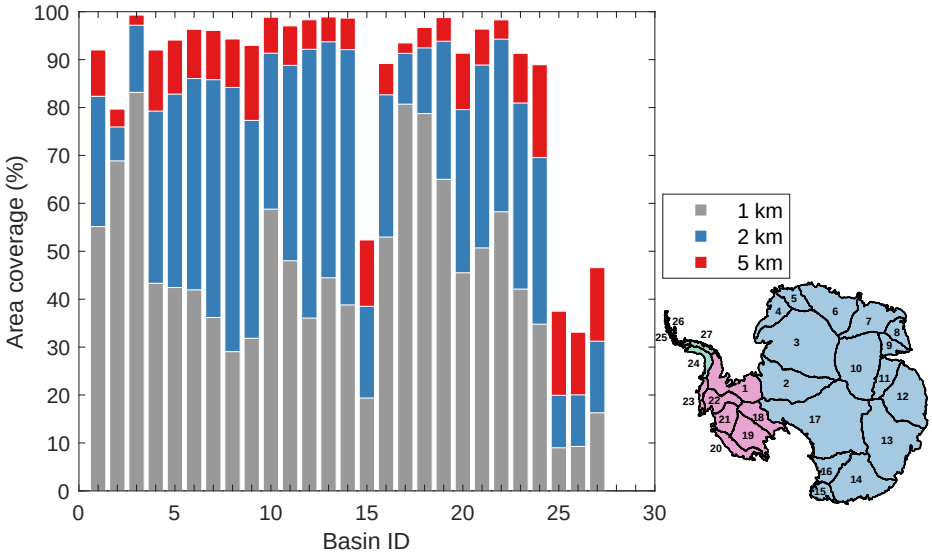

Figure 2.1: Area coverage of elevation values provided by the model fit solution (Eq. 2.1) of CryoSat-2 measurements for the Antarctic Ice Sheet, with a grid cell sizing of 1 km^2, 2 km^2 and 5 km^2. Solid black lines and numbers (inset) show the boundaries and ID numbers of the 27 drainage basins used (Zwally et al., 2012). East Antarctica and the Antarctic Peninsula are defined as numbers 2 to 17 and 24 to 27, respectively, and the remaining numbers define West Antarctica.

for anisotropy in radar penetration depth depending on satellite direction (Armitage et al., 2014), and a linear rate of elevation change with time t. The satellite heading term, h, is a binary term set to 0 or 1 for an ascending or descending pass, respectively.

$$Z(x,t,y,h) = \bar{z} + a_0 x + a_1 y + a_2 x^2 + a_3 y^2 + a_4 xy + a_5 h + a_6 (t - t_{July2013}) \quad (2.1)$$

We retrieve the model coefficients in each grid cell using an iterative least-squares fit to the observations to minimise the impact of outliers, and discard unrealistic estimates resulting from poorly constrained model fits. At a spatial resolution of 1 km this approach provides, on average, in excess of 30 elevation measurements per grid cell to constrain each solution. By using the model fit method, we are able to generate elevation estimates from 6 years of continuous Cryosat-2 data, which are not unduly

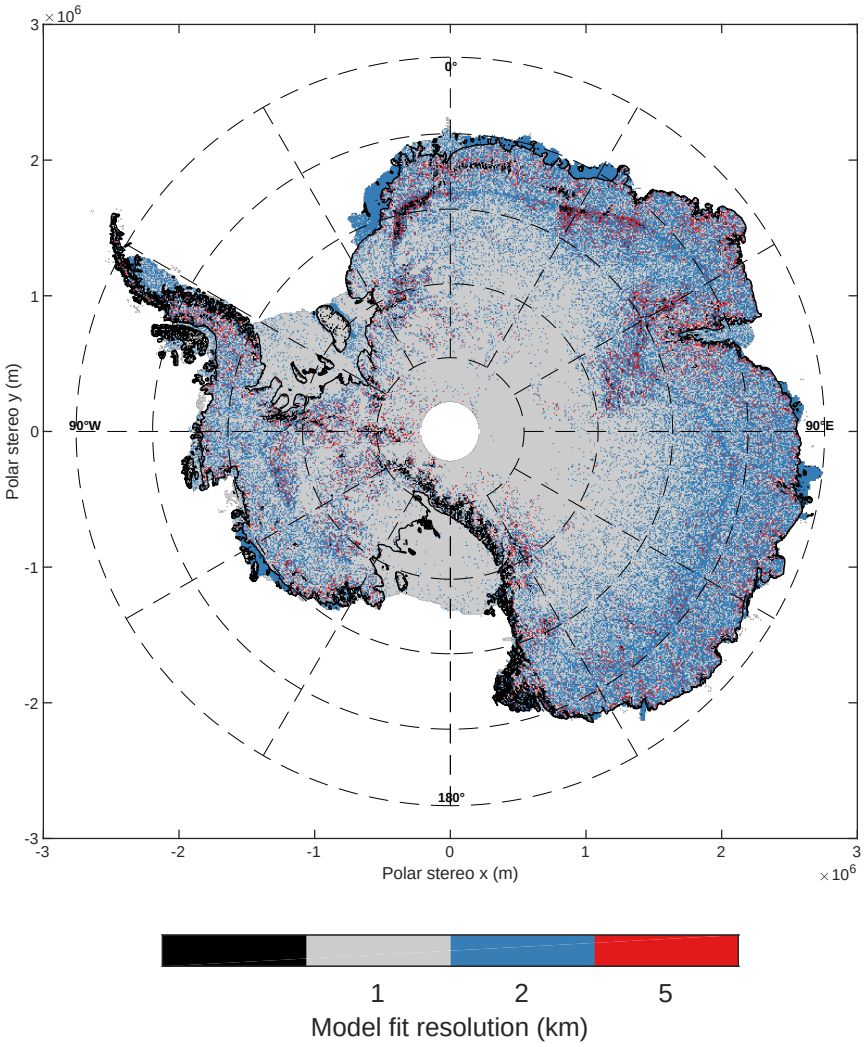

Figure 2.2: The grid cell resolution of the model fit method used to derive the surface elevation in each 1 km grid cell. Elevation values obtained from the 2 km and 5 km model fits are oversampled to the modal DEM resolution of 1 km. A black grid cell denotes a cell that contains an interpolated value. For the grounded ice sheet, approximately 60 %, 30 % and 5 % of elevation values are derived from 1, 2 and 5 km model fits, respectively. For the ice shelves, 75 % of elevations are calculated with 1 km model fits, and 23 % from 2 km model fits. The remaining 5 % of ice sheet and 2 % of ice shelf values are interpolated using ordinary kriging. At the mode mask boundary, where CryoSat-2 switches between LRM and SARIn operating modes, grid cells are predominantly derived from 2 km model fits, as there are a reduced number of elevation measurements available to constrain model fits at a resolution of 1 km.

affected by fluctuations in surface elevation that may occur during the acquisition period (McMillan et al., 2014). In addition, it also allows for the retrieval of ice sheet elevation and rate of elevation change from the same data in a self-consistent manner.

We form the DEM from the mean elevation term, $\bar{z}$, in Eq. (2.1) within each 1 x 1 km grid cell, which corresponds to the elevation at the midpoint of the observation period. At a resolution of 1 km, the model fit provides an elevation estimate in 60 % and 75 % of grid cells within the total area of the ice sheet and ice shelves, respectively. To fill data gaps in the 1 km grid, we generate additional DEMs of Antarctica from model fits at spatial resolutions of 2 km and 5 km. At these coarser resolutions more data are available to constrain model fits within a given geographical region, particularly at lower latitudes where the spacing between ground tracks is larger. As a result, for the ice sheet the data coverage for DEMs generated at resolutions of 2 km and 5 km is increased to 91 % and 94 %, respectively (Figure 2.1). For the ice shelves we use an additional DEM generated from model fits at a resolution of 2 km, for which data coverage is increased to 98 %. Data gaps in the 1 km grid are filled by the re-sampled 2 km and 5 km DEMs (where neither 1 km or 2 km model fit estimates are available) for the ice sheet, and the 2 km DEM for the ice shelves (Figure 2.2). This approach provides a DEM at the modal spatial resolution of 1 km, where approximately 94 % and 98 % of grid cells contain an elevation estimate derived from CryoSat-2 measurements for the ice sheet and ice shelves, respectively.

In order to provide a continuous dataset, we estimate elevation values in grid cells North of 88 ° S that contain no data using ordinary kriging (Isaaks and Srivastava, 1989; Kitanitis, 1997), an interpolation technique used in the generation of previously published DEMs (Bamber et al., 2009; Helm et al., 2014). We interpolate using a search radius of 10, 25 or 50 km, depending on which first satisfies a minimum threshold of 100 data points to be used in the interpolation. Over the grounded ice sheet, 44 %, 52 % and 4 % of interpolated elevation values used a search radius of 10, 25 and 50 km, respectively. The majority of data points requiring a search radius of 50 km are located along the margins of Graham Land and Palmer Land in the Antarctic Peninsula, where data coverage is poor. After interpolation, the DEM provides a continuous elevation dataset for the ice shelves and ice sheet for latitudes north of 88 ° S. We have chosen

not to interpolate the pole hole due to interpolation distances exceeding the maximum kriging search radius of 50 km, and a desire to keep the DEM a product of CryoSat-2 data only.

2.2.3 Airborne elevation measurements

To evaluate the accuracy of the DEM, we compare our elevation estimates to measurements acquired by airborne laser altimeters during NASA's Operation IceBridge survey. The IceBridge mission, running since 2009, is the largest airborne polar survey ever undertaken (Koenig et al., 2010). The primary goal of IceBridge is to maintain a continuous time series of laser altimetry over the Arctic and the Antarctic, bridging the gap between ICESat, which stopped collecting data in 2009, and ICESat-2, launched in 2018.

We compare the DEM to elevation measurements obtained by two airborne laser altimeter instruments (Figure 2.3):

- The Airborne Topographic Mapper (ATM), over the following regions of the continental ice sheet: Antarctic Peninsula, Bellingshausen, Amundsen and Getz sectors of West Antarctica, and the Transantarctic Mountains, Oates Land and the plateau region of East Antarctica. The following ice shelves were also surveyed: Larsen C, Pine Island, Thwaites, Wilkins, Abbot, Getz, George VI, Ross and Filchner-Ronne. Measurements were acquired between March 2009 and December 2014 (Krabill, 2016).

- The Riegl Laser Altimeter (RLA), over the Antarctic Peninsula, Marie Byrd Land of West Antarctica, Dronning Maud Land, Totten Glacier and Wilkes Land of East Antarctica, and the Ross ice shelf. Measurements were acquired between December 2008 and January 2013 (Blankenship et al., 2013).

The ATM is an airborne scanning laser altimeter capable of measuring surface elevation with an accuracy of 10 cm or better (Krabill et al., 2004). Flown at a typical altitude of 500 m above ground level, the ATM illuminates a swath width of approximately 140 m, with a footprint size of 1-3 m and along track separation of 2 m (Levinsen et al., 2013).

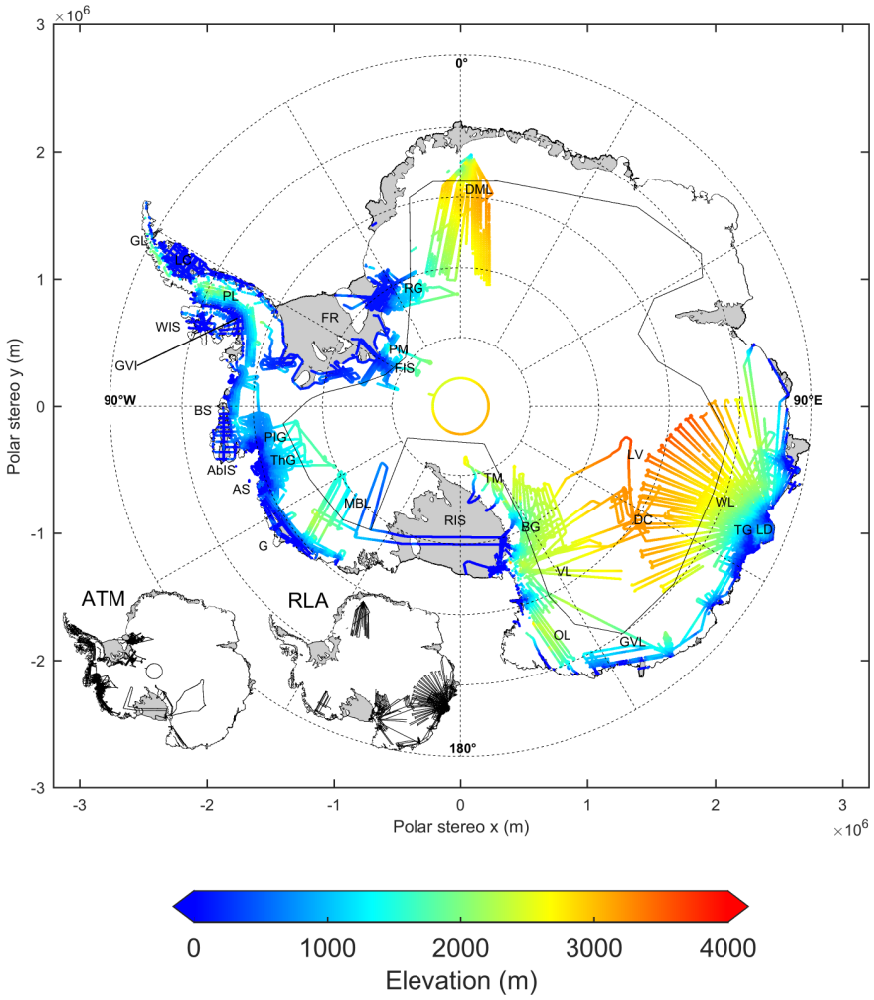

Figure 2.3: IceBridge airborne dataset used to evaluate the DEM, acquired between December 2008 and December 2014. The mode mask boundary (solid black line) between CryoSat-2 LRM and SARIn modes is also shown. (inset) Locations of the individual ATM and RLA airborne datasets. Labelled are the following locations of interest: AbIS: Abbot Ice Shelf, AS: Amundsen Sea, BS: Bellingshausen Sea, BG: Byrd Glacier, DC: Dome C, DML: Dronning Maud Land, FIS: Foundation Ice Stream, FR: Filchner-Ronne Ice Shelf, G: Getz, GL: Graham Land, GVI: George VI Ice Shelf, GVL: George V Land, LC: Larsen-C Ice Shelf, LD: Law Dome, LV: Lake Vostok, MBL: Marie Byrd Land, OL: Oates Land, PIG: Pine Island Glacier, PL: Palmer Land, PM: Pensacola Mountains, RG: Recovery Glacier, RIS: Ross Ice Shelf, TG: Totten Glacier, ThG: Thwaites Glacier, TM: Transantarctic Mountains, VL: Victoria Land, WIS: Wilkins Ice Shelf, WL: Wilkes Land.

Data acquired by the RLA were collected as part of the NASA ICECAP program from December 2009 to 2013, mounted to a survey aircraft flown at a typical height of 800 m. Elevation measurements are provided at a spatial resolution of 25 m along track and 1 m across track with an error of approximately 12 cm (Blankenship et al., 2013).

In total, we selected approximately 2.3 x 10^7 laser altimeter elevation measurements, comprising of 1.7 x 10^7 ATM measurements, and 0.6 x 10^7 RLA measurements. Combined, these data provide an independent comparison dataset, obtained over a contemporaneous time period and in a wide range of locations across Antarctica. For all airborne measurements, a filter was applied to remove any erroneous step changes in elevation resulting from the laser altimeter ranging from cloud cover (Kwok et al., 2012; Young et al., 2008).

2.2.4 DEM evaluation

When comparing the DEM and airborne laser altimeter datasets, we separate the evaluation results according to whether the IceBridge elevation measurement resides in a grid cell derived from CryoSat-2 surface height measurements, hereby referred to as an observed grid cell, or an interpolated elevation value. This approach allows the accuracy of CryoSat-2 observations and the chosen interpolation method to be assessed independently. In total, approximately 84 % of the airborne laser elevation measurements reside within an observed DEM grid cell. Of this total, 53 %, 41 % and 6 % grid cells are derived from 1, 2 and 5 km model fits, respectively.

In order to compare the DEM and IceBridge datasets, we estimate the DEM elevation at the exact location of the airborne laser altimeter measurement through bilinear interpolation. Subsequently, we subtract the IceBridge elevation from the interpolated DEM elevation and collate the elevation differences into the same 1 x 1 km grid that the DEM is projected on. We then calculate the median difference to obtain one elevation difference for each individual grid cell, and to minimise the impact of outliers. On average, 1 km DEM grid cells overflown by IceBridge campaigns contain 70 individual airborne measurements. In total, elevation differences were compared for approximately 2.7 x 10^5 DEM grid cells, covering 2% of the total ice sheet and ice shelf

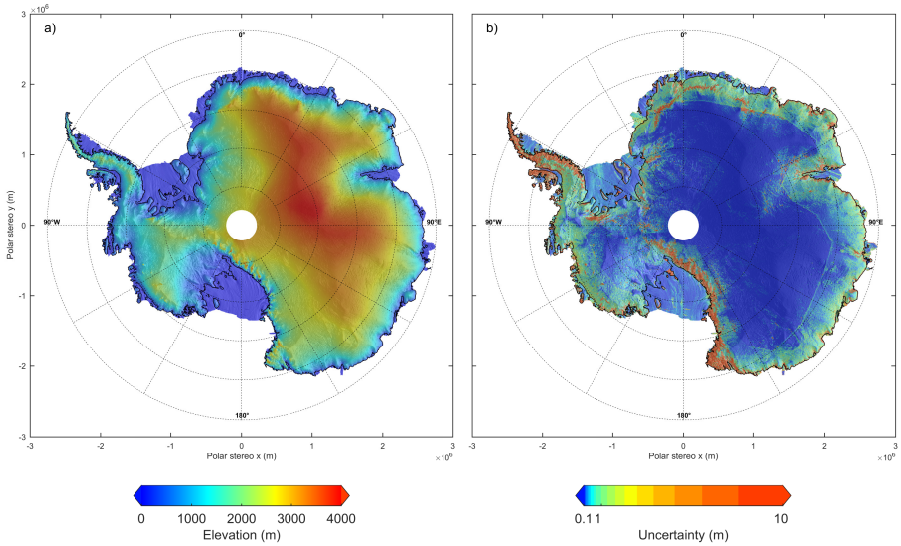

Figure 2.4: (a) A new elevation model of Antarctica derived from 6 years of CryoSat-2 radar altimetry data acquired between July 2010 and July 2016, and (b) uncertainty map of the new CryoSat-2 Antarctic DEM, calculated from root mean square difference of elevation residuals in observed grid cells, and the kriging variance error in interpolated grid cells. Uncertainties due to radar penetration into a dry snowpack are not accounted for.

area, respectively. All DEM and IceBridge elevations are referenced to the WGS84 ellipsoid.

2.3 Results

Our new DEM of Antarctica (Figure 2.4) provides an elevation value derived from CryoSat-2 measurements for 94 % of the grounded ice sheet and 98 % of the ice shelves. The remaining 5 % of grid cells North of 88 ° S are interpolated using ordinary kriging to provide a continuous gridded elevation dataset for the entire continent beyond the pole hole. Accounting for the length of the elevation time series within each individual grid cell, we determine the effective time stamp of the DEM to be July 2013. Surface

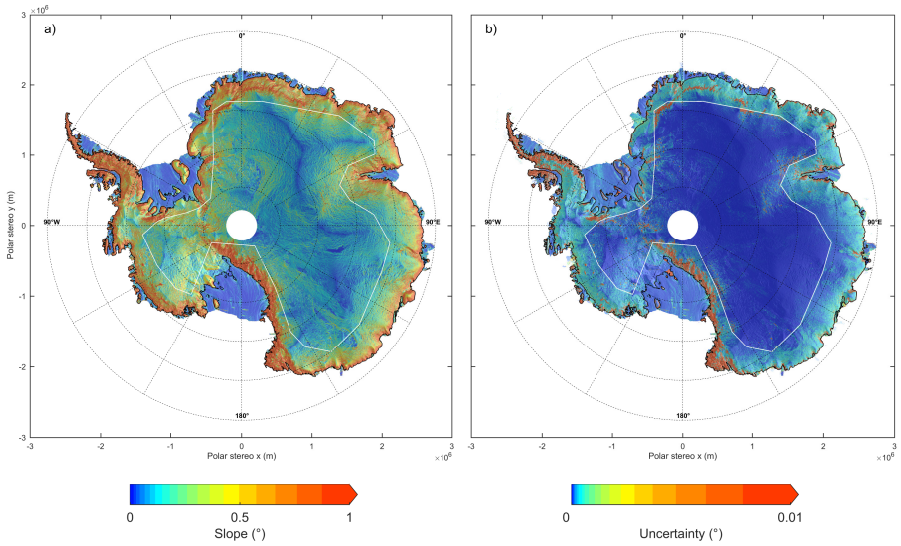

Figure 2.5: (a) Surface slopes of Antarctica posted at a resolution of 1 km, derived from the digital elevation model, and (b) estimated uncertainty of surface slope, derived through propagation of the elevation uncertainties. The mode mask boundary between CryoSat-2 LRM and SARIn modes is also shown in white.

slopes derived from the elevation gradient of the DEM (Figure 2.5) illustrate the short scale topographic undulations, and identify the ice divides and larger features such as subglacial Lake Vostok.

To evaluate the DEM's systematic bias we compute the median elevation difference with respect to the airborne measurements, as this is robust against the effect of outliers. To evaluate its random error, we calculate the root mean square (RMS) difference. Both of these statistical measures are more appropriate than the mean and standard deviation when describing the systematic bias and random error, respectively, of the non-Gaussian distributions we typically find when calculating elevation differences between the DEM and IceBridge elevation datasets.

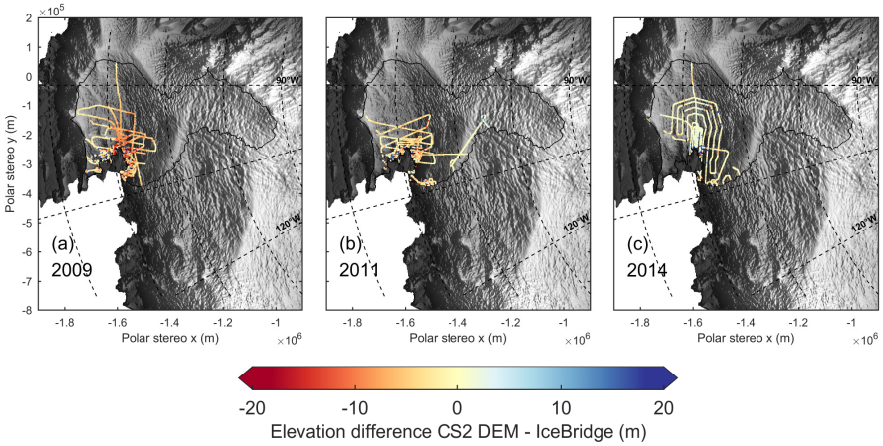

Figure 2.6: Difference between observed DEM grid cells derived from 1 km model fits and IceBridge ATM elevation measurements for the Pine Island Glacier region in West Antarctica for ATM flight surveys undertaken in the years (a) 2009, (b) 2011 and (c) 2014. The DEM has an effective time stamp of July 2013. The boundary of the Pine Island Glacier drainage basin (solid black line) is also shown (Zwally et al., 2012).

2.3.1 Comparison of DEM to airborne elevation measurements: observed grid cells

A primary objective of NASA's IceBridge program is to maintain a continuous observational record of rapidly changing areas in Antarctica. As a result, elevation measurements were obtained in regions such as Pine Island (PIG), Thwaites and Totten Glaciers, where the observed thinning rate is of the order of several metres per year (McMillan et al., 2014). Therefore, we expect to see height differences between the DEM and airborne datasets due to real changes in surface elevation between their respective acquisition periods. Comparing DEM elevations at PIG against measurements acquired by ATM flights in the years 2009, 2011 and 2014 (Figure 2.6), the elevation difference is smallest in 2014, closest to the DEM effective date of July 2013 (Table 2.1).

To account for the temporal difference between the two datasets, we adjust the interpolated DEM value for changes in surface elevation which may have occurred between the acquisition periods. We calculate this adjustment by interpolating the gridded ele-

Year	Number of compared grid cells	Median difference (m)	RMS difference (m)
2009	3490	−4.97	11.35
2011	2819	−2.08	8.56
2014	2794	0.05	3.97

Table 2.1: Statistics of the comparison between observed DEM grid cells derived from 1 km model fits, and ATM elevation measurements in the Pine Island Glacier drainage basin. The airborne data are separated into the year of acquisition to demonstrate the effect of ice dynamical thinning in this region on the elevation difference. The effective date of the DEM is July 2013.

vation trends (Eq. 2.1) to the location of the airborne measurement, through the same bilinear interpolation method as used for the DEM elevation estimate. The elevation change trends were corrected for temporal fluctuations in backscatter, which can introduce spurious signals in time series of elevation change, by adjusting the elevation time series according to the correlation between changes in elevation and backscattered power (Davis and Ferguson, 2004; Khvorostovsky, 2012; Wingham et al., 1998).

At the continental scale, there is generally good agreement between the DEM and airborne laser altimeter measurements (Figure 2.7, Figure 2.8), and the median and RMS elevation difference between the DEM and airborne data are −0.27 m and 13.36 m, respectively (Table 2.2).

At the Antarctic Peninsula, the median and RMS difference are −1.12 m and 22.40 m, respectively; errors are larger in this region due to its mountainous and highly variable terrain, and it remains a challenge for radar altimetry. The largest elevation differences in this region are found in DEM grid cells derived from 5 km model fits, indicating that the complex topography is poorly described by a quadratic model at this resolution. In grid cells with elevation values derived from 1 km model fits, which accounts for 40 % of the Antarctic Peninsula DEM, the median and RMS difference are improved to −0.71 m and 16.88 m, respectively. Geographically, elevation differences rise towards Graham Land at the northern tip of the Antarctic Peninsula, where topography is complex and highly variable at length scales similar to the satellite footprint.

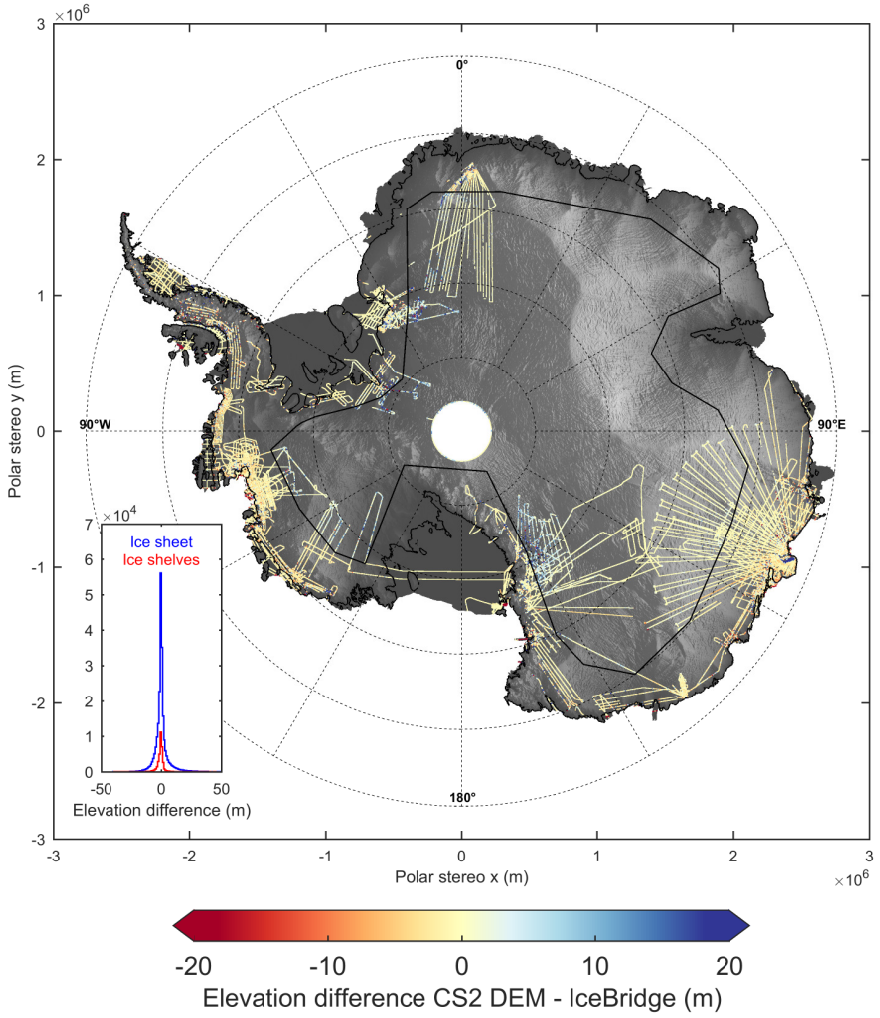

Figure 2.7: Difference between CryoSat-2 DEM elevation and airborne laser altimeter measurements in observed grid cells. The mode mask boundary between CryoSat-2 LRM and SARIn modes is also shown as a solid black line. (inset) Distribution of the elevation differences (DEM – airborne) for the ice sheet and ice shelves.

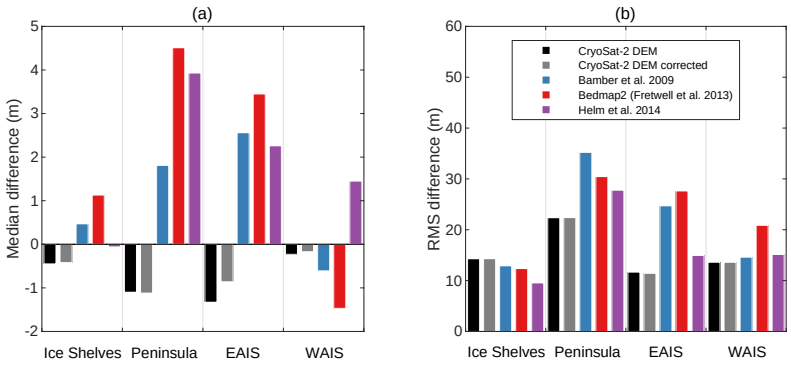

Figure 2.8: (a) Median and (b) RMS differences between airborne elevation measurements calculated over the ice shelves, Antarctic Peninsula, West Antarctica (WAIS) and East Antarctica (EAIS) for the new CryoSat-2 DEM presented in this report, and three publicly available Antarctic DEMs. CryoSat-2 DEM comparisons with the elevation change correction applied (Table 2.2) are plotted as grey bars.

In West Antarctica there is good agreement between the DEM and airborne measurements, particularly along the coastal margins of the Bellingshausen and Amundsen Seas. In the Bryan and Eights Coasts in the Bellingshausen Sea Sector, the median and RMS difference are -1.72 m and 10.40 m, respectively. At Pine Island and Thwaites Glaciers, and their surrounding drainage area, the median difference is -1.02 m, and the RMS difference is 10.58 m. Further inland towards Marie Byrd Land, the median and RMS differences are 0.20 m and 5.27 m, respectively.

In East Antarctica, the DEM compares well to the airborne dataset inland in the plateau region where slopes are low, and the topography is well suited to satellite radar altimetry. Along the George V coast and in George V Land, the median difference is -0.68 m, and the RMS difference 6.52 m. Over Totten glacier and its catchment area, the median and RMS difference are -0.39 m and 16.15 m respectively. In this region, there is good agreement with airborne elevations both inland towards Dome C, and over Totten glacier itself. On the eastern flank of Law Dome, biases of several tens of metres between the DEM and the airborne data coincide with grid cells derived from 5 km model fits, where there is insufficient data to constrain models at higher spatial resolutions. As a result, elevations derived from 5 km model fits will poorly sample the

Region	**Observed** Number of compared grid cells	Median difference (m)	RMS difference (m)	**Interpolated** Number of compared grid cells	Median difference (m)	RMS difference (m)
Ice sheet	230165	−0.27	13.36	32933	25.37	138.62
Ice shelves	40081	−0.42	14.31	4772	1.20	30.96
Antarctic Peninsula	6820	−1.12	22.40	7473	82.21	191.07
West Antarctica	60452	−0.86	11.43	8783	11.78	96.15
East Antarctica	162893	−0.17	13.60	14679	19.62	117.77
LRM	73867	0.26	7.15	1683	6.51	41.70
SARIn (ice sheet only)	156298	−0.82	15.45	31250	28.65	141.97
Total	270246	−0.30	13.50	37655	19.84	131.13

Table 2.2: Statistics of the comparison between observed and interpolated DEM grid cells and airborne elevation measurements for individual Antarctic regions and mode mask areas. In total, only 5 % and 2 % of DEM elevation values are obtained through interpolation for the ice sheet and ice shelves, respectively.

highly sloping terrain in this region when compared to the airborne laser. Additionally, in East Antarctica, elevation differences several tens of metres in magnitude over the Pensacola Mountains occur where high surface slopes and nunataks complicate radar altimeter elevation retrievals.

At the Antarctic ice shelves, the DEM also compares favourably to the airborne elevation data, with median and RMS differences of −0.42 m and 14.31 m, respectively. Differences are most pronounced near to grounding lines where tidal effects are relatively large and where the terrain is generally more complex, and are smallest in the interior of the larger ice shelves, which are generally flat. At the Ross and Filchner-Ronne Ice Shelves, for example, the RMS differences are 3.93 and 3.54 m, respectively — considerably lower than the continental average.

Overall, the median and RMS differences between the DEM and airborne measurements are −0.30 m and 13.50 m, respectively, and 99 % of the data agree to within 45 m. In addition to temporal mismatch, possible explanations for residual elevation differences include differences in the satellite and airborne altimeter footprint sizes and scattering horizons, as well as errors in the individual data sets themselves. Although generally small, biases between the DEM and the airborne data are notably high in

Slope (°)	**LRM** RMS difference (m)	LRM area coverage (km^2)	**SARIn** RMS difference (m)	SARIn area coverage (km^2)
0 - 0.25	4.90	5481579	6.37	1373258
0.25 - 0.5	11.24	975624	8.54	1338826
0.5 - 0.75	19.85	143420	13.50	775083
> 0.75	29.59	93660	24.26	1551836

Table 2.3: RMS differences between observed DEM grid cells airborne elevation measurements for four slope bands, separated into the LRM and SARIn mode mask areas for the Antarctic Ice Sheet. The area of each region represented by the four slope bands is also provided.

several isolated regions, including the upstream catchments of the Byrd Glacier flowing from East Antarctica into the Ross Ice Shelf, the Recovery Glacier flowing from East Antarctica into the Filchner Ice Shelf, and the Foundation Ice Stream in the Pensacola mountains (see Figure 2.7). In each of these locations, surface slopes are high (exceeding 1 °) and CryoSat-2 operates in Low Resolution Mode (see Figure 2.5). To illustrate this in more detail, we compare elevation recorded along two RLA tracks falling within the LRM zone (Figure 2.9); one at Byrd Glacier where slopes are high and undulating, and another 600 km northward in Victoria Land where slopes are low and smooth. Along these tracks, elevation differences of approximately 20 m occur where the terrain undulates rapidly, because CryoSat-2 under samples the topographic depressions when operating in LRM. Despite being well sampled by the airborne laser altimeter dataset, regions of high surface slopes represent a small fraction of the area surveyed by CryoSat-2 in either LRM or SARIn modes (Table 2.3). In contrast, agreement between DEM and IceBridge elevations in regions of lower surface slope (less than 0.5 °) — which represent the majority of the ice sheet — falls typically in the range 5 to 10 m in either operating mode (Table 2.3). Combining the slope-dependent errors (Table 2.3) and the distribution of slopes within the LRM and SARIn mode masks, we estimate the average uncertainty of the observed DEM to be 9.5 m.

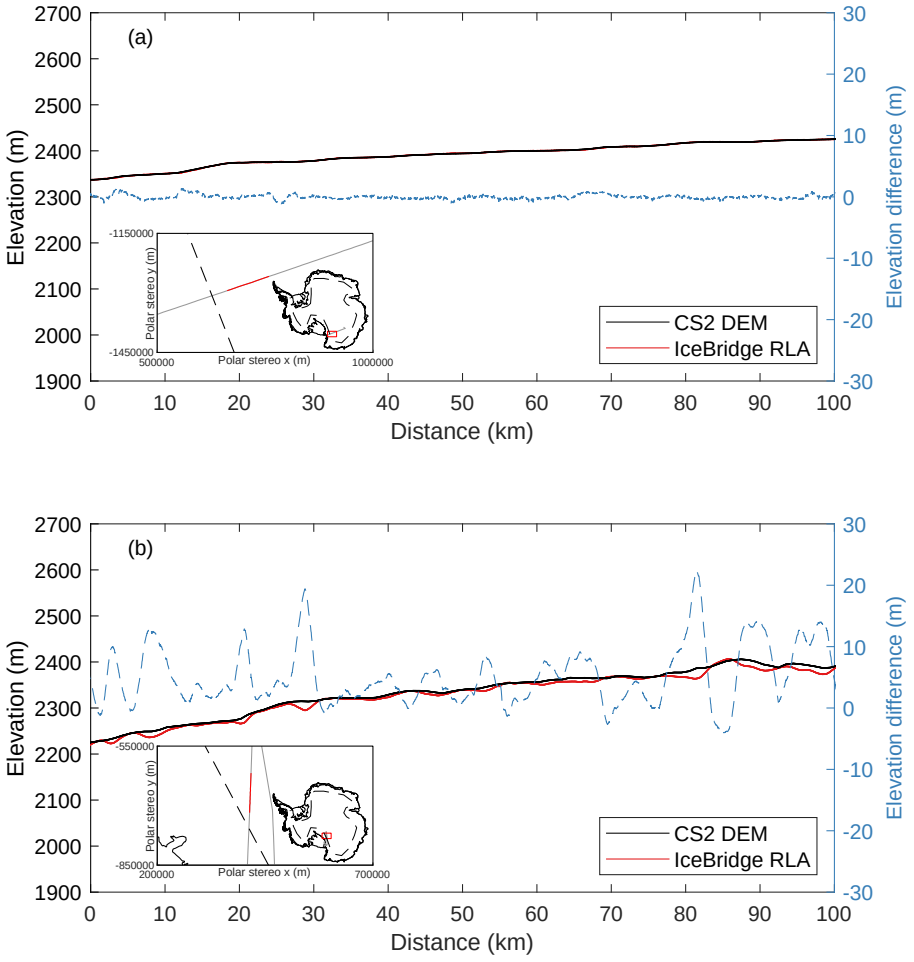

Figure 2.9: CryoSat-2 LRM, and IceBridge RLA elevation profiles for 100 km flight path sections obtained in (a) Victoria Land, where surface slopes are low, and (b) inland from Byrd Glacier, where surface slopes are high. Elevation differences (CS2 DEM – airborne) are plotted in blue to the right hand scale. (Inset) locations of RLA flight paths, with the profile section highlighted in red. The LRM/SARIn mode mask boundary is shown as a dashed line.

2.3.2 Comparison of DEM to airborne elevation measurements: interpolated grid cells

A small proportion (5 %) of the DEM is estimated by ordinary kriging, and we assess the accuracy of this method by comparing airborne elevation measurements residing in a DEM grid cell containing no data with the interpolated value (Table 2.2). Predictably, our interpolated DEM values deviate more from the airborne elevation measurements in areas of high slope and complex terrain, where internal tracker losses occur and data coverage is reduced. This is true in particular for the ice sheet margins and the Antarctic Peninsula, where there is little spatial correlation over the 10, 25 and 50 km search distances we have chosen for the interpolation, and limited data coverage available for sampling. At the Antarctic Peninsula, where the majority of interpolated grid cells are located in the bare rock regions on the north coasts of Graham and Palmer Land, the median and RMS difference are 82.21 m and 191.07 m, respectively. Similarly, in East Antarctica, where the median and RMS difference are 19.62 m and 117.77 m, respectively, interpolated grid cells are primarily found in the rugged, bare rock terrain across the Transantarctic Mountains, the Victory Mountains in Victoria Land, and the mountain ranges in Oates Land.

The largest interpolation errors are located in empty grid cells at the boundary of the ice sheet along the margins, as data gaps are filled through extrapolation from data inland rather than interpolation between known values. Over higher elevation regions with relatively smooth topography it is more reasonable to assume spatial correlation over interpolation distances of 10 to 50 km, and our chosen interpolation method is more reliable. Within the LRM zone, the median and RMS difference are 6.51 m and 41.70 m, respectively. We note that, because the elevation rate is unknown where there is no model solution, we have not corrected for temporal changes in elevation between the acquisition periods of the two datasets within our evaluation of interpolated grid cells. As a result, the reported values represent an upper bound of the elevation difference which includes errors due to both interpolation and elevation change — if present within an interpolated grid cell.

2.3.3 Comparison of currently available DEMs

We compare the accuracy of the new CryoSat-2 DEM over the ice shelves, Antarctic Peninsula, West Antarctica and East Antarctica with three other publicly available Antarctic DEMs: Bedmap2 (Fretwell et al., 2013), and DEMs generated from ERS-1 and ICESat data (Bamber et al., 2009), and CryoSat-2 data (Helm et al., 2014). To ensure an equivalent comparison dataset, we only use airborne elevation measurements which reside in an observed grid cell of the presented CryoSat-2 DEM (see Figure 2.7). For all four DEMs we use the same evaluation method as described in Section 2.2.4. From the calculated median and root mean squared differences, the new CryoSat-2 DEM we present here is comparable to, or an improvement upon currently available DEMs in all four regions (Figure 2.8). In areas of high rates of elevation change, it is worth noting that all four DEMs will exhibit larger biases due to real changes in surface elevation between the acquisition periods of the respective datasets, and that these differences may be larger in the DEMs containing older ERS-1 and ICESat data (Bedmap2, Bamber et al. (2009)).

Similarly, median and root mean squared differences calculated with respect to surface slope for each DEM within the Antarctic Ice Sheet (Figure 2.10), further illustrate the improvement offered by the new CryoSat-2 DEM, and the slope-dependency of DEM accuracy. We limit this analysis to regions where surface slopes are lower than 1.5 °, which accounts for approximately 94 % of the Antarctic Ice Sheet area North of 88 ° S. In addition, we note that the spatial distribution of the airborne dataset used for comparison within the grounded ice sheet preferentially samples regions of high slope and low elevation, and does not reflect the overall elevation and slope distributions of the Antarctic Ice Sheet. Approximately 60 % of DEM grid cells overflown by IceBridge survey craft have an elevation of less than or equal to 1000 m, and 43 % have a surface slope greater than 0.5 °. In comparison, approximately 15 % and 22 % of the Antarctic Ice Sheet area has elevations of less than 1000 m and slopes greater than 0.5 °, respectively.

Although another recent DEM of Antarctica (Fei et al., 2017) formed using 1.7 x 10^7 elevation measurements acquired by CryoSat-2 between 2012 and 2014 is not available

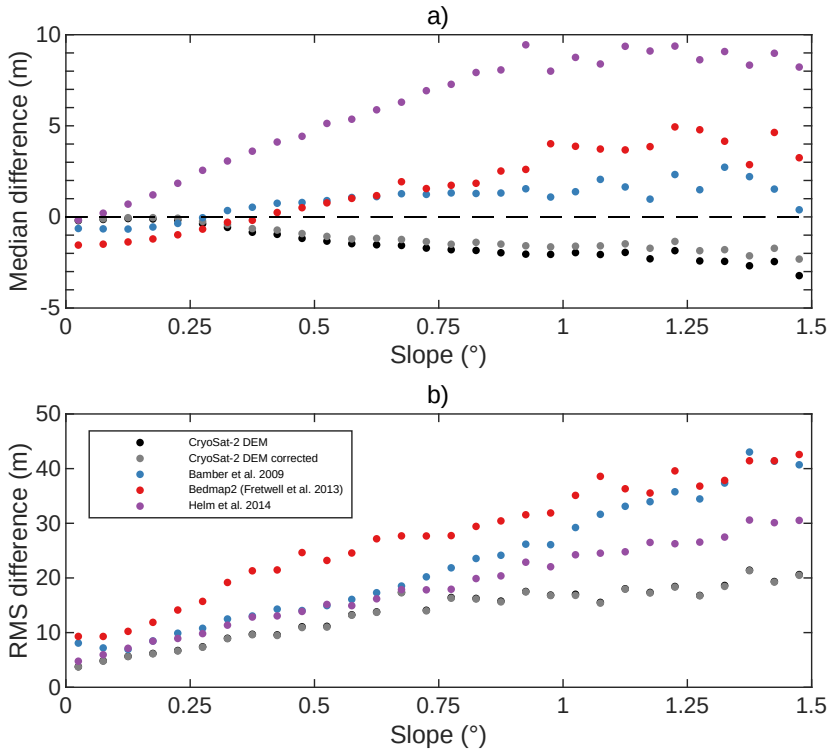

Figure 2.10: (a) Median and (b) RMS differences between airborne elevation measurements calculated for grid cells within the Antarctic Ice Sheet, binned with respect to surface slope at a bin size of 0.05 °, the new CryoSat-2 DEM presented in this report, and the three publicly available Antarctic DEMs used for comparison. CryoSat-2 DEM differences with the elevation change correction applied are plotted in grey.

for direct assessment, it has a reported accuracy of approximately 1 m for the high elevation region at the Domes, 4 m for the ice shelves and over 150 m for mountainous and coastal areas.

2.4 Conclusions

We present a new DEM of Antarctica derived from a spatio-temporal analysis of CryoSat-2 data acquired between July 2010 and July 2016. The DEM is posted at a modal resolution of 1 km and contains an elevation measurement in 94 % and 98 % of

ice sheet and ice shelf grid cells, respectively; elevation in a further 5 % of the domain is estimated via ordinary kriging. We evaluate the accuracy of the DEM through comparison to an extensive independent set of airborne laser altimeter elevation measurements, acquired over a contemporaneous time period and in a wide range of locations across the Antarctic Ice Sheet and ice shelves. From a comparison at grid cells acquired in both data sets, the median and RMS difference between the DEM and airborne data are −0.30 m and 13.50 m, respectively. The largest elevation differences occur in areas of high slope and where CryoSat-2 operates in Low Resolution Mode, where the altimeter ranges to the peaks of undulating terrain and under samples troughs. Using the slope-dependent uncertainties and the wider distribution of slopes, we estimate the overall accuracy of the DEM to be 9.5 m where elevations are formed from satellite data alone. In areas where the DEM is interpolated, the median and RMS differences rise to 19.84 m and 131.13 m, respectively. Through comparisons to an equivalent validation dataset in four individual Antarctic regions, we find the new CryoSat-2 DEM to be comparable to, or an improvement upon, three publicly available and widely used Antarctic DEMs.

References

Armitage, T. W. K., Wingham, D. J., and Ridout, A. L. (2014). Meteorological origin of the static crossover pattern present in low-resolution-mode CryoSat-2 data over central Antarctica. *IEEE Geoscience and Remote Sensing Letters*, 11(7):1295–1299. 46, 47

Bamber, J. L., Gomez-Dans, J. L., and Griggs, J. A. (2009). A new 1 km Digital Elevation Model of the Antarctic derived from combined satellite radar and laser data – Part 1: Data and methods. *The Cryosphere*, 3(1):101–111. 44, 49, 63

Blankenship, D. D., Young, D. D., Kempf, S., Roberts, J. L., van Ommen, T., Forsberg, R., Siegert, M., Palmer, S. J., and Dowdeswell, J. A. (2013). IceBridge Riegl Laser Altimeter L2 geolocated surface elevation triplets. 50, 52

Cook, A. J., Murray, T., Luckman, A., Vaughan, D. G., and Barrand, N. E. (2012). A new 100m Digital Elevation Model of the Antarctic Peninsula derived from ASTER Global DEM: methods and accuracy assessment. *Earth System Science Data*, 4:129–142. 44

Cornford, S. L., Martin, D. F., Payne, A. J., Ng, E. G., Le Brocq, A. M., Gladstone, R. M., Edwards, T. L., Shannon, S. R., Agosta, C., van den Broeke, M. R., Hellmer, H. H., Krinner, G., Ligtenberg, S. R. M., Timmermann, R., and Vaughan, D. G. (2015). Century-scale simulations of the response of the West Antarctic Ice Sheet to a warming climate. *The Cryosphere*, 9(4):1579–1600. 44

Davis, C. H. (1997). A robust threshold retracking algorithm for measuring ice-sheet surface elevation change from satellite radar altimeters. *IEEE Transactions on Geoscience and Remote Sensing*, 35(4):974–979. 46

Davis, C. H. and Ferguson, A. C. (2004). Elevation change of the Antarctic ice sheet, 1995-2000, from ERS-2 satellite radar altimetry. *IEEE Transactions on Geoscience and Remote Sensing*, 42(11):2437–2445. 56

DiMarzio, J., Brenner, A., Schutz, R., Shuman, C. A., and Zwally, H. J. (2007). GLAS/ICESat 500m laser altimetry Digital Elevation Model of Antarctica. 44

ESA (2012). CryoSat-2 Product Handbook, ESRIN-ESA and Mullard Space Science Laboratory University College London, available at: http://emits.sso.esa.int/emits-doc/ESRIN/7158/CryoSat-PHB-17apr2012.pdf (last access: October 2017). 46

Fei, L. I., Feng, X., Sheng-Kai, Z., Dong-Chen, E., Xiao, C., Wei-Feng, H. A. O., Le-Xian, Y., and Yao-Wen, Z. U. O. (2017). DEM development and precision analysis for Antarctic Ice Sheet using CryoSat-2 altimetry data. *Chinese Journal of Geophysics*, 60(3):231–243. 44, 63

Flament, T. and Rémy, F. (2012). Dynamic thinning of Antarctic glaciers from along-track repeat radar altimetry. *Journal of Glaciology*, 58(211):830–840. 46

Fretwell, P., Pritchard, H. D., Vaughan, D. G., Bamber, J. L., Barrand, N. E., Bell, R., Bianchi, C., Bingham, R. G., Blankenship, D. D., Casassa, G., Catania, G., Callens, D., Conway, H., Cook, A. J., Corr, H. F. J., Damaske, D., Damm, V., Ferraccioli, F., Forsberg, R., Fujita, S., Gim, Y., Gogineni, P., Griggs, J. A., Hindmarsh, R. C. A., Holmlund, P., Holt, J. W., Jacobel, R. W., Jenkins, A., Jokat, W., Jordan, T., King, E. C., Kohler, J., Krabill, W., Riger-Kusk, M., Langley, K. A., Leitchenkov, G., Leuschen, C., Luyendyk, B. P., Matsuoka, K., Mouginot, J., Nitsche, F. O., Nogi, Y., Nost, O. A., Popov, S. V., Rignot, E., Rippin, D. M., Rivera, A., Roberts, J., Ross, N., Siegert, M. J., Smith, A. M., Steinhage, D., Studinger, M., Sun, B., Tinto, B. K., Welch, B. C., Wilson, D., Young, D. A., Xiangbin, C., and Zirizzotti, A. (2013). Bedmap2: improved ice bed, surface and thickness datasets for Antarctica. *The Cryosphere*, 7(1):375–393. 44, 63

Griggs, J. A. and Bamber, J. L. (2009). A new 1 km Digital Elevation Model of the Antarctic derived from combined radar and laser data – Part 2: Validation and error estimates. *The Cryosphere*, 3(1):113–123. 44

Helm, V., Humbert, A., and Miller, H. (2014). Elevation and elevation change of Greenland and Antarctica derived from CryoSat-2. *The Cryosphere*, 8(4):1539–1559. 44, 49, 63

Isaaks, E. H. and Srivastava, R. M. (1989). *An Introduction to Applied Geostatistics*. Oxford University Press, New York, USA. 49

Khvorostovsky, K. S. (2012). Merging and analysis of elevation time series over Greenland Ice Sheet from satellite radar altimetry. *IEEE Transactions on Geoscience and Remote Sensing*, 50(1):23–36. 56

Kitanitis, P. K. (1997). *Introduction to Geostatistics: Applications in Hydrogeology*. Cambridge University Press, Cambridge, UK. 49

Koenig, L., Martin, S., Studinger, M., and Sonntag, J. (2010). Polar airborne observations fill gap in satellite data. *Eos, Transactions American Geophysical Union*, 91(38):333–334. 50

Korona, J., Berthier, E., Bernard, M., Rémy, F., and Thouvenot, E. (2009). Spirit. spot 5 stereoscopic survey of polar ice: Reference images and topographies during the fourth international polar year (2007–2009). *ISPRS Journal of Photogrammetry and Remote Sensing*, 64(2):204–212. 44

Krabill, W., Hanna, E., Huybrechts, P., Abdalati, W., Cappelen, J., Csatho, B., Frederick, E., Manizade, S., Martin, C., Sonntag, J., Swift, R., Thomas, R., and Yungel, J. (2004). Greenland Ice Sheet: Increased coastal thinning. *Geophysical Research Letters*, 31(24). 50

Krabill, W. B. (2016). IceBridge ATM L2 Icessn elevation, slope and roughness version 2, National Snow and Ice Data Center, Boulder, Colorado, USA, available at: https://nsidc.org/icebridge/portal/ (last access January 2017). 50

Kwok, R., Cunningham, G. F., Manizade, S. S., and Krabill, W. B. (2012). Arctic sea ice freeboard from IceBridge acquisitions in 2009: Estimates and comparisons with ICESat. *Journal of Geophysical Research: Oceans*, 117(C2). 52

Levinsen, J. F., Howat, I. M., and Tscherning, C. C. (2013). Improving maps of ice-sheet surface elevation change using combined laser altimeter and stereoscopic elevation model data. *Journal of Glaciology*, 59(215):524–532. 50

Liu, H., Jezek, K. C., Li, B., and Zhao, Z. (2001). Radarsat Antarctic Mapping Project Digitial Elevation Model version 2. 44, 46

McMillan, M., Shepherd, A., Sundal, A., Briggs, K., Muir, A., Ridout, A., Hogg, A., and Wingham, D. (2014). Increased ice losses from Antarctica detected by CryoSat-2. *Geophysical Research Letters*, 41(11):3899–3905. 46, 49, 55

Mouginot, J., Scheuchl, B., and Rignot, E. (2012). Mapping of ice motion in Antarctica using synthetic-aperture radar data. *Remote Sensing*, 4(9):2753–2767. 44

Rignot, E., Mouginot, J., and Scheuchl, B. (2011a). Ice flow of the Antarctic Ice Sheet. *Science*, 333(6048):1427. 44

Rignot, E., Velicogna, I., van den Broeke, M. R., Monaghan, A., and Lenaerts, J. T. M. (2011b). Acceleration of the contribution of the Greenland and Antarctic ice sheets to sea level rise. *Geophysical Research Letters*, 38(5). 44

Ritz, C., Edwards, T. L., Durand, G., Payne, A. J., Peyaud, V., and Hindmarsh, R. C. (2015). Potential sea-level rise from Antarctic ice-sheet instability constrained by observations. *Nature*, 528(7580):115–8. 44

Shepherd, A., Ivins, E. R., A, G., Barletta, V. R., Bentley, M. J., Bettadpur, S., Briggs, K. H., Bromwich, D. H., Forsberg, R., Galin, N., Horwath, M., Jacobs, S., Joughin, I., King, M. A., Lenaerts, J. T. M., Li, J., Ligtenberg, S. R. M., Luckman, A., Luthcke, S. B., McMillan, M., Meister, R., Milne, G., Mouginot, J., Muir, A., Nicolas, J. P., Paden, J., Payne, A. J., Pritchard, H., Rignot, E., Rott, H., Sørensen, L. S., Scambos, T. A., Scheuchl, B., Schrama, E. J. O., Smith, B., Sundal, A. V., van Angelen, J. H., van de Berg, W. J., van den Broeke, M. R., Vaughan, D. G., Velicogna, I., Wahr, J., Whitehouse, P. L., Wingham, D. J., Yi, D., Young, D., and Zwally, H. J. (2012). A reconciled estimate of ice-sheet mass balance. *Science*, 338(6111):1183. 44

Sutterley, T. C., Velicogna, I., Rignot, E., Mouginot, J., Flament, T., van den Broeke, M. R., van Wessem, J. M., and Reijmer, C. H. (2014). Mass loss of the Amundsen Sea Embayment of West Antarctica from four independent techniques. *Geophysical Research Letters*, 41(23):8421–8428. 44

Wingham, D. J., Francis, C. R., Baker, S., Bouzinac, C., Brockley, D., Cullen, R., de Chateau-Thierry, P., Laxon, S. W., Mallow, U., Mavrocordatos, C., Phalippou, L., Ratier, G., Rey, L., Rostan, F., Viau, P., and Wallis, D. W. (2006). CryoSat: A mission to determine the fluctuations in Earth's land and marine ice fields. *Advances in Space Research*, 37(4):841–871. 44, 45, 46

Wingham, D. J., Phalippou, L., Mavrocordatos, C., and Wallis, D. (2004). The mean echo and echo cross product from a beamforming interferometric altimeter and their application to elevation measurement. *IEEE Transactions on Geoscience and Remote Sensing*, 42(10):2305–2323. 45

Wingham, D. J., Rapley, C. G., and Griffiths, H. (1986). New techniques in satellite altimeter tracking systems. In *18th IGARSS Symposium*. 46

Wingham, D. J., Ridout, A. J., Scharroo, R., Arthern, R. J., and Shum, C. K. (1998). Antarctic elevation change from 1992 to 1996. *Science*, 282(5388):456–458. 56

Wingham, D. J. and Wallis, D. W. (2010). The rough surface impulse response of a pulse-limited altimeter with an elliptical antenna pattern. *IEEE Antennas and Wireless Propagation Letters*, 9:232–235. 45

Young, D. A., Kempf, S. D., Blankenship, D. D., Holt, J. W., and Morse, D. L. (2008). New airborne laser altimetry over the thwaites glacier catchment, west antarctica. *Geochemistry, Geophysics, Geosystems*, 9(6). 52

Zwally, H. J., Giovinetto, M. B., Beckley, M. A., and Saba, J. J. L. (2012). Antarctic and Greenland drainage systems. xii, xiv, 47, 55

Chapter 3

Compensating changes in the penetration depth of pulse limited radar altimetry over the Greenland Ice Sheet

Authors: **Thomas Slater, Andrew Shepherd, Malcolm McMillan, Thomas W. K. Armitage, Inès Otosaka, Robert J. Arthern**

Abstract

Changes in firn properties affect the shape of pulse-limited radar altimeter echoes acquired over the polar ice sheets. We apply a waveform deconvolution model to CryoSat-2 low-resolution mode echoes to determine the depth-distribution of radar backscattering across the Greenland Ice Sheet. The deconvolution allows us to calculate the relative contributions of surface and volume scattering, and the effective penetration depth of the radar echoes into the snowpack. The most prominent signal is that associated with the extreme surface melting of summer 2012, which resulted in a shift of the dominant radar scattering horizon towards the snow surface in the accumulation zone. At locations above 2000 m, the average penetration depth in July 2012 (prior to the melt event) was 3.79 ± 1.12 m. Following the melt event, there was an abrupt reduction in the average penetration depth across the same region to 1.45 ± 0.94 m.

The average penetration depth then gradually increased to 3.28 ± 1.13 m by the end of 2017, as fresh snow accumulated on the ice sheet surface. Although the variation in penetration is evident in surface height estimates derived from the CryoSat-2 echoes, the magnitude of the effect is reduced by waveform retracking. Using airborne laser altimeter data recorded over the same time period, we show that the penetration variation can be compensated effectively by incorporating the deconvolution penetration depth into the surface height retrieval.

3.1 Introduction

Measurements of surface elevation change from satellite radar altimeters have transformed our understanding of the Greenland Ice Sheet, resolving detailed patterns of thinning across dynamic marine-terminating glaciers and in the ice sheet margins, where surface melting occurs each summer (Helm et al., 2014; Johannessen et al., 2005; McMillan et al., 2016; Nilsson et al., 2016; Sandberg Sørensen et al., 2018; Shepherd et al., 2012; Simonsen and Sørensen, 2017). Satellite radar altimeters transmit a microwave pulse at nadir, and record backscattered power as a function of time delay (the echo). Over ice, the shape of altimeter echoes is complicated by (1) ice sheet topography (surface scattering), and (2) the Ku band radar penetrating several metres beyond the snow surface (volume scattering) (Armitage et al., 2014; Arthern et al., 2001; Davis and Moore, 1993; Ridley and Partington, 1988; Wingham et al., 2006). The depth of radar penetration is dependent on the physical properties of the ice sheet surface and near-surface snowpack (e.g. grain size, density, liquid water content) (Matzler, 1996), which exhibit both spatial and seasonal variability (Davis and Zwally, 1993). The precise height of the ice sheet surface is estimated from altimeter echoes through retracking algorithms, designed to be less sensitive to fluctuations in penetration by focussing on the surface scattering contribution to the echo leading edge (Davis, 1997; Helm et al., 2014).

In July 2012 an unprecedented proportion (98.6 %) of the Greenland Ice Sheet experienced surface melting as increased transport of warm air from the south created anomalously high temperatures (Fettweis et al., 2013; Nghiem et al., 2012). This event was clearly visible in passive and active microwave imagery (Casey et al., 2017; Nghiem

et al., 2012; Tedesco et al., 2013), extending inland to high altitude regions (approximately > 2800 m.a.s.l.) which had not seen melting during the satellite era (Mote, 2007). Meltwater percolated and re-froze in a layer near to the snow surface (Nghiem et al., 2012), altering the physical properties of the firn layer within which radar altimeter echoes are scattered. Across the ice sheet interior, an apparent 89 ± 49 cm increase in surface elevation was recorded in uncorrected CryoSat-2 satellite radar altimeter elevation data after the melt event (Nilsson et al., 2015). A range of approaches have been employed to mitigate this effect, including applying (1) threshold retrackers (Helm et al., 2014; Nilsson et al., 2016), which are less sensitive to variations in volume scattering, (2) a step offset to the affected elevation time series (McMillan et al., 2016) and (3) a correction to retracked heights based upon correlated fluctuations between elevation change and several echo parameters including the leading edge width, trailing edge slope and backscatter coefficient (Sandberg Sørensen et al., 2018; Simonsen and Sørensen, 2017). Here, we employ a waveform deconvolution model to CryoSat-2 data to retrieve the depth-distribution of radar scattering across the interior of the Greenland Ice Sheet, and to compensate surface height retrievals for the effects of temporal variations in firn properties.

3.2 Data and methods

3.2.1 Penetration depth

CryoSat-2, launched in 2010, was designed to overcome challenges faced by previous satellite radar altimeters over Earth's polar regions. Equipped with a novel synthetic aperture radar altimeter and interferometer providing high spatial resolution measurements in areas of steep terrain, CryoSat-2 observes to latitudes of ± 88 °, with a long-period, drifting orbit (369-day repeat period with a 30-day subcycle) which affords a high density of orbit cross-overs at the poles (Wingham et al., 2006). Across the interior of the Greenland Ice Sheet, CryoSat-2 acquires measurements in low-resolution mode (LRM), where it operates as a traditional pulse-limited altimeter illuminating a ground footprint of 1.5 km diameter (Wingham and Wallis, 2010). Previous studies have investigated the effects of variable surface and volume scattering on altimeter echoes acquired over ice sheets through fitting a theoretical model to both averaged (Davis and Moore, 1993; Partington et al., 1989) and individual altimeter echoes (Davis, 1993). Here,

we investigate spatial and temporal variations in the degree of radar penetration into the Greenland Ice Sheet, using CryoSat-2 Level 1b baseline-C data acquired between January 2011 and December 2017 and a numerical deconvolution technique (Arthern et al., 2001; Wingham et al., 2004) designed to separate the effects of scattering from the surface and from greater depth within the snowpack. This model assumes that the effects of large scale surface slope and footprint-scale topographic undulations upon the waveform shape are negligible, and is therefore only appropriate in areas of flat terrain.

First, we describe CryoSat-2 echoes as a convolution of three functions (Brown, 1977; Ridley and Partington, 1988):

$$P_R(t) = P_T(t) * P_{FS}(t) * P_D(t) \tag{3.1}$$

where $P_R(t)$ is the pulse received at the antenna as a function of time, t, $P_T(t)$ is the transmitted pulse shape, $P_{FS}(t)$ is the normalised flat surface impulse response and $P_D(t)$ is the distribution of backscattered power with depth and surface roughness height. $P_{FS}(t)$ represents the echo that would be recovered from an ideal flat surface if a delta function were transmitted, if no penetration occurred and if the flat surface had a backscatter coefficient equal to unity. In this way, $P_D(t)$ contains both the surface and volume backscattering cross sections. Over ice sheets, $P_D(t)$ contains all scattering contributions from both the ice sheet surface and due to penetration of the radar pulse into the snowpack.

The Fourier transform of a convolution of time-dependent functions is equal to the product of their spectra in the frequency domain, ω. Utilising this property, Equation (3.1) can be re-written as:

$$P_R(t) = P_T(t) * P_{FS}(t) * P_D(t) \leftrightarrow P_T(\omega)P_{FS}(\omega)P_D(\omega) = P_R(\omega) \tag{3.2}$$

where $\leftrightarrow$ denotes the Fourier transform operation. By performing the Fourier transform, we are able to isolate the distribution of scattering with depth and surface roughness height, $P_D(t)$, by removing convolved scattering contributions outside the point of closest approach within a given radar footprint in the frequency domain. Before deconvolving, we downsample the CryoSat-2 echoes from 20 Hz to 1 Hz in order to reduce the effects of speckle noise, and because individual echoes are more distorted by

topography within the radar footprint than their average. Rearranging and rewriting Equation (3.2) gives:

$$P_D(t) \leftrightarrow \frac{P_R(\omega)}{P_T(\omega)\overline{P_{FS}(\omega)}}\Pi(\omega) \tag{3.3}$$

where $P_T(\omega)\overline{P_{FS}(\omega)}$ is the product of the transmitted and the mean flat surface impulse response spectra, and $\Pi(\omega)$ is a Gaussian low-pass smoothing filter with a standard deviation of 40 frequency bins. As an empirical approximation for $P_T(\omega)\overline{P_{FS}(\omega)}$, we assume that the average impulse response of an a flat ice sheet is equal to that of a uniformly rough ocean surface (i.e. $P_D(t)$ approaches that of a Dirac delta function, $\delta(t)$). To estimate this response, we use the mean of a set of CryoSat-2 LRM echoes acquired over a region of the Mediterranean Sea where the significant wave height is less than 0.1 m and the impact of surface roughness on the waveform is minimised.

In order to obtain information about the scattering properties of the illuminated snowpack, we fit an analytical function (Arthern et al., 2001) to the resulting deconvolutions (Equation 3.2.1), $P_D(t)$ through a non-linear least-squares regression (using the Levenberg-Marquardt algorithm, (Marquardt, 1963)) such that:

$$P_D(t;\sigma^0_{surf},\sigma^0_{vol},k_e,\gamma,\bar{t}) = \frac{\sigma^0_{surf}}{\gamma\sqrt{\pi}}\exp\left(-\frac{(t-\bar{t})^2}{\gamma^2}\right) + \frac{\sigma^0_{vol}c_{ice}k_e}{2}$$
$$\cdot\exp\left(\frac{\gamma^2c_{ice}^2k_e^2}{4} - c_{ice}k_e(t-\bar{t})\right)\cdot\left[1+\mathrm{erf}\left(\frac{(t-\bar{t})}{\gamma} - \frac{\gamma c_{ice}k_e}{2}\right)\right] \tag{3.4}$$

where σ^0_{surf} is the surface backscatter cross section, σ^0_{vol} is the depth-integrated volume backscatter, k_e is the extinction coefficient, γ is the leading edge width, and $\bar{t}$ is the leading edge time delay (e.g. Figure 3.1). The leading edge width and delay time refer to those that apply after the ocean echo has been removed, and following the application of the smoothing filter. The influence of the significant wave height and smoothing filter on the modelled leading edge width are small relative to the effects of surface roughness and the depth of radar penetration. We use $c_{ice} = 2.2 \times 10^8$ m/s, which is a common value for the speed of light in densities typical of the upper snowpack (Matzler, 1996). In Equation (3.4), echoes are modelled as the sum of contributions due to scattering from the snow surface (a Gaussian peak) and from the subsurface volume (an exponentially decaying tail). σ^0_{surf} and σ^0_{vol}, the integrals of the surface and volume scattering terms, describe their relative strength, while k_e denotes the rate

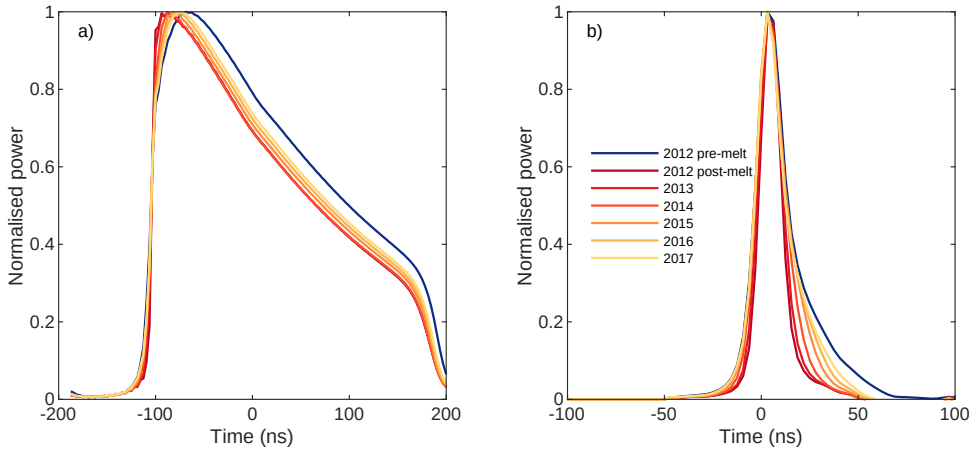

Figure 3.1: Average of (a) CryoSat-2 low-resolution mode echoes and (b) their respective deconvolutions acquired in areas exceeding 2000 m in elevation before (January-June) and after (August-December) the melt event of July 2012, and during the subsequent years (2013 to 2017). Plotted waveforms and deconvolutions are normalized to peak power of unity.

(in units of m^{-1}) that the radar signal is attenuated as it travels into the snowpack. We note that the units of σ^0_{surf} and σ^0_{vol} are dependent upon the CryoSat-2 ice and ocean waveforms being normalised during the deconvolution procedure, in order to account for the differing strength of their respective returns. Because of this, we recover backscatter coefficients relative to a reference backscatter (that of the ocean echo used in the deconvolution). Together, these three parameters describe the scattering behaviour of the snowpack and allow estimation of the radar penetration depth, defined as the inverse of the extinction coefficient (Arthern et al., 2001).

We estimate σ^0_{surf}, σ^0_{vol}, and k_e from deconvolved CryoSat-2 L1b LRM echoes acquired across the interior of the Greenland Ice Sheet between January 2011 and December 2017. We limit our analyses to the region of the ice sheet interior above the 2000 m contour, in order to provide a continuous, $\sim$ 710,000 km^2 area in which the ice sheet

Figure 3.2: Pre- and post-melt event and yearly averages of (a) surface backscatter coefficient, (b) volume backscatter coefficient and (c) penetration depth during the period 2012-2017. In each plot, the black line represents the boundary between LRM and SARIn mode acquisitions, and grey lines represent elevation contours of 2000, 2500 and 3000 m. Shading represents extent of the ice sheet (white) and surrounding land (grey). Also shown (purple, (c) 2012 post-melt) is the location of the North Greenland Eemian Ice Drilling Project site and surrounding area used for comparison to Nilsson et al. (Nilsson et al., 2015).

surface slopes are low (approximately 0.1 ° on average), which covers the entirety of the dry snow zone where the scattering horizon was reset in 2012, and which corresponds to 92 % of the area sampled in LRM. Solutions where the scattering model fails to converge after 20 iterations (through minimising the chi-squared error of the fit), and that yield unrealistic penetration depths of more than 10 m are excluded. To investigate spatial and temporal variations, we compute the mean values of each of the three scattering parameters within 25 x 25 km grid cells and within discrete time intervals (e.g. Figure 3.2). To track temporal changes in penetration depth we then average the data in monthly time intervals (e.g. Figure 3.3a).

3.2.2 Elevation change

A variety of retracking routines have been applied to satellite altimeter waveforms to improve the accuracy, precision, and stability of ice sheet surface height retrieval (Davis, 1997; Helm et al., 2014; Wingham et al., 1986). To assess the impact of the Greenland Ice Sheet surface properties, we compare temporal variations in the radar penetration depth before and after significant melting events to changing surface heights estimated using conventional waveform retracking algorithms. To compute the latter, we use measurements of ice sheet surface elevation determined using two waveform retrackers available in the Level 2i baseline-C product: (1) a model based algorithm, CFI (ESA, 2012), historically available in the baseline-B product and known to be sensitive to fluctuations in the scattering horizon (Nilsson et al., 2016), and (2) a threshold offset center of gravity (TCOG) retracking algorithm, which selects a threshold power of 30 % of the OCOG amplitude. With these algorithms we analyse the effects of variable radar penetration on the two main classes of retracker most commonly used in the literature: physically-based (CFI), and empirically-based (TCOG). While other empirical threshold retrackers have been used in previous studies, and provide less weight to later delay times as they focus only on the leading edge of the waveform (e.g. (Helm et al., 2014)), we contrast the echo deconvolution to those included in the ESA Level 2i product. Time-series of ice sheet surface elevation change are then generated from these measurements using a model fit (Flament and Rémy, 2012; McMillan et al., 2016) to separate spatial and temporal fluctuations within 5 x 5 km grid cells:

$$z(x,t,y,h) = \bar{z} + a_0 x + a_1 y + a_2 x^2 + a_3 y^2 + a_4 xy + a_5 h + a_6 t \tag{3.5}$$

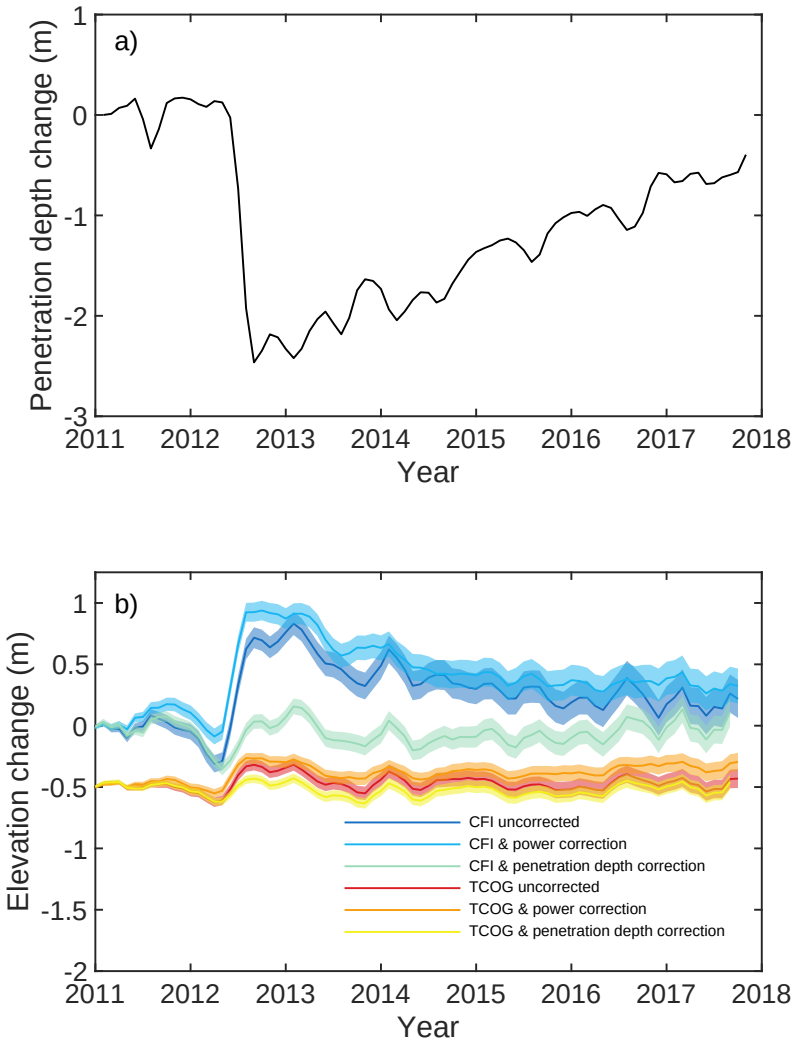

Figure 3.3: Monthly evolution of the change in (a) penetration depth and (b) elevation in the interior of the Greenland Ice Sheet (> 2000 m.a.s.l.), 2011-2017. Time series of elevation change are calculated using the CFI (blue) and TCOG (red) retracking algorithms, both before and after applying corrections for correlated fluctuations in backscattered power and penetration depth. For visualisation purposes, an offset of 50 cm has been applied to the TCOG time series.

where we model the elevation (z) as a function of the local surface terrain (x, y), satellite heading (h, which equals 0 or 1 whether measurement was acquired on an ascending or descending pass, respectively) and time (t). We solve for the individual model coefficients using an iterative least-squares fit to minimise the impact of outliers, and discard any unrealistic estimates from poorly constrained solutions based on a set of statistical thresholds which include: a minimum of 40 data points, a time series length of at least 2 years, a maximum root mean squared difference of elevation residuals from the model of 12 m, a maximum elevation rate magnitude of 10 m/yr, and a maximum surface slope of 5 °. The resulting time-series are then averaged within 25 x 25 km grid cells and across monthly intervals to allow comparison with the estimates of penetration depth obtained from the deconvolution procedure at the same location (e.g. Figure 3.3b). A resolution of 25 km has been selected as a balance between the spatial resolution and the number of measurements averaged to reduce noise in our monthly penetration depth time series. Within any given time series, we quantify the uncertainty at each epoch by computing the regional average of the standard error of height change measurements within all contributing pixels. We assume this component is temporally uncorrelated, therefore at any given epoch we sum all preceding uncertainties in quadrature. To obtain the error on the overall elevation change, we combine this uncertainty with the standard error of the rate of surface elevation change in quadrature, in order to account for systematic errors which may affect the trend.

Time-series of ice sheet elevation change computed using conventionally retracked waveforms have exhibited seasonal cycles (Davis and Ferguson, 2004; Khvorostovsky, 2012; Wingham et al., 1998) and episodic shifts (Nilsson et al., 2015) that track changes in the echo properties, which have been interpreted as owing to changes in the surface scattering (McMillan et al., 2016; Nilsson et al., 2016; Simonsen and Sørensen, 2017). To account for these, we first apply a correction based upon correlations between changes in elevation and backscattered power (Davis and Ferguson, 2004; McMillan et al., 2016) (e.g. Figure 3.3b). As an alternative approach, we also explore the use of the penetration depth determined from our deconvolution method as the basis for a volume scattering correction (e.g. Figure 3.3b). We do not, however, apply the penetration depth as an explicit correction to the L2 data, because the conventional waveform

retracking routines have been designed in part to minimize the effects of volume scattering, and because the scattering correction may not be entirely due to fluctuations in penetration. Instead, we develop a surface scattering correction based on the ratio between changes in penetration depth and elevation, and we then apply the correction to retracked heights at each point in our elevation time series such that:

$$dH_{corrected} = dH - \frac{dH}{dk_e^{-1}} \cdot dk_e^{-1} \tag{3.6}$$

where dH is the elevation change at each epoch, k_e^{-1} is the radar penetration depth, and $\frac{dH}{dk_e^{-1}}$ is the correlation gradient between changes in elevation and penetration depth.

To complement the LRM data, which survey the ice sheet interior, we also compute time-series of surface elevation change from CryoSat-2 measurements acquired in synthetic aperture radar interferometry (SARIn) mode around the ice sheet margin. In this mode, CryoSat-2 uses two receive antennae to determine the location of the point of closest approach in the across-track plane through interferometry, with an along-track ground resolution of approximately 400 m (Wingham et al., 2004). SARIn elevation estimates are determined using the ESA Level 2 SARIn retracker, which fits an analytical model to each SAR waveform (ESA, 2012; Wingham et al., 2006). We then compute elevation trends using the same model fit (Flament and Rémy, 2012; McMillan et al., 2016) applied to measurements collected within 5 km grid cells, only we preserve the trends at this resolution to better describe the complex topography of the ice sheet margins. We do not attempt to deconvolve the SARIn echoes as the terrain is not flat. Although this prevents us from estimating the penetration depth, we instead adjust the time series of elevation change to account for temporal variations in the degree of radar penetration using a correction based upon correlated fluctuations in elevation and backscattered power (Davis and Ferguson, 2004; McMillan et al., 2016).

Elevation trends in empty grid cells at elevations below 2000 m.a.s.l. are filled using an empirical model based upon latitude, elevation and velocity change, all of which affect surface elevation change through temperature-related processes or ice flow (McMillan et al., 2016). We model the observed elevation trend as function of latitude (l), elevation

(z) and change in velocity (Δv):

$$\frac{dz}{dt} = al + bz + c\Delta v + d \tag{3.7}$$

which we then use to estimate trends in unobserved grid cells. The change in velocity was computed by differencing velocities recorded in 2008-2009 and 2000-2001 (Joughin et al., 2015, 2010). Where no velocity data is available, we use a model based on latitude and elevation only. Based upon the root mean squared difference of the residuals to the model fit, we estimate an average uncertainty in unobserved grid cells of 0.4 m/yr.

3.3 Results and discussion

To examine the effect of the 2012 melt event on elevation trends derived over varying timescales, we process data over two time periods: (1) 2011-2014, similar to the temporal extent of previous studies affected by melting (McMillan et al., 2016; Nilsson et al., 2016; Simonsen and Sørensen, 2017), and (2) 2011-2017, which we expect to be less influenced by the 2012 melt event, given the longer duration of the record. We compare rates of elevation change determined from the LRM and SARIn data to estimates derived from Operation IceBridge repeat airborne laser altimetry (Studinger, 2014). For our shorter 2011-2014 period, we remove any IceBridge elevation rates which do not span the melt event, any which are outside the dry snow zone, and any for which the repeat period is less than 2 years. In total, this accounts for 34 % (821,000) of all IceBridge measurements acquired between 2011 and 2014. For the 2011-2017 period, we utilise all available data to maximize the number of available comparisons. For both time periods, we bin the IceBridge measurements at a resolution of 25 km and 5 km within the LRM and SARIn areas, respectively, and remove any grid cells sampled by less than 10 IceBridge measurements or where the standard deviation of laser altimetry elevation rates is greater than 2 m/yr. These filtering steps removed 12 % and 15 % of grid cells between 2011 and 2014, and 5 % and 15 % of grid cells between 2011 and 2017 in the LRM and SARIn zones, respectively. Overall, we compare rates of elevation change in 135 and 3375 grid cells between 2011 and 2014, and 585 and 8788 grid cells between 2011 and 2017 in the LRM and SARIn zones, respectively.

3.3.1 Penetration depth

Deconvolutions of CryoSat-2 LRM echoes acquired before and after the 2012 melt event (Figure 3.1) demonstrate a clear shift from a situation dominated by volume scattering (power within the decaying tail, delay times greater than zero), to scattering from near to the snow surface (specular peak, increased backscatter at delay times near zero). Variations in the shape of the original CryoSat-2 LRM echoes (Figure 3.1) are also visible, but disentangling the effects of surface contributions beyond the point of closest approach (POCA) and radar penetration is more difficult, as both redistribute backscattered power to later delay times in the leading edge (Arthern et al., 2001). By removing scattering contributions outside the POCA within a given radar footprint through the deconvolution procedure, the distribution of scattering with depth and surface roughness can be more clearly observed. In the years 2013-2017, the deconvolved echoes show a continuous increase in volume backscatter, returning to the shape observed before the melt event (Figure 3.1b).

Across the ice sheet interior as a whole, there is a two-fold increase in the proportion of backscattered power returning from the ice sheet surface (σ^0_{surf}) after the melt event, on average (Figure 3.2) . In regions above 2000 m in altitude, we estimate that the radar penetration depth decreased by approximately 2.34 $\pm$ 1.41 m on average, between the months before (January-June) and after (August-December) the formation of the new scattering horizon in July 2012 (Figure 3.2) (penetration depth uncertainties are defined to be one standard deviation of the spatial variability). In higher altitude areas above 2800 m.a.s.l. which experienced melting for the first time in the satellite era, we estimate an even greater reduction in Ku band radar penetration depth of 3.21 $\pm$ 1.16 m. At lower elevation regions towards the south of the LRM zone ($<$ 2500 m.a.s.l.), there is little change in the scattering horizon following the melt event (Figure 3.2). Using definitions of ice melt zones used in McMillan et al. (McMillan et al., 2016) and Leeson et al. (Leeson et al., 2018), we find that this area is within the percolation zone which typically experiences melt each summer (Tedesco et al., 2013). In the percolation zone, there is no clear evidence of a coherent change in penetration depth following the 2012 melt event, with an estimated change of 0.25 $\pm$ 0.61 m. Excluding the percolation zone, the decrease in penetration depth in the dry snow zone following

the 2012 summer melt event is 2.64 ± 1.16 m on average.

The effect of the 2012 melt event on CryoSat-2 elevation estimates has been previously assessed over Greenland (Nilsson et al., 2015); within a 90 000 km^2 area around the North Greenland Eemian Ice Drilling Project (NEEM) camp (Figure 3.2), an increase in surface elevation of 1.24 ± 0.51 m was recorded across the period of the melt event. Our deconvolution of CryoSat-2 waveforms acquired in the same area show a decrease in radar penetration depth of 1.74 ± 0.76 m between the 30-day periods before and after 11 July 2012, the date of the maximum single-day melt extent (Tedesco et al., 2013). Although the change in surface elevation and penetration depth are similar, they are not equivalent as a waveform retracker is applied to the elevation measurement to reduce the impact of volume scattering, and so a lower elevation change is to be expected.

Following the formation of the new radar scattering horizon after the 2012 melt event, backscattered power increasingly shifts to the ice sheet volume year-on-year during subsequent years (Figure 3.1, Figure 3.2). An extreme melt event can be defined as one which produces more than 1 mm w.e./day of melting (Franco et al., 2013). Between 1995 and 2015, the only melt event of such magnitude to affect the Greenland Ice Sheet interior was July 2012 (Leeson et al., 2018). Snowfall has since accumulated on the ice sheet surface, forming an increasingly thick new firn layer above the 2012 horizon. This change in firn structure is consistent with the evolution of backscattered power, which has returned to its pre-melt event state over the same period. Continued increases in the proportion of volume scattering since 2015 suggest that no further melting significant enough to disrupt the Ku band radar scattering horizon in the ice sheet interior has occurred within our study area. By comparing our yearly estimates of radar penetration depth to its pre-melt average (Figure 3.2) we estimate that, by the end of 2017, the scattering horizon has lowered to a depth of 3.28 ± 1.13 m on average, to within approximately 0.5 m of that recorded before July 2012 (3.79 ± 1.12 m).

At the regional scale, the step-like reduction in the average penetration depth across the interior of the ice sheet as a result of the 2012 melt event is clearly visible (Figure 3.3). By fitting a linear trend to the penetration depth time series between 2013 and 2017, we find that since the melt event the radar scattering horizon has lowered by 0.4

m/yr, on average. Assuming it continues at this rate, backscattered power from the ice sheet interior will return to near its pre-melt distribution by 2020, provided that there are no further extreme melt events of the scale recorded in 2012. We note that the rate at which the scattering horizon lowers is not equivalent to the downward velocity of the ice lens formed in 2012, and is dependent on the firn compaction rate in addition to the surface mass balance.

3.3.2 Elevation change

To further explore the relationship between fluctuations in penetration depth and elevation, we also examined estimates of ice sheet elevation change derived from ranges corrected using a variety of waveform retrackers (e.g. Figure 3.3b). When the CFI retracker is used (Figure 3.3), we observe a step-like increase in elevation of 91 $\pm$ 17 cm over the summer of 2012, consistent with previous findings (Nilsson et al., 2015). Although less sensitive to changes in volume scattering, we also observe a step increase of 21 $\pm$ 9 cm when a TCOG retracker is applied. A step of similar magnitude is also apparent in the elevation time series corrected for fluctuations in backscattered power, which does capture the changes in volume scatter coincident with the melt event. Although both retrackers lead to elevation changes that are small by comparison to the change in penetration depth (Figure 3.3a), a step is still present. However, when the penetration depth is included as an additional factor in the elevation change retrieval (Equation 3.6), the step is further reduced (Figure 3.3b).

The degree of correlation between changes in penetration depth and surface elevation is dependent upon a number of factors, including the waveform retracker, the time period considered, and the ice sheet location. For grid cells within the dry snow zone changes in penetration depth account for, on average, 14 % and 1 % of the observed variance in elevations derived from the CFI and TCOG retrackers over the entire time period, respectively. In addition, a change in radar penetration depth of 1 m corresponds to a change of 0.21 m and 0.06 m in the retracked height derived from the CFI and TCOG algorithms on average, respectively. Overall there is higher spatial variability in the correlation between changes in height and penetration depth for the CFI retracker than for the TCOG retracker (standard deviation of the Pearson correlation coefficient, R, of 0.18 and 0.10, respectively). In both cases, we find significantly higher correlation

within the dry snow zone (reaching a maximum of $R = -0.70$ for CFI and $R = -0.40$ for TCOG). Within the percolation zone, we find little association between changes in penetration depth and height for both retrackers ($R = -0.05$ for CFI and $R = -0.01$ for TCOG, on average).

The pattern of regional elevation change calculated over both time periods broadly agrees with the pattern derived from the sparse repeat airborne laser altimetry (Figure 3.4). Previously identified signals of ice thinning at individual glaciers and along the western margin (e.g. (Helm et al., 2014; McMillan et al., 2016; Nilsson et al., 2016; Simonsen and Sørensen, 2017)) are well resolved in both datasets. We find the highest rates of thinning at key marine terminating glaciers known to be in a state of dynamical imbalance (e.g. Jakobshavn Isbræ, Kangerlussuaq and Upernavik Isstrøm). Our longer 7-year survey period (2011-2017) reveals that these high rates of thinning (in excess of 2 m/yr) have persisted at these sites throughout the decade, in agreement with the laser altimetry. We also resolve losses resulting from seasonal melt in the ablation zone close to the ice sheet margin. We note that differences between the radar and airborne laser altimetry may arise due to the way in which we have constructed the reference dataset. Although averaging the IceBridge trends calculated over multiple epochs provides superior spatial coverage, particularly in the ice sheet interior, we note that this may introduce some inter-annual variability in the elevation rates. Therefore, we do not expect to see an exact correspondence between elevation rates measured by IceBridge and CryoSat-2 altimetry. Over short repeat periods the laser altimetry may capture short-term changes which are smoothed out by the longer time interval used for the radar altimetry. For example, in our 2011-2017 datasets, it is possible that moderate thickening not seen in the radar altimetry but present in two flight lines in the north-east beyond the LRM boundary (Figure 3.4j) is the result of short-term accumulation occurring between the laser survey dates (2013 and 2014).

Because the 2012 melt event is unique during the period of the CryoSat-2 data, its effect is more pronounced on rates of elevation change that are calculated over shorter time intervals (Figure 3.4). Over the full period of our survey (2011-2017), differences between regionally averaged rates of elevation change in the interior of the Greenland Ice Sheet are $\sim$ 1 cm/yr, regardless of which retracker is used (CFI or TCOG) or if

Figure 3.4: Rates of surface elevation change calculated at a resolution of 5 km for SARIn mode (smoothed with a 25 x 25 km median filter) using heights from the SARIn retracker, and at a resolution of 25 km for LRM (resampled to 5 km here using nearest neighbour interpolation for visualisation purposes) using heights calculated from the CFI and TCOG retracking algorithms. Results are shown for LRM solutions that have been both uncorrected (a, f, c, h) and corrected (b, g, d, i) for changes in radar penetration depth, and for the time periods 2011-2014 (top) and 2011-2017 (bottom). (e, j) Rates of elevation change derived from repeat IceBridge airborne laser altimetry. In each plot, the black line represents the boundary between LRM and SARIn mode acquisitions, and grey lines represent elevation contours of 2000, 2500 and 3000 m. Also shown in (e) is the boundary of the dry snow zone (purple), as defined in McMillan et al. (McMillan et al., 2016).

	CryoSat-2 – IceBridge elevation change statistics (>2000 m)					
	2011-2014			2011-2017		
	Mean difference (m/yr)	Standard deviation (m/yr)	Number of comparisons	Mean difference (m/yr)	Standard deviation (m/yr)	Number of comparisons
CFI retracker						
Uncorrected	0.20	0.10	135	0.01	0.11	585
Power correction	0.19	0.11	135	0.01	0.18	585
Penetration depth correction	0.06	0.08	135	0.01	0.10	585
TCOG retracker						
Uncorrected	0.07	0.08	135	0.02	0.10	585
Power correction	0.06	0.07	135	0.02	0.17	585
Penetration depth correction	0.03	0.07	135	0.02	0.10	585

Table 3.1: Statistics of the comparison between CryoSat-2 and Operation IceBridge rates of elevation change for the interior of the Greenland Ice Sheet (areas greater than 2000 m.a.s.l.) for the time periods 2011-2014 and 2011-2017.

a penetration depth correction is applied. In contrast, over shorter periods the 2012 melt event introduces a significant positive bias in rates of elevation change in the interior if uncorrected (Figure 3.4), as has been previously observed (Nilsson et al., 2016; Simonsen and Sørensen, 2017). This bias is much more apparent for elevation rates calculated from the CFI retracker (Fig. 3.4a), which displays differences up to 42 cm/yr relative to the rates determined from the laser altimetry. However, once changes in radar penetration depth have been accounted for using our penetration depth correction, the average elevation rate (2011-2014) within the LRM region is significantly reduced, from 14.6 $\pm$ 2.7 cm/yr to 2.4 $\pm$ 2.6 cm/yr. When applying the penetration depth correction to TCOG elevation time series over the same time period, we also find the elevation rate in the interior is reduced from 3.3 $\pm$ 1.4 cm/yr to -0.2 ± 1.3 cm/yr, on average. For comparison, the average rate of elevation change computed from airborne surveys falling within the LRM zone and between 2011-2014 is $-2.1 \pm$ 4.2 cm/yr. Although the airborne data are sufficient to conclude that the penetration depth correction to both the CFI and TCOG elevation data is effective, their spatial distribution is too sparse to pick which of the corrected CFI and TCOG solutions is more accurate for deriving long term elevation trends.

Examining rates of elevation change within the dry snow zone in more detail, it is

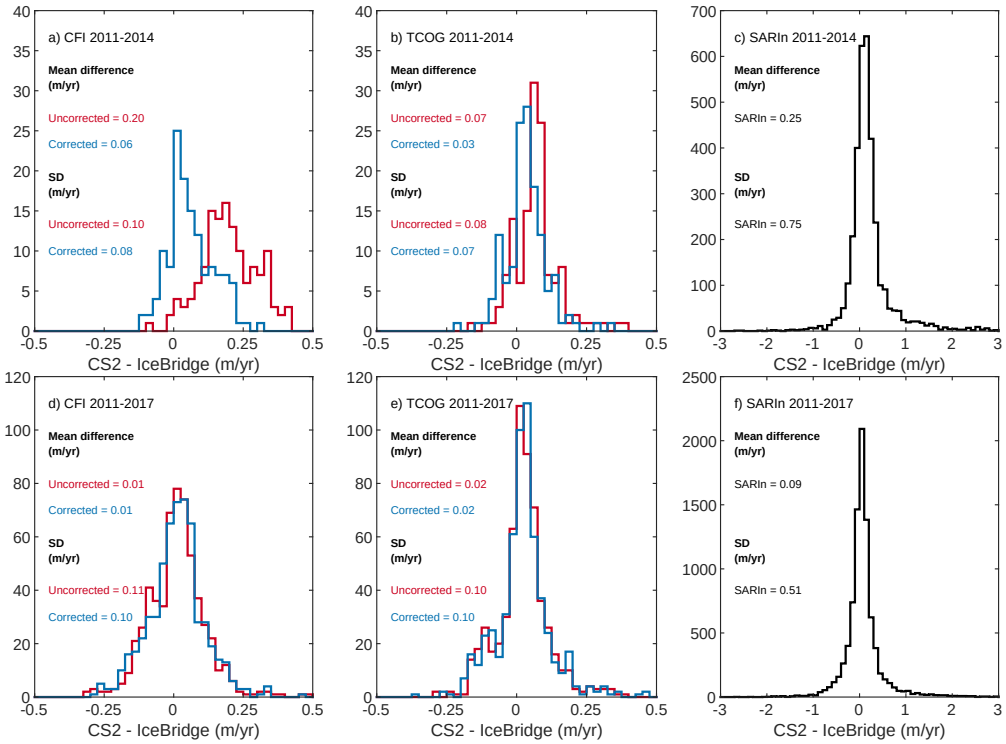

Figure 3.5: Comparison of uncorrected (red) and penetration depth corrected (blue) CryoSat-2 elevation rates to Operation IceBridge airborne laser altimetry rates between (top) January 2011 and December 2014 and (bottom) January 2011 and December 2017 for (a, d) CFI retracker, (b, e) TCOG retracker in the LRM zone, and (c, f) in the SARIn zone.

clear that the penetration depth correction reduces the positive bias induced by the 2012 melt event in comparison to the airborne data (Table 3.1, Figure 3.5), regardless of the retracker or whether the trends have been corrected for fluctuations in backscattered power. For the CFI algorithm, which is more sensitive to fluctuations in the radar scattering horizon, applying the retracker correction reduces the mean and standard deviation of the differences by 14 cm/yr and 2 cm/yr, respectively, when compared to the uncorrected data. Although designed to be less influenced by such fluctuations, our penetration correction also improves elevation rates derived from the TCOG algorithm, decreasing the mean difference and standard deviation by 4 cm/yr and 1 cm/yr, respectively. These results are comparable to an intercomparison to a different subset of IceBridge data over a similar time period performed in a previous study (Simonsen and Sørensen, 2017), which found a median difference of 1 cm/yr and standard deviation of 32 cm/yr when accounting for changes in the echo leading edge. Over the longer 2011-2017 survey period, both retrackers perform similarly well in all three scenarios when compared to the laser altimetry (Table 3.1). In each case, the effect of the penetration depth correction is negligible due to the reduced effect of the melt event on elevation rates derived from longer time intervals. Over both time periods we find reasonable agreement between elevation rates derived from SARIn and laser altimetry (Figure 3.5). Between 2011-2014 and 2011-2017 we calculate a mean difference and standard deviation of 25 cm/yr and 75 cm/yr, and 9 cm/yr and 51 cm/yr, respectively — a similar order of magnitude to previous studies where an evaluation against IceBridge laser altimetry has been performed (McMillan et al., 2016; Simonsen and Sørensen, 2017).

3.4 Conclusion

By deconvolving CryoSat-2 low-resolution mode altimeter echoes, we are able to provide a record of spatio-temporal variability in Ku band radar backscatter and penetration depth over the interior of the Greenland Ice Sheet between 2011-2017. Within this record we identify the melt event of 2012 as an isolated disruption to the radar scattering horizon, causing a widespread shift from volume to surface scattering and reducing the radar penetration depth by 2.34 $\pm$ 1.41 m on average in sectors of the ice sheet above 2000 m in altitude. Since then, a return to cooler atmospheric conditions (Bevis

et al., 2019) have allowed snowfall to accumulate across the interior of the ice sheet, and the scattering horizon has lowered, on average, to a depth of 3.28 ± 1.13 m — close to that seen before the melt event.

We show that changes in the penetration depth are correlated with changes in surface elevation determined from retracked radar altimeter waveform echoes, with typically 6 to 21 cm of elevation change occurring per metre variation in penetration depth. Accounting for the positive bias induced in elevation trends leads to improved agreement with respect to airborne laser altimetry — especially when calculated over short (<4 year) periods. When using an empirical retracker correction based upon changes in radar penetration depth, the mean bias is reduced by up to 14 cm/yr in the interior of the Greenland Ice Sheet. Over longer time periods, the correction is less important as the impact of the melt event on derived elevation trends becomes negligible. Elevation trends calculated from CryoSat-2 data processed with the TCOG retracker are much less affected by changes in penetration depth than those processed with the CFI retracker. Our study provides a physical basis for temporal variations in ice sheet elevation recorded during episodic melting events, and demonstrates an effective method to compensate for these signals through waveform deconvolution. Here our approach requires the use both Level 1 and 2 data products: in future implementing the waveform deconvolution within a Level 2 processor would allow fluctuations in penetration depth to be compensated for on an individual waveform basis.

References

Armitage, T. W. K., Wingham, D. J., and Ridout, A. L. (2014). Meteorological origin of the static crossover pattern present in low-resolution-mode CryoSat-2 data over central Antarctica. *IEEE Geoscience and Remote Sensing Letters*, 11(7):1295–1299. 72

Arthern, R. J., Wingham, D. J., and Ridout, A. L. (2001). Controls on ERS altimeter measurements over ice sheets: Footprint-scale topography, backscatter fluctuations, and the dependence of microwave penetration depth on satellite orientation. *Journal of Geophysical Research: Atmospheres*, 106(D24):33471–33484. 72, 74, 75, 76, 83

Bevis, M., Harig, C., Khan, S. A., Brown, A., Simons, F. J., Willis, M., Fettweis, X., van den Broeke, M. R., Madsen, F. B., Kendrick, E., Caccamise, D. J., van Dam, T., Knudsen, P., and Nylen, T. (2019). Accelerating changes in ice mass within Greenland, and the ice sheet's sensitivity to atmospheric forcing. *Proceedings of the National Academy of Sciences*, page 201806562. 90

Brown, G. (1977). The average impulse response of a rough surface and its applications. *IEEE Transactions on Antennas and Propagation*, 25(1):67–74. 74

Casey, K. A., Polashenski, C. M., Chen, J., and Tedesco, M. (2017). Impact of MODIS sensor calibration updates on Greenland ice sheet surface reflectance and albedo trends. *The Cryosphere*, 11(4):1781–1795. 72

Davis, C. H. (1993). A surface and volume scattering retracking algorithm for ice sheet satellite altimetry. *IEEE Transactions on Geoscience and Remote Sensing*, 31(4):811–818. 73

Davis, C. H. (1997). A robust threshold retracking algorithm for measuring ice-sheet surface elevation change from satellite radar altimeters. *IEEE Transactions on Geoscience and Remote Sensing*, 35(4):974–979. 72, 78

Davis, C. H. and Ferguson, A. C. (2004). Elevation change of the Antarctic ice sheet, 1995-2000, from ERS-2 satellite radar altimetry. *IEEE Transactions on Geoscience and Remote Sensing*, 42(11):2437–2445. 80, 81

Davis, C. H. and Moore, R. K. (1993). A combined surface-and volume-scattering model for ice-sheet radar altimetry. *Journal of Glaciology*, 39(133):675–686. 72, 73

Davis, C. H. and Zwally, H. J. (1993). Geographic and seasonal variations in the surface properties of the ice sheets by satellite-radar altimetry. *Journal of Glaciology*, 39(133):687–697. 72

ESA (2012). CryoSat-2 Product Handbook, ESRIN-ESA and Mullard Space Science Laboratory University College London, available at: http://emits.sso.esa.int/emits-doc/ESRIN/7158/CryoSat-PHB-17apr2012.pdf (last access: October 2017). 78, 81

Fettweis, X., Hanna, E., Lang, C., Belleflamme, A., Erpicum, M., and Gallée, H. (2013). Brief communication: Important role of the mid-tropospheric atmospheric circulation in the recent surface melt increase over the Greenland ice sheet. *The Cryosphere*, 7(1):241–248. 72

Flament, T. and Rémy, F. (2012). Dynamic thinning of Antarctic glaciers from along-track repeat radar altimetry. *Journal of Glaciology*, 58(211):830–840. 78, 81

Franco, B., Fettweis, X., and Erpicum, M. (2013). Future projections of the Greenland ice sheet energy balance driving the surface melt. *The Cryosphere*, 7(1):1–18. 84

Helm, V., Humbert, A., and Miller, H. (2014). Elevation and elevation change of Greenland and Antarctica derived from CryoSat-2. *The Cryosphere*, 8(4):1539–1559. 72, 73, 78, 86

Johannessen, O. M., Khvorostovsky, K., Miles, M. W., and Bobylev, L. P. (2005). Recent ice-sheet growth in the interior of Greenland. *Science*, 310(5750):1013–1016. 72

Joughin, I., Smith, B., Howat, I., and Scambos, T. (2015). MEaSUREs Greenland Ice Sheet velocity map from InSAR data, version 2, National Snow and Ice Data Center, Boulder, Colorado, USA, available at: https://nsidc.org/icebridge/portal/ (last access January 2019). 82

Joughin, I., Smith, B. E., Howat, I. M., Scambos, T., and Moon, T. (2010). Greenland flow variability from ice-sheet-wide velocity mapping. *Journal of Glaciology*, 56(197):415–430. 82

Khvorostovsky, K. S. (2012). Merging and analysis of elevation time series over Greenland ice sheet from satellite radar altimetry. *IEEE Transactions on Geoscience and Remote Sensing*, 50(1):23–36. 80

Leeson, A. A., Eastoe, E., and Fettweis, X. (2018). Extreme temperature events on Greenland in observations and the MAR regional climate model. *The Cryosphere*, 12(3):1091–1102. 83, 84

Marquardt, D. W. (1963). An algorithm for least-squares estimation of nonlinear parameters. *Journal of the Society for Industrial and Applied Mathematics*, 11(2):431–441. 75

Matzler, C. (1996). Microwave permittivity of dry snow. *IEEE Transactions on Geoscience and Remote Sensing*, 34(2):573–581. 72, 75

McMillan, M., Leeson, A., Shepherd, A., Briggs, K., Armitage, T. W. K., Hogg, A., Kuipers Munneke, P., van den Broeke, M., Noël, B., van de Berg, W. J., Ligtenberg, S., Horwath, M., Groh, A., Muir, A., and Gilbert, L. (2016). A high-resolution record of Greenland mass balance. *Geophysical Research Letters*, 43(13):7002–7010. xvi, 72, 73, 78, 80, 81, 82, 83, 86, 87, 90

Mote, T. L. (2007). Greenland surface melt trends 1973–2007: Evidence of a large increase in 2007. *Geophysical Research Letters*, 34(22). 73

Nghiem, S. V., Hall, D. K., Mote, T. L., Tedesco, M., Albert, M. R., Keegan, K., Shuman, C. A., DiGirolamo, N. E., and Neumann, G. (2012). The extreme melt across the Greenland ice sheet in 2012. *Geophysical Research Letters*, 39(20). 72, 73

Nilsson, J., Gardner, A., Sandberg Sørensen, L., and Forsberg, R. (2016). Improved retrieval of land ice topography from CryoSat-2 data and its impact for volume-change estimation of the Greenland ice sheet. *The Cryosphere*, 10(6):2953–2969. 72, 73, 78, 80, 82, 86, 88

Nilsson, J., Vallelonga, P., Simonsen, S. B., Sørensen, L. S., Forsberg, R., Dahl-Jensen, D., Hirabayashi, M., Goto-Azuma, K., Hvidberg, C. S., Kjaer, H. A., and Satow, K. (2015). Greenland 2012 melt event effects on CryoSat-2 radar altimetry. *Geophysical Research Letters*, 42(10):3919–3926. xv, 73, 77, 80, 84, 85

Partington, K. C., Ridley, J. K., Rapley, C. G., and Zwally, H. J. (1989). Observations of the surface properties of the ice sheets by satellite radar altimetry. *Journal of Glaciology*, 35(120):267–275. 73

Ridley, J. K. and Partington, K. C. (1988). A model of satellite radar altimeter return from ice sheets. *International Journal of Remote Sensing*, 9(4):601–624. 72, 74

Sandberg Sørensen, L., Simonsen, S. B., Forsberg, R., Khvorostovsky, K., Meister, R., and Engdahl, M. E. (2018). 25 years of elevation changes of the Greenland ice sheet from ERS, Envisat, and CryoSat-2 radar altimetry. *Earth and Planetary Science Letters*, 495:234–241. 72, 73

Shepherd, A., Ivins, E. R., A, G., Barletta, V. R., Bentley, M. J., Bettadpur, S., Briggs, K. H., Bromwich, D. H., Forsberg, R., Galin, N., Horwath, M., Jacobs, S., Joughin, I., King, M. A., Lenaerts, J. T. M., Li, J., Ligtenberg, S. R. M., Luckman, A., Luthcke, S. B., McMillan, M., Meister, R., Milne, G., Mouginot, J., Muir, A., Nicolas, J. P., Paden, J., Payne, A. J., Pritchard, H., Rignot, E., Rott, H., Sørensen, L. S., Scambos, T. A., Scheuchl, B., Schrama, E. J. O., Smith, B., Sundal, A. V., van Angelen, J. H., van de Berg, W. J., van den Broeke, M. R., Vaughan, D. G., Velicogna, I., Wahr, J., Whitehouse, P. L., Wingham, D. J., Yi, D., Young, D., and Zwally, H. J. (2012). A reconciled estimate of ice-sheet mass balance. *Science*, 338(6111):1183. 72

Simonsen, S. B. and Sørensen, L. S. (2017). Implications of changing scattering properties on Greenland ice sheet volume change from CryoSat-2 altimetry. *Remote Sensing of Environment*, 190:207–216. 72, 73, 80, 82, 86, 88, 90

Studinger, M. (2014). Icebridge ATM L4 surface elevation rate of change, Version 1, National Snow and Ice Data Center, Boulder, Colorado, USA, available at: https://nsidc.org/icebridge/portal/ (last access January 2019). 82

Tedesco, M., Fettweis, X., Mote, T., Wahr, J., Alexander, P., Box, J. E., and Wouters, B. (2013). Evidence and analysis of 2012 Greenland records from spaceborne observations, a regional climate model and reanalysis data. *The Cryosphere*, 7(2):615–630. 73, 83, 84

Wingham, D. J., Francis, C. R., Baker, S., Bouzinac, C., Brockley, D., Cullen, R., de Chateau-Thierry, P., Laxon, S. W., Mallow, U., Mavrocordatos, C., Phalippou, L., Ratier, G., Rey, L., Rostan, F., Viau, P., and Wallis, D. W. (2006). CryoSat: A mission to determine the fluctuations in Earth's land and marine ice fields. *Advances in Space Research*, 37(4):841–871. 72, 73, 81

Wingham, D. J., Phalippou, L., Mavrocordatos, C., and Wallis, D. (2004). The mean echo and echo cross product from a beamforming interferometric altimeter and their application to elevation measurement. *IEEE Transactions on Geoscience and Remote Sensing*, 42(10):2305–2323. 74, 81

Wingham, D. J., Rapley, C. G., and Griffiths, H. (1986). New techniques in satellite altimeter tracking systems. In *18th IGARSS Symposium*. 78

Wingham, D. J., Ridout, A. J., Scharroo, R., Arthern, R. J., and Shum, C. K. (1998). Antarctic elevation change from 1992 to 1996. *Science*, 282(5388):456–458. 80

Wingham, D. J. and Wallis, D. W. (2010). The rough surface impulse response of a pulse-limited altimeter with an elliptical antenna pattern. *IEEE Antennas and Wireless Propagation Letters*, 9:232–235. 73

Chapter 4

Seasonal elevation changes in the Greenland Ice Sheet from CryoSat-2 altimetry

Authors: **Thomas Slater, Andrew Shepherd, Malcolm McMillan, Amber Leeson, Anna E. Hogg, Lin Gilbert, Alan Muir, Kate Briggs**

Abstract

Seasonal changes in the elevation of the Greenland Ice Sheet below the equilibrium line altitude are driven by ice dynamics and fluctuations in surface melting and snowfall accumulation. Here, for the first time, we use CryoSat-2 altimetry to estimate summer and winter elevation changes in the ice sheet ablation zone between 2011 and 2017. During this period, we find average summer and winter elevation trends of -3.67 ± 0.93 m/yr and 0.69 ± 0.41 m/yr, respectively. Our altimeter record of monthly height change is strongly correlated with regional climate model reconstructions of elevation change due to surface processes alone in both summer ($R = 0.99$) and winter ($R = 0.98$), and tracks ice sheet meteorology. While the rate at which the ablation zone thickens in the winter due to snowfall has remained relatively stable, spatial and temporal variations in ice thinning in the summer due to surface melting have followed recent changes in atmospheric circulation. We find the rate of thinning peaked at -5.21 ± 0.33 m/yr during the extreme summer of 2012. After this rate halved (-2.59 ± 0.61 m/yr) in

the following summer, when low pressure and temperature conditions prevailed, the summer thinning rate has increased year-on-year to -3.62 ± 0.55 m/yr in the summer of 2017. Between 2011 and 2017, we estimate that the ablation zone of the Greenland Ice Sheet has thinned by 3.22 ± 0.50 m from CryoSat-2 altimetry.

4.1 Introduction

Surface mass balance is a key component of ice sheet mass balance (Mouginot et al., 2019; Shepherd et al., 2012) and provides meltwater for surface (Das et al., 2008; Leeson et al., 2014; Zwally et al., 2002), englacial (Catania and Neumann, 2010) and subglacial hydrological systems (Andrews et al., 2014; Bowling et al., 2019). Both ice sheet melting and accumulation are expected to increase in the future due to global heating (Fettweis et al., 2013a; Golledge et al., 2019). With only sparse in situ observations provided by automatic weather stations (Leeson et al., 2018), and remote observations limited to measurements of melt extent (Tedesco et al., 2013), regional estimates of seasonal melt and accumulation are mainly derived from regional climate models (e.g. (Ettema et al., 2009; Fettweis et al., 2017; Noël et al., 2018)). Over the past two decades, 55 % of ice losses in Greenland have been driven by changes in surface mass balance (Mouginot et al., 2019), as a result of increasing ablation (Enderlin et al., 2014; Trusel et al., 2018; van den Broeke et al., 2016) driven by atmospheric circulation enhancing warming in the summer months (Fettweis et al., 2013b; Hanna et al., 2012; van Angelen et al., 2014) and decreasing snowfall (Bevis et al., 2019).

Signals of surface lowering brought about by changes in ice sheet surface mass balance have been resolved by satellite radar altimeters, and in particular CryoSat-2, which has successfully measured elevation changes in the difficult terrain found in the ablation zone due to its interferometric capability (e.g. (Gray et al., 2019; Helm et al., 2014; McMillan et al., 2016; Nilsson et al., 2016; Sandberg Sørensen et al., 2018; Simonsen and Sørensen, 2017)). In addition, ice sheet elevation change arising from surface mass balance and firn processes only has been reconstructed with regional climate models (Kuipers Munneke et al., 2015; Ligtenberg et al., 2018). Knowledge of ice sheet meteorology provided by regional climate models can be used in conjunction with satellite observations of elevation change (Forsberg et al., 2017; Khan et al., 2014; McMillan

et al., 2016; Shepherd et al., 2012; Sørensen et al., 2011; Thomas et al., 2006), and ice flow (Enderlin et al., 2014; Mouginot et al., 2015; Rignot et al., 2011; van den Broeke et al., 2009, 2016), to partition ice imbalance in Greenland due to ice-dynamical and surface mass balance processes. Here we use CryoSat-2 radar altimetry to separate long-term and seasonal elevation changes, and map summer melting and winter snowfall in the ablation zone of the Greenland Ice Sheet between 2011-2017. We then compare these results to output from a semi-empirical firn densification model (Ligtenberg et al., 2011, 2018) forced by surface mass fluxes and temperature from a polar regional climate model (Noël et al., 2018).

4.2 Data and Methods

We compute linear rates of surface elevation change and monthly height evolution from CryoSat-2 radar altimeter observations acquired between January 2011 and December 2017. In total, we used over 34 million measurements of ice sheet elevation provided in the level 2i baseline-C product, which are corrected for echo deviations from the onboard tracking gate, off-nadir ranging due to slope, dry atmosphere, wet atmosphere, ionosphere, and solid-earth tide (ESA, 2012). Using a model fit method (e.g. (Flament and Rémy, 2012; McMillan et al., 2016; Simonsen and Sørensen, 2017)), we generate time series and trends of ice sheet surface elevation change on a 5 x 5 km grid (e.g. Figure 4.1a), allowing for elevation fluctuations caused by topography (x,y), satellite heading (h) and time (t):

$$z(x,t,y,h) = \bar{z} + a_0 x + a_1 y + a_2 x^2 + a_3 y^2 + a_4 xy + a_5 h + a_6 t \tag{4.1}$$

We solve for the individual model coefficients using an iterative least-squares fit to minimise the impact of outliers, and discard any unrealistic estimates from poorly constrained solutions based on a set of statistical thresholds which include: a minimum of 40 data points, a time series length of at least 2 years, a maximum root mean squared difference of elevation residuals from the model of 12 m, a maximum elevation rate magnitude of 10 m/yr, and a maximum surface slope of 5°.

To account for temporal variations in range associated with changes in radar echo shape, we apply an empirical correction based upon correlated changes in elevation

and backscattered power (Davis and Ferguson, 2004; McMillan et al., 2014). We first compute the correlation gradient in elevation as a function of power, $\frac{dh}{dp}$, using a linear fit in each grid cell over a 60-month time window. We then multiply time series of changes in backscattered power dp by this gradient to estimate the backscatter correction term, which we remove from our original elevation change time series dh:

$$dh_{corrected} = dh - (dp\frac{dh}{dp}) \tag{4.2}$$

Although previous studies have also adapted backscatter corrections to account for the effects of an episodic change in snowpack characteristics on the shape of altimeter echoes (e.g. (McMillan et al., 2016; Simonsen and Sørensen, 2017)) due to widespread melting in the ice sheet interior (Nghiem et al., 2012; Nilsson et al., 2015), here we do not as (1) the threshold offset centre of gravity retracker we use (Davis, 1997) is less sensitive to changes in volume scatter than physically based algorithms, and (2) we only examine elevation trends in the ice sheet interior, which are less affected by the melt event when determined over longer time periods (Chapter 3). At the ice sheet margins where CryoSat-2 operates in synthetic aperture radar interferometry mode (SARIn), we use the ESA Level 2 SARIn retracker, which fits an analytical model to individual SAR waveforms (ESA, 2012; Wingham et al., 2006).

Across a small proportion (9 %) of the ice sheet area our method fails to retrieve a solution, and we estimate elevation trends in this region instead using an empirical model based upon latitude (l), elevation (z) and velocity change (Δv, which accounts for elevation changes due to ice-dynamical and temperature-related processes) (McMillan et al., 2016) (Eq. 4.3). Where no velocity data are available, we model elevation changes as a function of latitude and elevation only.

$$\frac{dz}{dt} = al + bz + c\Delta v + d \tag{4.3}$$

Based upon the root mean squared difference of the residuals to the model fit, we estimate an average uncertainty in unobserved grid cells of 0.4 m/yr. To evaluate our estimates derived from CryoSat-2 altimetry we compare our results to 11,404 contemporaneous and independent elevation trends derived from Operation IceBridge airborne laser altimetry (Studinger, 2014): the mean and standard deviation of the differences (CryoSat − IceBridge) is 11 cm/yr, and 59 cm/yr, respectively.

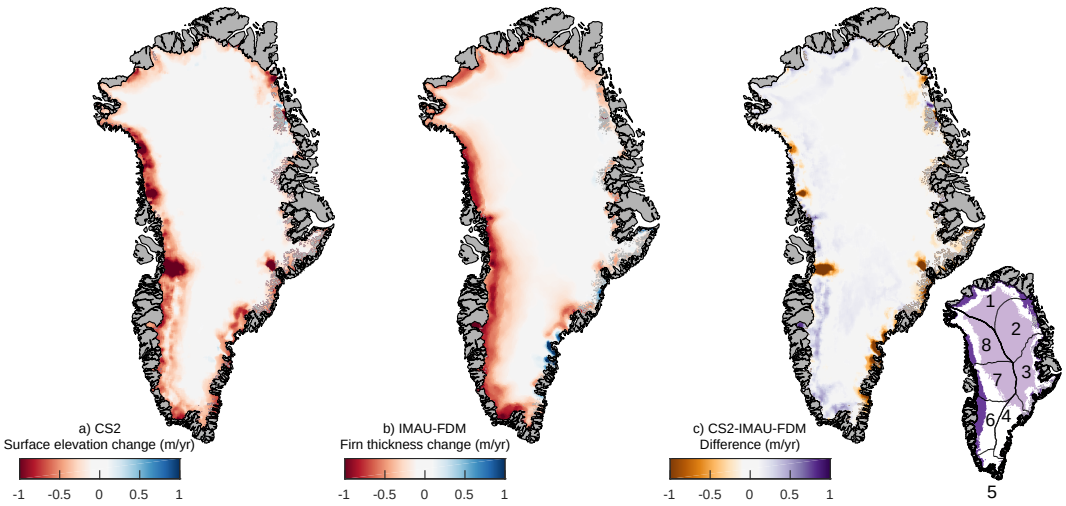

Figure 4.1: Greenland elevation change 2011-2017. (a) Rate of surface elevation change between January 2011 and December 2017 from CryoSat-2 radar altimetry. (b) Rate of elevation change between January 2011 and December 2017 due to surface mass balance and firn processes only from the IMAU-FDM firn densification model. (c) Difference (radar altimetry − firn model) between the derived trends. For visualisation purposes, the maps have been smoothed with a 25 by 25 km median filter. (Right inset) Ice sheet dry snow (light) and ablation (dark) zones and definition of principal ice sheet drainage basins (Zwally et al., 2012)

We simulate surface elevation changes due to firn compaction and surface mass balance processes during the period of our satellite altimeter record using the Institute for Marine and Atmospheric Research Utrecht firn densification model (IMAU-FDM). IMAU-FDM simulates the time evolution of firn compaction, temperature, liquid water content, and surface elevation in a vertical 1-D column of firn and ice at high spatial (11 km) and temporal (10 day) resolution (Kuipers Munneke et al., 2015; Ligtenberg et al., 2011, 2018). IMAU-FDM uses an expression for firn- densification (Arthern et al., 2010) adapted to fit *in-situ* density profiles retrieved from the Greenland Ice Sheet (Kuipers Munneke et al., 2015), and covers the period 1960-2017. The surface layer of the firn column is forced by surface mass balance components (solid and liquid precipitation, surface and drifting snow sublimation, drifting snow erosion, surface melt), surface temperature and 10 m wind speed at 11 km horizontal and sub-daily (3-6 hour) temporal resolution from the RACMO2.3p2 regional climate model (Ligtenberg et al., 2018; Noël et al., 2018). Surface elevation changes are computed with respect to the spin-up period (1960-1979), over which zero surface elevation change due to firn and surface mass balance processes is assumed (Kuipers Munneke et al., 2015). In the ablation zone, where there is no firn layer, elevation changes are modelled due to surface mass balance processes alone. To compare firn model outputs to the satellite observations, we resample the gridded firn model time series to a spatial (5 x 5 km) and temporal (monthly) domain common to that used for the radar altimetry through bilinear interpolation. We then obtain average rates of elevation change due to surface mass balance and firn processes through fitting a linear trend to the firn height anomaly time series in each grid cell (e.g. Figure 4.1b).

We compute time-varying surface height evolution in the ice sheet accumulation and ablation zones at monthly intervals from the CryoSat-2 measurements and IMAU-FDM by averaging gridded monthly elevation anomalies. To ensure comparison within equivalent areas we mask the firn model output to the spatial coverage of the satellite observations at each epoch. We use definitions of the ablation and dry snow zones described in McMillan et al. (2016) and Leeson et al. (2018) according to RACMO simulations of melting and surface mass balance: the ablation zone (Figure 4.1) is taken as the area of

the ice sheet below the equilibrium line (i.e. negative surface mass balance) in a majority of years between 2009 and 2014, and the dry snow zone is defined as the area where melting never exceeded 5 mm w.e. on any given day during this period (van Angelen et al., 2014). We do not compare monthly time series in the south-eastern sectors of the ice sheet (basins 3, 4 and 5), as in this region the ablation zone is small (10 % of the ice sheet ablation area in total, Figure 4.1), and the rugged terrain is challenging for both radar altimeters and regional climate models. We quantify the uncertainty on the altimeter elevation estimates at each epoch by computing the regional average of the standard error of height change within all contributing pixels. Assuming this component is temporally uncorrelated, we then accumulate all preceding uncertainties in quadrature at any given epoch. For the firn model outputs we use error estimates evaluated from the variability due to the reference climate (Kuipers Munneke et al., 2015).

4.3 Results

Our CryoSat-2 record resolves clear patterns of thinning at large outlet glaciers and along the ice sheet margins (particularly the western coast): signals which have been previously identified in altimeter surveys over shorter time periods (e.g. (McMillan et al., 2016; Nilsson et al., 2016; Sandberg Sørensen et al., 2018; Simonsen and Sørensen, 2017)) (Figure 4.1a). Coherent thinning at the ice sheet margins and away from outlet glaciers has been predominantly associated with increased surface runoff (Kuipers Munneke et al., 2015; van den Broeke et al., 2016) resulting from warmer atmospheric conditions and exceptional melt episodes during the first years of our study period (Bevis et al., 2019; Hanna et al., 2014). We separate time series in the ice sheet dry snow and ablation zones to understand variations in the spatial pattern of Greenland Ice Sheet elevation change (Figure 4.2). Height fluctuations in the ice sheet ablation zone are governed by a seasonal cycle of surface melting in the summer months (May – August) and snowfall in the winter (September – April). No such seasonal signal is evident in the dry snow zone, where atmospheric temperatures are too low in general to force surface melting (with the exception of the summer of 2012 (Nghiem et al., 2012), and elevation changes are instead controlled by interannual variations in snowfall. Although there has been little to no change in the elevation of the ice

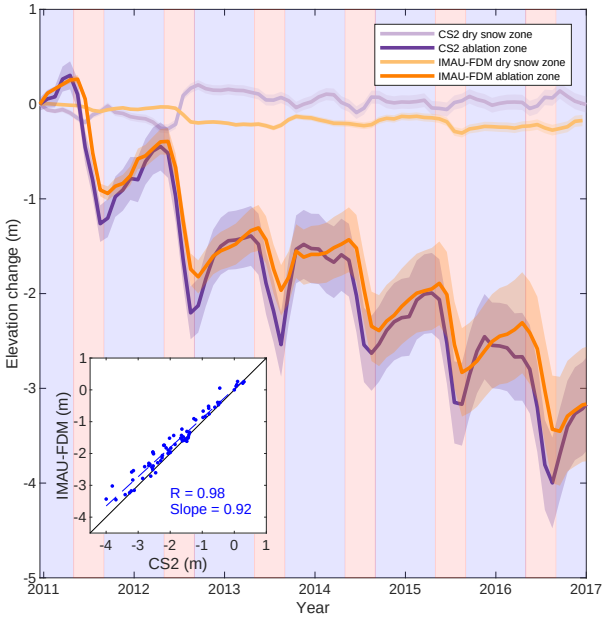

Figure 4.2: Surface height evolution in the accumulation and ablation zone of the Greenland Ice Sheet. Monthly evolution in ice surface height from CryoSat-2 altimetry (purple) and IMAU-FDM (orange) for the ice sheet dry snow (light) and ablation (dark) zones. Shaded regions indicate summer (red) and winter (blue) periods used to compute seasonal elevation changes. The inset scatter plot shows a linear regression between monthly elevation change values in the ice sheet ablation zone derived from CryoSat-2 and regional climate modelling, together with the linear regression coefficients.

sheet interior, in the ablation zone summer losses have far exceeded winter gains: from CryoSat-2 altimetry we estimate that the ablation zone has thinned by approximately 3.22 $\pm$ 0.50 m on average over the period 2011-2017.

To reduce the impact of short term variations in the CryoSat-2 and IMAU-FDM time series we applied linear fits to the data over summer and winter periods, before using these trends to derive seasonal elevation changes (Figure 4.3). To derive the seasonal

elevation rates, we smooth the time series using a 3 month Gaussian-weighted moving average before fitting a linear trend to summer and winter elevation changes between January 2011 and December 2017 across the ablation zone as a whole, and partitioned into the principal ice sheet drainage basins (Zwally et al., 2012). In each region we define the summer period over which we fit the trends according to the corresponding period of melting taken from RACMO, and define the winter period as the surrounding months. Across the ablation zone our definition of summer is typically May 1st to August 31st, with shorter ablation periods in the northernmost basins. To obtain the error on the seasonal rate of elevation change, we combine the elevation uncertainty with the standard error of the rate of surface elevation change in quadrature, in order to account for systematic errors which may affect the trend.

From our CryoSat-2 time series we identify the highest rate of thinning occurring across the ice sheet ablation zone in the summer of 2012 (-5.21 ± 0.33 m/yr), relating to an exceptionally warm summer (Hanna et al., 2014; Nghiem et al., 2012; Tedesco et al., 2013) which saw record mass losses due to surface melting, enhanced by a strongly negative North Atlantic Oscillation (NAO) (Fettweis et al., 2013b; McMillan et al., 2016; van Angelen et al., 2014). A significant reduction in summer thinning in the following year (-2.59 ± 0.61 m/yr) is consistent with an abrupt shift to a positive NAO, bringing low-pressure and low-temperature conditions (Bevis et al., 2019). In the summer of 2016, a higher rate of thinning (-3.62 ± 0.55 m/yr) coincides with a return to warmer atmospheric conditions and a negative phase of the NAO. In the winter, we note that both the magnitude and interannual variability in elevation trends is significantly reduced when compared to summer across the ablation zone, and range from 0 to 1 m/yr. Partitioning seasonal elevation changes into individual drainage basins (Figure 4.3), we find thinning associated with the extreme melt in the summer of 2012 is highest in the west (basin 7) and south-western (basin 6) sectors, over which warm southerly air is advected during a negative phase of the NAO (Fettweis et al., 2013b). Although elevation rates are reduced in all basins during the summer of 2013, in line with the return of cooler atmospheric conditions brought about by a positive NAO phase, they are significantly lower in the northern basins (1, 2 and 8). In the same regions, high thinning derived from both techniques in the summer of 2015 reflect an exceptional atmospheric circulation pattern which enhanced surface melting in the north (Tedesco et al., 2016).

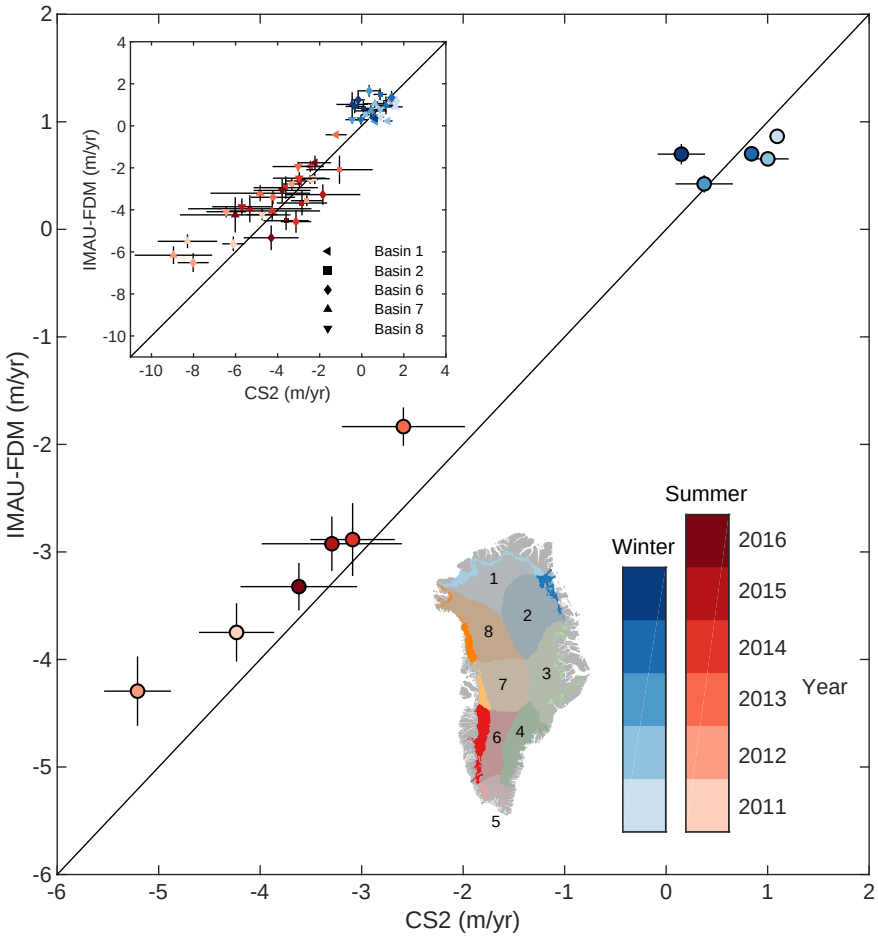

Figure 4.3: Seasonal elevation changes in the ablation zone of the Greenland Ice Sheet. Summer (red) and winter (blue) rates of surface elevation change derived from CryoSat-2 altimetry and IMAU-FDM during the period 2011-2017 for the entire ice sheet ablation zone and six large drainage basins (inset).

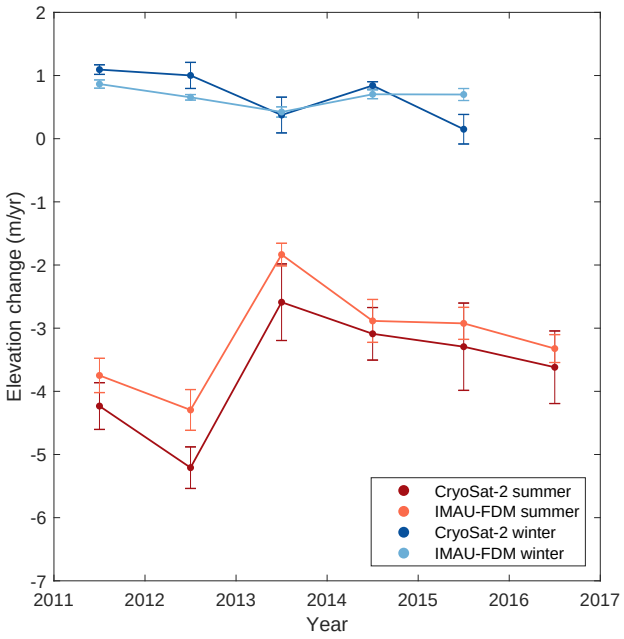

Figure 4.4: Temporal variability in seasonal elevation changes in the ablation zone of the Greenland Ice Sheet. Summer (red) and winter (blue) rates of surface elevation change derived from CryoSat-2 altimetry (dark) and IMAU-FDM (light) during the period 2011-2017 for the ice sheet ablation zone.

Over the 7-year record there is broad agreement between satellite measurements of surface elevation change and model estimates of firn layer thickness change (Figure 4.1c). Both CryoSat-2 and IMAU-FDM show strong seasonal changes in elevation at the ice sheet margin, and lower variability in the interior: when comparing the monthly elevation change estimates in the ablation zone (Figure 4.2), we find close agreement for the time series as a whole ($R = 0.98$), and during the summer ($R = 0.99$) and winter ($R = 0.98$) months. Seasonal rates of surface elevation change determined from CryoSat-2 altimetry and the IMAU-FDM also agree well across the ice sheet ablation zone (median difference (CS2 − IMAU-FDM) −0.06 m/yr , root-mean squared difference (RMS) 0.4 m/yr) (Figure 4.3). Generally, seasonal elevation changes derived from both datasets

across the entire ablation zone agree better in the summer (RMS = 0.40 m/yr) than in winter (RMS = 0.48 m/yr). When decomposed into the principal drainage basins, the agreement between seasonal trends derived from CryoSat-2 altimetry and regional climate modelling is reduced when compared to the ice sheet as a whole (Figure 4.3): across all regions, seasonal elevation rates typically agree to around 1 m/yr (RMS = 1.06 m/yr). Overall, CryoSat-2 matches IMAU-FDM in capturing the interannual variability in seasonal elevation trends which emerge from the sensitivity of the ice sheet to changes in atmospheric forcing (Figure 4.4).

4.4 Discussion

Differencing the CryoSat-2 altimetry and IMAU-FDM elevation change fields removes the simulated surface mass balance component, and allows us to investigate discrepancies which may arise due to model or observational errors, and signals which are dynamical in origin. Departures arise at several marine-terminating glacier systems known to be dynamically out of balance during our study period: the most notable example is Jakobshavn Isbræ, where observed surface thinning trends which exceed modelled firn thickness changes are supported by independent observations of dynamic activity (Joughin et al., 2014; Lemos et al., 2018), and are clearly defined within the glacier. Other glaciers known to be in a state of dynamical imbalance and where the altimeter elevation trends are more negative include Zachariae Isstrøm (Mouginot et al., 2015), Kangerlussuaq (Kehrl et al., 2017) and Upernavik Isstrøm (Larsen et al., 2016). We also find evidence of continued dynamic thickening at Storstrømmen in the northeast, where ice flow has slowed after the glacier surged between 1978 and 1984 (Mohr et al., 1998). We note the presence of a strip of zero elevation change along the south western margin in the altimetry that is not present in the firn model (Figure 4.1). Comparing to Operation IceBridge airborne laser altimetry within this region we find better agreement with CryoSat-2 elevation trends (3 cm/yr) than IMAU-FDM (-30 cm/yr). Examining changes in ice velocity will help determine if this is ice dynamical in origin: localised thickening due to slowdown (Tedstone et al., 2015) may be offsetting thinning due to summer melting. We do not, however, rule out the possibility of this signal being the artefact of a migrating radar scattering horizon.

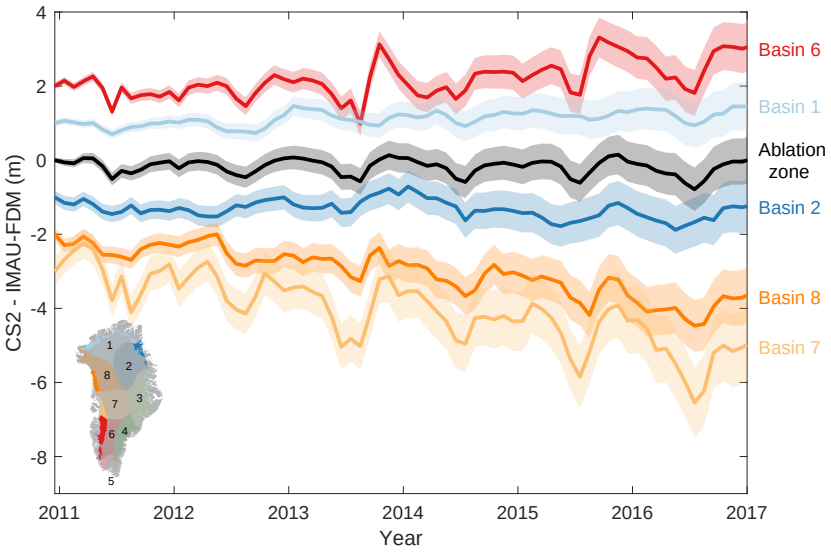

Figure 4.5: Difference between observed changes in the surface elevation and simulated changes in the firn layer of the ablation zone of the Greenland Ice Sheet (black) and six drainage basins (colours). For visualisation purposes, individual time series are offset by 1 m and ordered according to the trend in the residuals (positive to negative).

Examining the local differences between surface elevation changes derived from CryoSat-2 altimetry and elevation changes due to surface mass balance processes from IMAU-FDM provides insight into the evolution of ice dynamical imbalance within the ice sheet ablation zone (Figure 4.5). A positive trend in the residual height change suggests dynamic thickening in the southwest (basin 6), consistent with contemporaneous observations of slowdown across an 8000 km^2 land-terminating region which extends up to 80 km inland, despite a 50 % increase in surface meltwater production (Tedstone et al., 2015). Progressive dynamic thinning in the western sector of the ablation zone (basin 7) is dominated by the imbalance at Jakobshavn Isbræ. Similarly in northwest Greenland (basin 8), a region known to be thinning dynamically (Khan et al., 2014), observations have detected a modest multiyear speed up across a network of outlet glaciers (Moon et al., 2015). Seasonal elevation changes in the west (basin 7) and northwest (basin 8) sectors of the ice sheet may be driven by seasonal changes in ice

flow (e.g. ice speed was found to increase by up to 50 % at Jakobshavn Isbræ in the summer of 2012 (Joughin et al., 2014)). Although individual basins exhibit differing long-term trends, in general they display the same seasonal cycle of enhanced thinning in summer, and modest accumulation in the winter.

In addition to the ice dynamical signals which can lead to the reported departure between changes in surface elevation and firn thickness derived from altimetry and regional climate modelling respectively, we note residual differences may also be associated with sources of error in the individual datasets. These include the reference climate used to initialise IMAU-FDM to force changes in firn height, or a reduced ability to capture extreme melt events due to the underestimation of sensible heat fluxes in low-lying regions at the ice sheet margins within the regional climate model during exceptionally warm summers (Noël et al., 2018). In addition, the regional climate model may underestimate surface melting in the complex terrain of the ice marginal areas, which are poorly resolved at 11 km resolution (Kuipers Munneke et al., 2015; Noël et al., 2018). Similarly for the altimetry, there are challenges associated with monitoring the rugged terrain found in the ice sheet margins. Reduced agreement between seasonal trends in winter may be in part due to uncompensated altimeter signals resulting from changes in radar penetration depth which arise from the accumulation of snow on the ice sheet surface, and the downward movement of ice lenses formed by summer melting (Gray et al., 2019). Because the ablation zone melts to bare ice in the summer, we do not expect the presence of such signals in summer elevation changes derived from the altimetry.

4.5 Conclusion

Using CryoSat-2 radar altimetry we examine elevation changes driven by melting and snowfall accumulation in the ablation zone of the Greenland Ice Sheet. Comparing these data to elevation changes due to surface mass balance processes from a regional climate model, we find good agreement between monthly height evolution and seasonal rates of elevation change derived from both datasets, and suggest that CryoSat-2 is able to measure elevation changes associated with summer melt and winter accumulation. In general we find CryoSat-2 is able to better monitor elevation changes in the summer,

and suggest the reduced skill in winter is due to the effects of variable radar penetration. Between 2011 and 2017, elevation change in the ablation zone has been driven by surface melting in the summer and has tracked changes in atmospheric forcing: the observed rate of elevation change peaked at -5.21 ± 0.33 m/yr during the summer of 2012 and halved in 2013 as atmospheric circulation favoured warmer and cooler conditions, respectively. In contrast, the observed winter accumulation rate has been relatively stable and has averaged 0.69 ± 0.41 m/yr between 2011 and 2017. Combining altimetry and regional climate model simulations, we examine elevation changes which result from ice dynamics and suggest progressive dynamic thickening in the southwest, and dynamic thinning in the west and northwest sectors of the ice sheet: glacier slowdown and speed-up has been observed across these regions, respectively. The majority of future ice losses from Greenland will be atmospherically driven (Golledge et al., 2019); our results suggest that CryoSat-2 can contribute towards understanding changes in Greenland which arise due to its meteorology.

References

Andrews, L. C., Catania, G. A., Hoffman, M. J., Gulley, J. D., Lüthi, M. P., Ryser, C., Hawley, R. L., and Neumann, T. A. (2014). Direct observations of evolving subglacial drainage beneath the Greenland Ice Sheet. *Nature*, 514:80. 98

Arthern, R. J., Vaughan, D. G., Rankin, A. M., Mulvaney, R., and Thomas, E. R. (2010). In situ measurements of Antarctic snow compaction compared with predictions of models. *Journal of Geophysical Research: Earth Surface*, 115(F3). 102

Bevis, M., Harig, C., Khan, S. A., Brown, A., Simons, F. J., Willis, M., Fettweis, X., van den Broeke, M. R., Madsen, F. B., Kendrick, E., Caccamise, D. J., van Dam, T., Knudsen, P., and Nylen, T. (2019). Accelerating changes in ice mass within Greenland, and the ice sheet's sensitivity to atmospheric forcing. *Proceedings of the National Academy of Sciences*, page 201806562. 98, 103, 105

Bowling, J. S., Livingstone, S. J., Sole, A. J., and Chu, W. (2019). Distribution and dynamics of Greenland subglacial lakes. *Nature Communications*, 10(1):2810. 98

Catania, G. A. and Neumann, T. A. (2010). Persistent englacial drainage features in the Greenland Ice Sheet. *Geophysical Research Letters*, 37(2). 98

Das, S. B., Joughin, I., Behn, M. D., Howat, I. M., King, M. A., Lizarralde, D., and Bhatia, M. P. (2008). Fracture propagation to the base of the Greenland Ice Sheet during supraglacial lake drainage. *Science*, 320(5877):778. 98

Davis, C. H. (1997). A robust threshold retracking algorithm for measuring ice-sheet surface elevation change from satellite radar altimeters. *IEEE Transactions on Geoscience and Remote Sensing*, 35(4):974–979. 100

Davis, C. H. and Ferguson, A. C. (2004). Elevation change of the Antarctic ice sheet, 1995-2000, from ERS-2 satellite radar altimetry. *IEEE Transactions on Geoscience and Remote Sensing*, 42(11):2437–2445. 100

Enderlin, E. M., Howat, I. M., Jeong, S., Noh, M.-J., Angelen, J. H., and Broeke, M. R. (2014). An improved mass budget for the Greenland Ice Sheet. *Geophysical Research Letters*, 41(3):866–872. 98, 99

ESA (2012). CryoSat-2 Product Handbook, ESRIN-ESA and Mullard Space Science Laboratory University College London, available at: http://emits.sso.esa.int/emits-doc/ESRIN/7158/CryoSat-PHB-17apr2012.pdf (last access: October 2017). 99, 100

Ettema, J., van den Broeke, M. R., van Meijgaard, E., van de Berg, W. J., Bamber, J. L., Box, J. E., and Bales, R. C. (2009). Higher surface mass balance of the Greenland ice sheet revealed by high-resolution climate modeling. *Geophysical Research Letters*, 36(12). 98

Fettweis, X., Box, J. E., Agosta, C., Amory, C., Kittel, C., Lang, C., van As, D., Machguth, H., and Gallée, H. (2017). Reconstructions of the 1900–2015 Greenland ice sheet surface mass balance using the regional climate MAR model. *The Cryosphere*, 11(2):1015–1033. 98

Fettweis, X., Franco, B., Tedesco, M., van Angelen, J. H., Lenaerts, J. T. M., van den Broeke, M. R., and Galllée, H. (2013a). Estimating the Greenland ice sheet surface mass balance contribution to future sea level rise using the regional atmospheric climate model MAR. *The Cryosphere*, 7(2):469–489. 98

Fettweis, X., Hanna, E., Lang, C., Belleflamme, A., Erpicum, M., and Gallée, H. (2013b). Brief communication: Important role of the mid-tropospheric atmospheric circulation in the recent surface melt increase over the Greenland ice sheet. *The Cryosphere*, 7(1):241–248. 98, 105

Flament, T. and Rémy, F. (2012). Dynamic thinning of Antarctic glaciers from along-track repeat radar altimetry. *Journal of Glaciology*, 58(211):830–840. 99

Forsberg, R., Sørensen, L., and Simonsen, S. (2017). Greenland and Antarctica Ice Sheet mass changes and effects on global sea level. *Surveys in Geophysics*, 38(1):89–104. 98

Golledge, N. R., Keller, E. D., Gomez, N., Naughten, K. A., Bernales, J., Trusel, L. D., and Edwards, T. L. (2019). Global environmental consequences of twenty-first-century ice-sheet melt. *Nature*, 566(7742):65–72. 98, 111

Gray, L., Burgess, D., Copland, L., Langley, K., Gogineni, P., Paden, J., Leuschen, C., van As, D., Fausto, R., Joughin, I., and Smith, B. (2019). Measuring height change around the periphery of the Greenland Ice Sheet with radar altimetry. *Frontiers in Earth Science*, 7(146). 98, 110

Hanna, E., Fettweis, X., Mernild, S. H., Cappelen, J., Ribergaard, M. H., Shuman, C. A., Steffen, K., Wood, L., and Mote, T. L. (2014). Atmospheric and oceanic climate forcing of the exceptional Greenland ice sheet surface melt in summer 2012. *International Journal of Climatology*, 34(4):1022–1037. 103, 105

Hanna, E., Mernild, S. H., Cappelen, J., and Steffen, K. (2012). Recent warming in Greenland in a long-term instrumental (1881–2012) climatic context: I. Evaluation of surface air temperature records. *Environmental Research Letters*, 7(4):045404. 98

Helm, V., Humbert, A., and Miller, H. (2014). Elevation and elevation change of Greenland and Antarctica derived from CryoSat-2. *The Cryosphere*, 8(4):1539–1559. 98

Joughin, I., Smith, B. E., Shean, D. E., and Floricioiu, D. (2014). Brief communication: Further summer speedup of Jakobshavn Isbræ. *The Cryosphere*, 8(1):209–214. 108, 110

Kehrl, L. M., Joughin, I., Shean, D. E., Floricioiu, D., and Krieger, L. (2017). Seasonal and interannual variabilities in terminus position, glacier velocity, and surface elevation at Helheim and Kangerlussuaq Glaciers from 2008 to 2016. *Journal of Geophysical Research: Earth Surface*, 122(9):1635–1652. 108

Khan, S. A., Kjær, K. H., Bevis, M., Bamber, J. L., Wahr, J., Kjeldsen, K. K., Bjørk, A. A., Korsgaard, N. J., Stearns, L. A., van den Broeke, M. R., Liu, L., Larsen, N. K., and Muresan, I. S. (2014). Sustained mass loss of the northeast Greenland Ice Sheet triggered by regional warming. *Nature Climate Change*, 4:292. 98, 109

Kuipers Munneke, P., Ligtenberg, S. R. M., Noël, B. P. Y., Howat, I. M., Box, J. E., Mosley-Thompson, E., McConnell, J. R., Steffen, K., Harper, J. T., Das, S. B., and van den Broeke, M. R. (2015). Elevation change of the Greenland Ice Sheet due to surface mass balance and firn processes, 1960–2014. *The Cryosphere*, 9(6):2009–2025. 98, 102, 103, 110

Larsen, S. H., Khan, S. A., Ahlstrøm, A. P., Hvidberg, C. S., Willis, M. J., and Andersen, S. B. (2016). Increased mass loss and asynchronous behavior of marine-terminating outlet glaciers at Upernavik Isstrøm, NW Greenland. *Journal of Geophysical Research: Earth Surface*, 121(2):241–256. 108

Leeson, A. A., Eastoe, E., and Fettweis, X. (2018). Extreme temperature events on Greenland in observations and the MAR regional climate model. *The Cryosphere*, 12(3):1091–1102. 98, 102

Leeson, A. A., Shepherd, A., Briggs, K., Howat, I., Fettweis, X., Morlighem, M., and Rignot, E. (2014). Supraglacial lakes on the Greenland ice sheet advance inland under warming climate. *Nature Climate Change*, 5:51. 98

Lemos, A., Shepherd, A., McMillan, M., Hogg, A. E., Hatton, E., and Joughin, I. (2018). Ice velocity of Jakobshavn Isbræ, Petermann Glacier, Nioghalvfjerdsfjorden, and Zachariæ isstrøm, 2015–2017, from Sentinel 1-a/b SAR imagery. *The Cryosphere*, 12(6):2087–2097. 108

Ligtenberg, S., Helsen, M. M., and van den Broeke, M. R. (2011). An improved semi-empirical model for the densification of Antarctic firn. *The Cryosphere*, 5(4):809–819. 99, 102

Ligtenberg, S., Kuipers Munneke, P., Noël, B. P. Y., and van den Broeke, M. R. (2018). Brief communication: Improved simulation of the present-day Greenland firn layer (1960–2016). *The Cryosphere*, 12(5):1643–1649. 98, 99, 102

McMillan, M., Leeson, A., Shepherd, A., Briggs, K., Armitage, T. W. K., Hogg, A., Kuipers Munneke, P., van den Broeke, M., Noël, B., van de Berg, W. J., Ligtenberg, S., Horwath, M., Groh, A., Muir, A., and Gilbert, L. (2016). A high-resolution record of Greenland mass balance. *Geophysical Research Letters*, 43(13):7002–7010. 98, 99, 100, 102, 103, 105

McMillan, M., Shepherd, A., Sundal, A., Briggs, K., Muir, A., Ridout, A., Hogg, A., and Wingham, D. (2014). Increased ice losses from Antarctica detected by CryoSat-2. *Geophysical Research Letters*, 41(11):3899–3905. 100

Mohr, J. J., Reeh, N., and Madsen, S. N. (1998). Three-dimensional glacial flow and surface elevation measured with radar interferometry. *Nature*, 391(6664):273–276. 108

Moon, T., Joughin, I., and Smith, B. (2015). Seasonal to multiyear variability of glacier surface velocity, terminus position, and sea ice/ice mélange in northwest Greenland. *Journal of Geophysical Research: Earth Surface*, 120(5):818–833. 109

Mouginot, J., Rignot, E., Bjørk, A. A., van den Broeke, M., Millan, R., Morlighem, M., Noël, B., Scheuchl, B., and Wood, M. (2019). Forty-six years of Greenland Ice Sheet mass balance from 1972 to 2018. *Proceedings of the National Academy of Sciences*, page 201904242. 98

Mouginot, J., Rignot, E., Scheuchl, B., Fenty, I., Khazendar, A., Morlighem, M., Buzzi, A., and Paden, J. (2015). Fast retreat of Zachariæ Isstrøm, northeast Greenland. *Science*, 350(6266):1357–1361. 99, 108

Nghiem, S. V., Hall, D. K., Mote, T. L., Tedesco, M., Albert, M. R., Keegan, K., Shuman, C. A., DiGirolamo, N. E., and Neumann, G. (2012). The extreme melt across the Greenland ice sheet in 2012. *Geophysical Research Letters*, 39(20). 100, 103, 105

Nilsson, J., Gardner, A., Sandberg Sørensen, L., and Forsberg, R. (2016). Improved retrieval of land ice topography from CryoSat-2 data and its impact for volume-change estimation of the Greenland ice sheet. *The Cryosphere*, 10(6):2953–2969. 98, 103

Nilsson, J., Vallelonga, P., Simonsen, S. B., Sørensen, L. S., Forsberg, R., Dahl-Jensen, D., Hirabayashi, M., Goto-Azuma, K., Hvidberg, C. S., Kjaer, H. A., and Satow, K. (2015). Greenland 2012 melt event effects on CryoSat-2 radar altimetry. *Geophysical Research Letters*, 42(10):3919–3926. 100

Noël, B., van de Berg, W. J., van Wessem, J. M., van Meijgaard, E., van As, D., Lenaerts, J. T. M., Lhermitte, S., Kuipers Munneke, P., Smeets, C. J. P. P., van Ulft, L. H., van de Wal, R. S. W., and van den Broeke, M. R. (2018). Modelling the climate and surface mass balance of polar ice sheets using RACMO2 – Part 1: Greenland (1958–2016). *The Cryosphere*, 12(3):811–831. 98, 99, 102, 110

Rignot, E., Velicogna, I., van den Broeke, M. R., Monaghan, A., and Lenaerts, J. T. M. (2011). Acceleration of the contribution of the Greenland and Antarctic ice sheets to sea level rise. *Geophysical Research Letters*, 38(5). 99

Sandberg Sørensen, L., Simonsen, S. B., Forsberg, R., Khvorostovsky, K., Meister, R., and Engdahl, M. E. (2018). 25 years of elevation changes of the Greenland ice sheet from ERS, Envisat, and CryoSat-2 radar altimetry. *Earth and Planetary Science Letters*, 495:234–241. 98, 103

Shepherd, A., Ivins, E. R., A, G., Barletta, V. R., Bentley, M. J., Bettadpur, S., Briggs, K. H., Bromwich, D. H., Forsberg, R., Galin, N., Horwath, M., Jacobs, S., Joughin, I., King, M. A., Lenaerts, J. T. M., Li, J., Ligtenberg, S. R. M., Luckman, A., Luthcke, S. B., McMillan, M., Meister, R., Milne, G., Mouginot, J., Muir, A., Nicolas, J. P., Paden, J., Payne, A. J., Pritchard, H., Rignot, E., Rott, H., Sørensen, L. S., Scambos, T. A., Scheuchl, B., Schrama, E. J. O., Smith, B., Sundal, A. V., van Angelen, J. H., van de Berg, W. J., van den Broeke, M. R., Vaughan, D. G., Velicogna, I., Wahr, J., Whitehouse, P. L., Wingham, D. J., Yi, D., Young, D., and Zwally, H. J. (2012). A reconciled estimate of ice-sheet mass balance. *Science*, 338(6111):1183. 98, 99

Simonsen, S. B. and Sørensen, L. S. (2017). Implications of changing scattering properties on Greenland ice sheet volume change from CryoSat-2 altimetry. *Remote Sensing of Environment*, 190:207–216. 98, 99, 100, 103

Sørensen, L. S., Simonsen, S. B., Nielsen, K., Lucas-Picher, P., Spada, G., Adalgeirsdottir, G., Forsberg, R., and Hvidberg, C. S. (2011). Mass balance of the Greenland ice sheet (2003–2008) from ICESat data – the impact of interpolation, sampling and firn density. *The Cryosphere*, 5(1):173–186. 99

Studinger, M. (2014). Icebridge ATM L4 surface elevation rate of change, Version 1, National Snow and Ice Data Center, Boulder, Colorado, USA, available at: https://nsidc.org/icebridge/portal/ (last access January 2019). 100

Tedesco, M., Fettweis, X., Mote, T., Wahr, J., Alexander, P., Box, J. E., and Wouters, B. (2013). Evidence and analysis of 2012 Greenland records from spaceborne observations, a regional climate model and reanalysis data. *The Cryosphere*, 7(2):615–630. 98, 105

Tedesco, M., Mote, T., Fettweis, X., Hanna, E., Jeyaratnam, J., Booth, J. F., Datta, R., and Briggs, K. (2016). Arctic cut-off high drives the poleward shift of a new Greenland melting record. *Nature Communications*, 7:11723. 105

Tedstone, A. J., Nienow, P. W., Gourmelen, N., Dehecq, A., Goldberg, D., and Hanna, E. (2015). Decadal slowdown of a land-terminating sector of the Greenland Ice Sheet despite warming. *Nature*, 526:692. 108, 109

Thomas, R., Frederick, E., Krabill, W., Manizade, S., and Martin, C. (2006). Progressive increase in ice loss from Greenland. *Geophysical Research Letters*, 33(10). 99

Trusel, L. D., Das, S. B., Osman, M. B., Evans, M. J., Smith, B. E., Fettweis, X., McConnell, J. R., Noël, B. P. Y., and van den Broeke, M. R. (2018). Nonlinear rise in Greenland runoff in response to post-industrial Arctic warming. *Nature*, 564(7734):104–108. 98

van Angelen, J. H., van den Broeke, M. R., Wouters, B., and Lenaerts, J. T. M. (2014). Contemporary (1960–2012) evolution of the climate and surface mass balance of the Greenland Ice Sheet. *Surveys in Geophysics*, 35(5):1155–1174. 98, 103, 105

van den Broeke, M., Bamber, J., Ettema, J., Rignot, E., Schrama, E., van de Berg, W. J., van Meijgaard, E., Velicogna, I., and Wouters, B. (2009). Partitioning recent Greenland mass loss. *Science*, 326(5955):984–6. 99

van den Broeke, M., Enderlin, E. M., Howat, I. M., Kuipers Munneke, P., Noël, B. P. Y., van de Berg, W. J., van Meijgaard, E., and Wouters, B. (2016). On the recent contribution of the Greenland Ice Sheet to sea level change. *The Cryosphere*, 10(5):1933–1946. 98, 99, 103

Wingham, D. J., Francis, C. R., Baker, S., Bouzinac, C., Brockley, D., Cullen, R., de Chateau-Thierry, P., Laxon, S. W., Mallow, U., Mavrocordatos, C., Phalippou, L., Ratier, G., Rey, L., Rostan, F., Viau, P., and Wallis, D. W. (2006). CryoSat: A mission to determine the fluctuations in Earth's land and marine ice fields. *Advances in Space Research*, 37(4):841–871. 100

Zwally, H. J., Abdalati, W., Herring, T., Larson, K., Saba, J., and Steffen, K. (2002). Surface melt-induced acceleration of Greenland Ice Sheet flow. *Science*, 297(5579):218–222. 98

Zwally, H. J., Giovinetto, M. B., Beckley, M. A., and Saba, J. J. L. (2012). Antarctic and Greenland drainage systems. xvi, 101, 105

Chapter 5

Discussion and conclusions

This thesis aimed to develop novel methods in the processing of satellite radar altimetry data to improve the accuracy of elevation and elevation change retrievals over Earth's ice sheets. In the preceding chapters, I have met this aim using data acquired by the CryoSat-2 satellite radar altimeter mission to develop improvements in the retrieval of ice surface elevation and elevation change across the Antarctic and Greenland ice sheets, respectively. Firstly, I created a model of the surface height of the Antarctic Ice Sheet by applying a model fit to 6 years of CryoSat-2 measurements, developing a contemporary Digital Elevation Model (DEM) of Antarctica's grounded ice sheet and floating ice shelves (Chapter 2) — with improved data coverage (three times more measurements than a previous CryoSat-2 DEM (Helm et al., 2014)), and an overall accuracy comparable to or better than other publicly available DEMs derived from satellite radar altimeters. Secondly, I developed a new technique to retrieve estimates of the depth distribution of radar backscatter from CryoSat-2 altimeter waveforms using a backscatter model. I applied this model to estimate spatial and temporal variations in radar backscatter across the interior of the Greenland Ice Sheet (Chapter 3). This model includes, for the first time, an explicit measure of radar penetration depth. I then used this information to correct for artefacts in elevation trends from CryoSat-2 pulse-limited altimetry, resulting from an episodic melt event which had reset the radar scattering horizon. Finally, I measured seasonal elevation changes in the ablation zone of the Greenland Ice Sheet, driven by melting and snowfall accumulation, using CryoSat-2 observations and regional climate model simulations (Chapter 4). In this final chapter I will outline how this thesis has met the original aims and research

objectives, firstly by summarising the key scientific findings from each chapter, before discussing areas for future work which have emerged from these results.

5.1 Summary of principal findings

In the following section, I summarise the novel datasets and methodological advances, based upon the processing of CryoSat-2 satellite radar altimetry data, developed in this thesis: a new Digital Elevation Model of Antarctica, a seven year time series of variability in radar backscatter over the Greenland Ice Sheet, an empirical correction to altimeter elevation trends to account for spatiotemporal changes in radar penetration depth, and the derivation of seasonal elevation trends in the ablation zone of the Greenland Ice Sheet.

5.1.1 A new Digital Elevation Model of Antarctica

In Chapter 2, I created a new Digital Elevation Model (DEM) of Antarctica. Accurate and contemporary DEMs are necessary as a boundary condition for ice sheet numerical modelling (e.g. (Cornford et al., 2015; Ritz et al., 2015)), and to distinguish between phase differences caused by topography and ice motion when measuring ice velocity using interferometric synthetic aperture radar (e.g. (Mouginot et al., 2012; Rignot et al., 2011)). In addition, DEMs can be used to delineate drainage basins (e.g.(Bamber et al., 2009)) or to estimate ice thickness at the grounding line when combined with other data (e.g. (Helsen et al., 2008; Rignot et al., 2008)). Applying a model fit to 6-years of CryoSat-2 data between 2010 and 2016, I developed a DEM posted at a spatial resolution of 1 km, with comprehensive data coverage — 94 % of the grounded ice sheet and 98 % of the floating ice shelves (Chapter 2, Figure 2.4) — a significant improvement over previous DEMs derived from altimetry (Bamber et al., 2009; Helm et al., 2014). To evaluate the accuracy of the DEM, I compared 2.7 x 10^5 individual DEM grid cells containing CryoSat-2 data to contemporaneous and independent measurements acquired by airborne laser altimeters during NASA's Operation IceBridge survey (Krabill, 2016). From this comparison there was good agreement between the two datasets (Chapter 2, Figure 2.7): the median and root mean square difference between the DEM and 2.3 x 10^7 airborne laser altimeter measurements were -0.30 m and 13.50 m, respectively. The largest differences were found to occur in areas of high slope

and where CryoSat-2 operates in low resolution mode: in these regions the altimeter ranges to the peaks of undulating terrain and undersamples troughs (Chapter 2, Figure 2.9). Taking into account the slope-dependent uncertainties and the wider distribution of slopes, the average accuracy was estimated to be 9.5 m. In addition, I compared the accuracy of the new CryoSat-2 DEM to three other publicly available Antarctic DEMs (Bamber et al., 2009; Fretwell et al., 2013; Helm et al., 2014) using the same reference IceBridge dataset. From this comparison I found the accuracy of the DEM to be comparable to, or better than the previously published DEMs (Chapter 2, Figure 2.8 and Figure 2.10).

5.1.2 Spatial and temporal variations in radar backscatter and penetration depth over the Greenland Ice Sheet

Over ice, the shape of altimeter echoes is complicated by ice sheet topography and the penetration of the Ku band radar pulse several metres beyond the snow surface (Armitage et al., 2014; Arthern et al., 2001; Ridley and Partington, 1988). The depth of radar penetration depends on the scattering characteristics of the snowpack (Matzler, 1996), which exhibit spatial and temporal variability (Davis and Zwally, 1993). In order to improve the accuracy of spatial and temporal changes in the surface elevation of Earth's ice sheets derived from satellite radar altimetry, it is necessary to understand and mitigate these effects. In Chapter 3, I developed a technique to estimate the depth-distribution of radar backscatter from CryoSat-2 low-resolution mode echoes using a radar backscatter model. The model allows the separation of the relative surface and volume backscattering contributions and, for the first time, the derivation of the effective penetration depth of the radar echoes into the snowpack (Chapter 3). Using this model, I charted spatial and temporal variations in surface and volume backscatter and effective radar penetration depth (Chapter 3, Figure 3.2) over the interior of the Greenland Ice Sheet between 2011 and 2017: during this period anomalously high temperatures induced surface melting over $\sim$ 99 % of the ice sheet surface area in the summer of 2012 (Fettweis et al., 2013; Nghiem et al., 2012), extending inland to regions which had not previously seen melting during the satellite era (Mote, 2007). The percolation and refreezing of surface meltwater reset the radar scattering horizon, inducing spurious elevation signals in uncorrected CryoSat-2 satellite radar altimeter data (Nilsson et al., 2015). Using the waveform deconvolution technique described in

Chapter 3 I demonstrated a clear shift in radar backscatter from a situation dominated by volume scattering to scattering from near the snow surface (Chapter 3, Figure 3.1) as a consequence of the melt event. Between the months immediately before and after the melt event, there was a two-fold increase in the proportion of backscattered power returning from the ice sheet surface across the ice sheet interior, on average (Chapter 3, Figure 3.2). In regions above 2000 m in altitude, I estimated that the radar penetration depth decreased from 3.79 ± 1.12 m to 1.45 ± 0.94 m, on average, between the months before and after the formation of the new scattering horizon in July 2012, respectively. The reduction in penetration depth was greater in high altitude areas which melted for the first time in the satellite era: in the region above 2800 m.a.s.l. the penetration depth decreased by 3.21 ± 1.16 m. Following the formation of the new radar scattering horizon after the 2012 melt event, backscattered power increasingly shifts to the volume component during subsequent years (Chapter 3, Figure 3.1 and Figure 3.2): by the end of 2017 the Ku band radar scattering horizon has lowered to a depth of 3.28 ± 1.13 m on average, to within approximately 0.5 m of that recorded before the summer of 2012.

5.1.3 Compensating for changes in penetration depth in satellite altimeter elevation trends

Time series of ice sheet elevation change computed using conventionally retracked echoes have exhibited seasonal cycles (Davis and Ferguson, 2004; Wingham et al., 1998) and episodic shifts (Nilsson et al., 2015) that track changes in the echo properties, which have been interpreted as owing to changes in the snowpack scattering properties (McMillan et al., 2016; Nilsson et al., 2016; Sandberg Sørensen et al., 2018; Simonsen and Sørensen, 2017). In Chapter 3 I applied an empirical correction based upon the ratio between changes in penetration depth and elevation (Chapter 3, Equation 3.6 and Figure 3.3). This correction allows, for the first time, elevation trends derived from satellite radar altimetry to be compensated for fluctuations in volume scatter with direct knowledge of the penetration depth. In order to investigate the effects of variable radar penetration on the two main classes of retracker most commonly used in the literature, I used measurements of ice sheet surface elevation determine using both a physically- (CFI) and empirically-based threshold offset center of gravity (TCOG) retracker. I showed that changes in radar penetration depth are correlated with changes in surface elevation from retracked CryoSat-2 echoes, with 21 and 6 cm

of elevation change occurring per metre variation in penetration depth for the CFI and TCOG retrackers, respectively. In both cases, correcting for correlated changes in radar penetration depth reduced the spurious step-like increase in elevation change associated with widespread surface melting in the summer of 2012 (Chapter 3, Figure 3.4) and the positive bias in elevation trends it caused (Chapter 3, Figure 3.5). When comparing CryoSat-2 elevation trends compensated for changes in penetration depth in the interior of the Greenland Ice Sheet with independent airborne laser altimeter measurements, the bias was reduced by up to 14 cm/yr. I found that elevation trends from CryoSat-2 data processed with the empirically-based TCOG retracker are much less affected by changes in penetration depth than those processed with the physically-based CFI retracker, with typically 6 to 21 cm of elevation change occurring per metre variation in penetration depth for each retracker, respectively. In addition, I showed that over longer time periods (greater than 4 years), the correction diminishes in importance as the impact of the singular melt event on derived elevation trends is reduced.

5.1.4 Seasonal elevation changes in the ablation zone of the Greenland Ice Sheet

In Chapter 4, I separated long-term and seasonal elevation changes in the ablation zone of the Greenland Ice Sheet during the period 2011-2017, and compared them to output from a semi-empirical firn densification model (IMAU-FDM) (Ligtenberg et al., 2011, 2018) which describes surface elevation changes due to firn and surface mass balance processes alone (e.g. (Kuipers Munneke et al., 2015)). Overall, I found broad agreement between both datasets in reproducing the spatial pattern of elevation change (Chapter 4, Figure 4.1). The most notable differences arise at several marine-terminating glaciers that are known to be significantly out of balance — for example Jakobshavn Isbræ (Joughin et al., 2014; Lemos et al., 2018), Zachariae Isstrøm (Mouginot et al., 2015), Kangerlussuaq (Kehrl et al., 2017), and Upernavik Isstrøm (Larsen et al., 2016) — where the elevation change associated with ice dynamical imbalance is not captured by the firn models. To assess the accuracy of the long-term elevation trends derived from CryoSat-2, I compared them to 11404 contemporaneous and independent measurements derived from Operation IceBridge laser altimetry (Studinger, 2014): the mean and standard deviation of the differences (CryoSat-2 — IceBridge) were 11 cm/yr and 59 cm/yr, respectively.

I also determined the monthly evolution of ice surface height from CryoSat-2 altimetry and IMAU-FDM in the Greenland Ice Sheet ablation zone (Chapter 4, Figure 4.2), and found that both time series were highly correlated ($R = 0.98$) and consistent in describing height change. In addition, I derived summer and winter rates of ablation zone surface elevation change from both datasets (Chapter 4, Figure 4.3), finding good agreement (median difference -0.06 m/yr, root-mean square (RMS) difference 0.44 m/yr). When the seasonal elevation trends are split further into the principal ice sheet drainage basins (Chapter 4, Figure 4.3), the agreement is reduced but typically the data sets differ by less than 1 m/yr (RMS = 1.06 m/yr). Both datasets are consistent in capturing the interannual variability in seasonal elevation trends (Chapter 4, Figure 4.4): the highest rate of summer thinning across the ablation zone occurred in the summer of 2012 (-5.21 ± 0.33 m/yr from CryoSat-2) and relate to an exceptionally warm summer (Hanna et al., 2014; Nghiem et al., 2012; Tedesco et al., 2013). Reduced thinning in the following summer of 2013 (-2.59 ± 0.61 m/yr from CryoSat-2) reflects an abrupt change in atmospheric circulation favouring cooler conditions (Bevis et al., 2019). Finally, I examined the differences between CryoSat-2 and FDM monthly time series of elevation change (Chapter 4, Figure 4.5): these were consistent with current understanding of the evolution ice dynamical imbalance within the Greenland ablation zone (e.g. (Khan et al., 2014; Moon et al., 2015; Sundal et al., 2011; Tedstone et al., 2015).

5.2 Synthesis of principal findings

In this thesis, I have developed novel methods and datasets based upon the processing of CryoSat-2 data, in order to improve the understanding of retrieving elevation and elevation trends over Earth's ice sheets. Together, these results can be used to better inform estimates of the ice sheet contribution to sea level rise, and the climate models on which sea level projections are based.

In Chapter 2, I created an elevation model of Antarctica using heights derived from fitting a plane-fit model to CryoSat-2 elevation measurements. Accurate and up-to-date DEMs are important datasets needed as a boundary condition for numerical ice

dynamic models (e.g. (Cornford et al., 2013; Nias et al., 2018; Pattyn et al., 2013)), and to compute grounding line thickness necessary for estimates of ice sheet mass balance using the mass budget method (e.g. (Mouginot et al., 2019; Rignot et al., 2019). Similarly, in climate models (e.g. (Agosta et al., 2019; van Wessem et al., 2018)), high resolution topography is required to accurately simulate katabatic winds and orographically forced precipitation. The DEM described in Chapter 2 can be implemented in these models to provide a better and current description of ice sheet topography — particularly at the ice sheet margins — and improve simulations of ice sheet meteorology and the ice dynamical response to future climate change. Improved and updated knowledge of ice sheet topography can also be used to update slope models (e.g. Figure 2.5) used to correct radar altimeter measurements (e.g. (Roemer et al., 2007)), and open loop tracking algorithms which position the altimeter range window using a priori knowledge of the surface height. In this thesis, I demonstrate the plane-fit model used to calculate ice sheet height in Chapter 2 is also well suited for computing elevation trends; in Chapters 3 and 4, I utilised the same model to map the long-term and seasonal height change of the Greenland Ice Sheet, respectively, and showed that these trends agree well with independent measurements.

Temporal fluctuations in the radar backscattering properties of the ice sheets induce spurious fluctuations in range which can be widespread and episodic (Nilsson et al., 2015) and correlate over seasonal and interannual timescales (Davis and Ferguson, 2004; Khvorostovsky, 2012). Even small signals can potentially have a large impact on spatially aggregated estimates of ice sheet mass balance when converted from volume changes, owing to the large length scales over which they are integrated. Compensating satellite radar altimeter derived elevation trends for fluctuations in radar penetration depth using the methods of Chapter 3 provide a means of improving the certainty of estimates of ice sheet mass balance. In turn, these improved assessments of ice sheet mass balance can provide a more accurate means of evaluating the reliability of ice sheet simulations (e.g. Figure 5.1) (Slater and Shepherd, 2018).

Seasonal elevation changes in the ablation zone of the Greenland Ice Sheet, described in Chapter 4, provide a new observational dataset which can be used to validate regional climate models. Such an exercise can provide increased certainty in simulations of ice

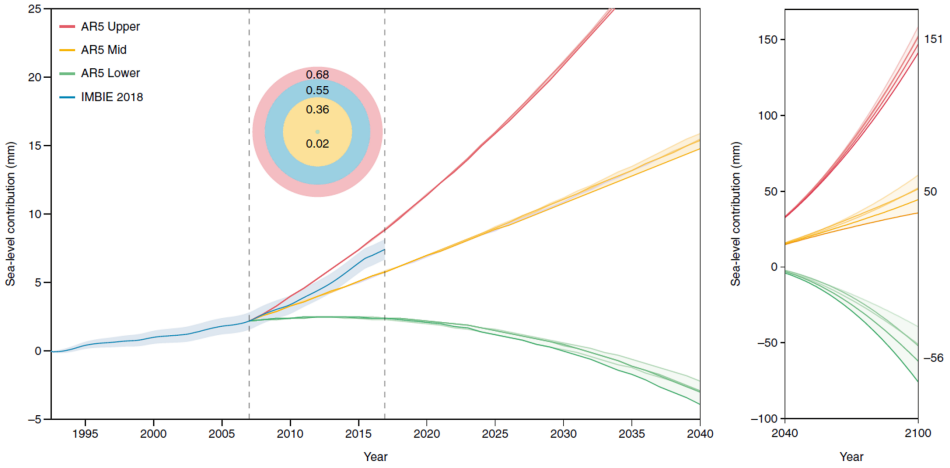

Figure 5.1: The global sea level contribution from Antarctica according to satellite observations (The IMBIE Team, 2018) (blue) and IPCC AR5 (Church et al., 2013) upper (red), mid (yellow) and lower (green) projections is shown from 1992-2040 (left) and 2040-2100 (right; values on the right hand side indicate the average sea level contribution predicted at 2100). The circle plot (inset) shows the rate of sea level rise (in mm/yr) during the overlap period 2007-2017 (vertical dashed lines). Extracted from (Slater and Shepherd, 2018).

sheet meteorology used to project the ice sheet response to future changes in atmospheric forcing . In addition to long term trends, the seasonal elevation trends derived in Chapter 4 can be used to validate rates of ablation and accumulation from regional climate models and evaluate the model's ability to represent the physical mechanisms responsible for ice sheet mass change. Furthermore, the techniques outlined within each chapter are complementary: echo deconvolutions can be used to (1) correct these seasonal elevation trends derived from radar altimetry for fluctuations in radar backscatter (of particular benefit in winter when snow accumulates on the ice sheet) and (2) adjust ice sheet DEMs derived from radar altimeters to the ice sheet surface using knowledge of the depth of the dominant radar scattering horizon.

The work described in Chapters 2, 3 and 4 deliver improvements in the understanding of the retrieval of elevation and elevation change over the Antarctica and Greenland from radar altimetry. Satellite altimeter measurements of ice height and its temporal

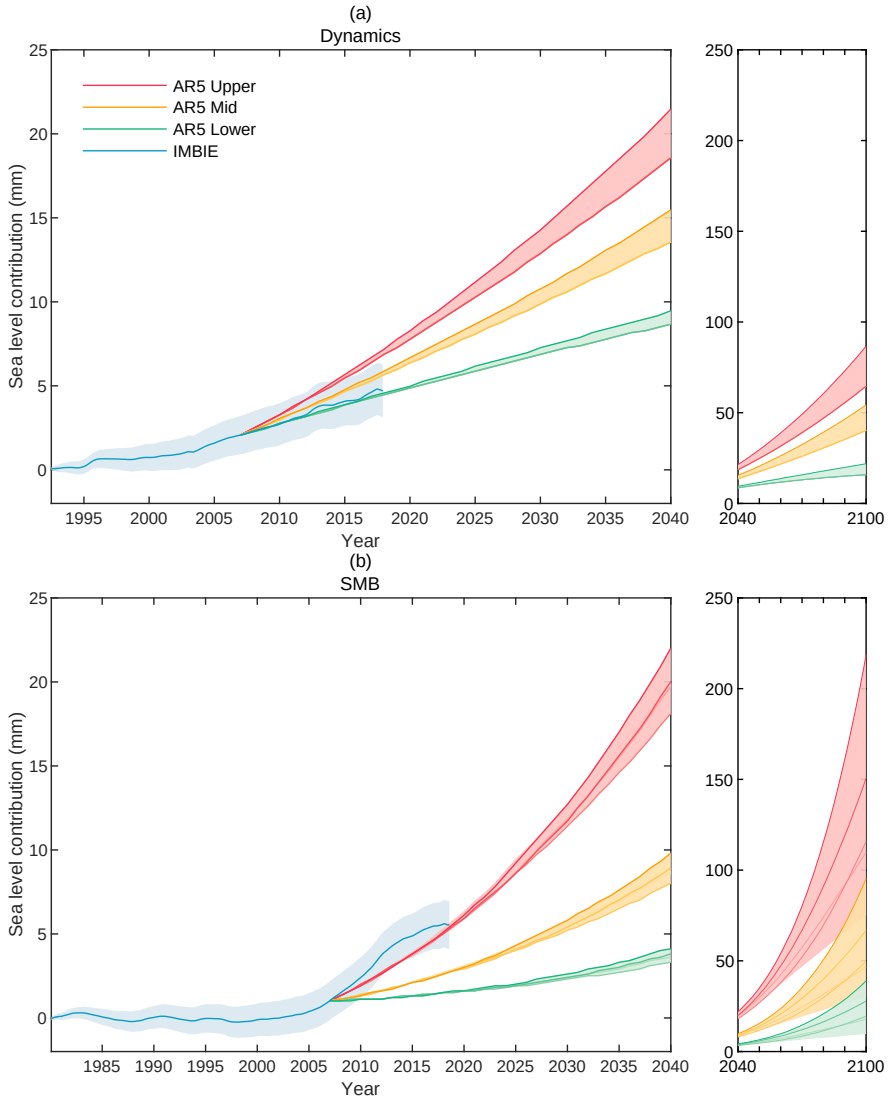

Figure 5.2: The global sea level contribution from Greenland (a) ice dynamics (b) surface mass balance according to satellite observations (blue) and IPCC AR5 (Church et al., 2013) upper (red), mid (yellow) and lowe (green) projections is shown from 1992-2040 (left) and 2040-2100 (right; values on the right hand side indicate the average sea level contribution predicted at 2100).

evolution are key glaciological parameters which, over the past 25 years, have identified areas of dynamic imbalance (e.g. (Pritchard et al., 2009; Wingham et al., 1998)) and charted ice sheet mass loss (e.g. (McMillan et al., 2016, 2014; Schröder et al., 2019; Shepherd et al., 2019, 2012; The IMBIE Team, 2018)). The potential improvements in the retrieval of ice sheet elevation and elevation change from radar altimeters described in this thesis can be used to improve estimates of ice sheet mass balance through (1) the application of new DEMs to the mass budget method, regional climate models and altimeter slope corrections, (2) compensating elevation trends for variations in penetration depth and (3) validating regional climate models used to simulate ice sheet surface mass balance.

Satellite altimeter observations of height and height change can be used to constrain numerical simulations of how the Antarctic and Greenland ice sheets respond to climate change, as a boundary condition for ice dynamic (e.g. (Cornford et al., 2015)) and regional climate models (e.g. (Noël et al., 2018; van Wessem et al., 2018)) and to validate modelled sea level rise contributions (Shepherd and Nowicki, 2017; Slater and Shepherd, 2018) (Figure 5.1). Of the individual components contributing to rising sea levels, Earth's polar ice sheets are the largest sources of uncertainty in projections of future sea level rise (Church et al., 2013); improvements in these predictions are required to better inform policymakers considering appropriate climate policy and adaptations. In Greenland, for example (Figure 5.2), cumulative ice losses due to surface mass balance processes are tracking the upper range of climate warming scenarios, whilst losses due to ice discharge are tracking the lower range. Ongoing monitoring is required to establish whether these trajectories will be followed, and even greater sea level contributions are possible as regional climate and ice dynamic models are further improved; the results developed in this thesis can be used to help achieve this goal through the provision of updated boundary conditions (Chapter 2) and validation datasets (Chapter 4).

5.3 Recommendations for future work

In this section, I explore the ways in which the methods developed in this thesis can potentially be employed to derive new techniques and datasets which form the basis of future studies. Firstly, I consider the application of the techniques described in

Chapters 2 and 3 to other relevant locations and satellite altimeter missions. I then look at the potential of extending the methods devised in Chapter 4 to derive estimates of ice sheet ablation over the Greenland Ice Sheet.

5.3.1 A CryoSat-2 Digital Elevation Model of the Greenland Ice Sheet

In Chapter 2, I demonstrated the capability of applying a model-fit to radar altimeter time series to produce an accurate DEM of Antarctica with comprehensive spatial coverage. In the future, this approach can be employed to create a new high spatial resolution (1 km) DEM of the Greenland Ice Sheet from CryoSat-2 altimetry. In this section, I explore the potential of this approach by generating a preliminary DEM of the Greenland Ice Sheet following the same approach outlined in Chapter 2, from over 34 million CryoSat-2 measurements acquired between 2011 and 2017 (Figure 5.3). Posted

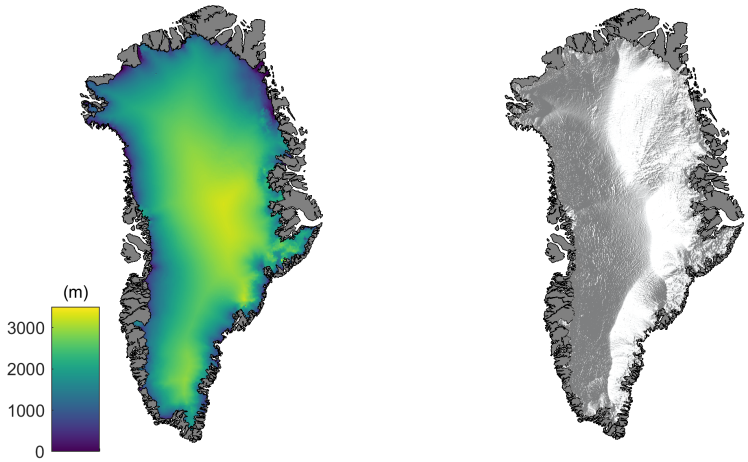

Figure 5.3: (left) A preliminary digital elevation model of Greenland derived from 7 years of CryoSat-2 radar altimetry data acquired between July 2010 and 2017, and (right) a shaded relief map of the elevation model.

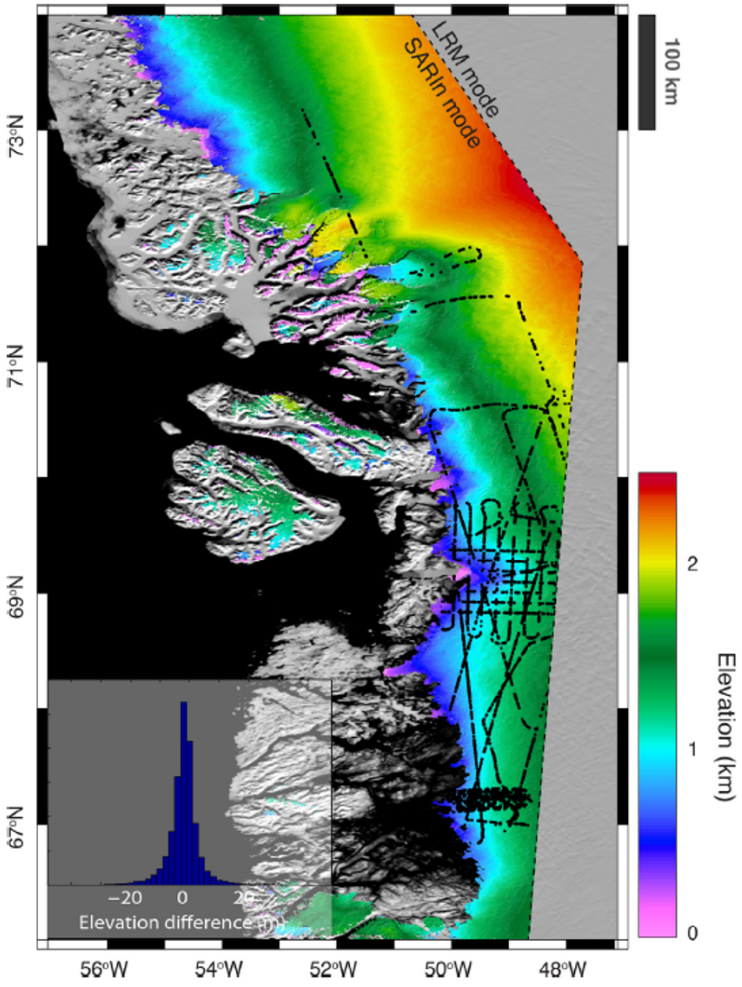

Figure 5.4: Elevation posted at 500 m resolution from swath interferometric processing of CryoSat-2 data. The inland limit of the swath elevation model corresponds to CryoSat-2's SARIn mode mask boundary (dashed line). Also shown are the locations of Operation IceBridge airborne laser altimeter measurements (black) used to validate the elevation model (inset). Extracted from (Gourmelen et al., 2018).

at a resolution of 1 km, this preliminary DEM observes 90 % of the ice sheet. As in Chapter 2, this DEM can be evaluated against contemporaneous Operation IceBridge airborne laser altimeter measurements in the future, and compared to other publicly available DEMs. Although not accounted for in these early results, episodic changes in snowpack scattering properties which occurred in Greenland over the course of the CryoSat-2 observation period (Nilsson et al., 2015) can be corrected for by utilising the echo deconvolution outlined in Chapter 3. Low resolution mode data from the ice sheet interior can also be combined swath interferometric data from CryoSat-2 (Gourmelen et al., 2018) (e.g. Figure 5.4) which provide even higher spatial resolution (500 m) in the ice sheet margins, and up to two orders of magnitude more elevation measurements than standard altimetry. Indeed, the model-fit approached utilised in this thesis can also be employed to other altimeter missions (e.g. Sentinel-3 (McMillan et al., 2019), IceSat-2 (Markus et al., 2017), AltiKa (Verron et al., 2015)); consideration of different operating frequencies (i.e. IceSat-2, AltiKa) can help understand their respective penetration depths, and characterise the uncertainties introduced by variable snow scattering characteristics.

5.3.2 Extension of echo deconvolution to Antarctica, SARIn echoes, and to data from other missions

In Chapter 3, I applied a numerical deconvolution technique to pulse-limited echoes in order to chart spatial and temporal changes in radar backscatter across the interior of the Greenland Ice Sheet. Although large-scale, episodic changes in the radar scattering horizon — as explored in Chapter 3 — have been limited to Greenland (Nilsson et al., 2015), short-period fluctuations in radar backscatter across the Antarctic Ice Sheet may influence altimeter-derived elevation trends (Arthern et al., 2001; Davis and Ferguson, 2004; McMillan et al., 2014; Wingham et al., 1998). In Chapter 3, I demonstrated that the echo deconvolution can be used to compensate for changes in penetration depth: in future this technique can be used to improve estimates of elevation change in the interior of the Antarctic Ice Sheet from radar altimetry (e.g. Figure 5.5). This is of particular importance in East Antarctica, where small elevation changes can have a relatively large effect on the spatially integrated mass balance. In addition, the echo deconvolution can be used to provide further insight into the nature of static crossover patterns in the interior of Antarctica brought about by wind-induced features of the

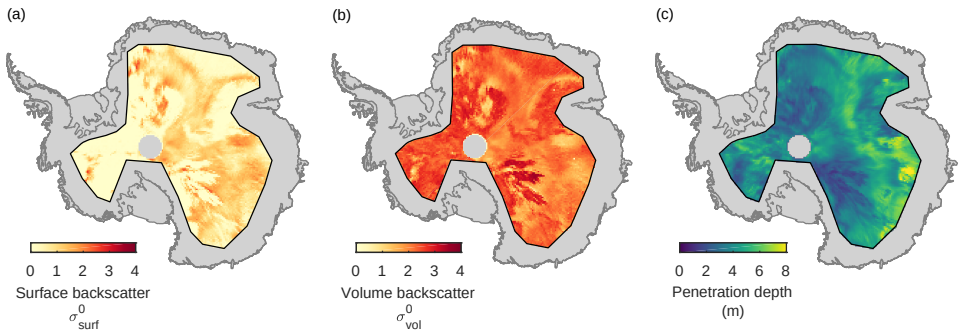

Figure 5.5: Preliminary results generated by applying the methods in Chapter 3 to the interior of the Antarctic Ice Sheet: average values of (a) surface backscatter coefficient, (b) volume backscatter coefficient and c) penetration depth during the period 2011-2016. In each plot the boundary between LRM and SARIn mode acquisitions is shown in black.

firn (Armitage et al., 2014).

In future, implementing the echo deconvolution within a Level 2 processor would allow fluctuations in penetration depth to be compensated for on an individual waveform basis, offering an improvement over the empirical approach employed in Chapter 3. A more sophisticated description of the surface response can be developed — using a radar backscatter model which accounts for the local surface topography, for example — to replace the empirical ocean waveform used in Chapter 3. In addition, a similar approach can be developed for CryoSat-2's SARIn mode: this would allow fluctuations in radar penetration depth to be accounted for in radar altimeter elevation trends in the ice sheet margins, where the strongest signals occur. Beyond CryoSat-2, similar backscatter models can be developed for other radar altimeters: such datasets would allow investigations in the differences between e.g. conventional pulse-limited and SAR altimeters (Sentinel-3 (McMillan et al., 2019)) and Ku and Ka operating frequencies (AltiKa (Verron et al., 2015)).

5.3.3 Developing a CryoSat-2 based retrieval of Greenland Ice Sheet ablation

In Chapter 4, I derived seasonal elevation changes driven by melting and snowfall in the ablation zone of the Greenland Ice Sheet from CryoSat-2 altimetry. In this section, I investigate the potential of using these data to estimate the ablation of the Greenland Ice Sheet using remote sensing. The runoff of surface meltwater is the main driver of recent Greenland Ice Sheet imbalance (Enderlin et al., 2014; van den Broeke et al., 2016) and an important indicator of its response to climate change. Due to a paucity of in situ measurements, regional-scale estimates of ablation are typically derived from regional climate models (Fettweis et al., 2017; Lucas-Picher et al., 2012; Noël et al., 2018); the development of remotely sensed estimates of ice sheet ablation will provide new observations with which regional climate models can be evaluated against. In recent years the production of surface meltwater (runoff) on the Greenland Ice Sheet has increased in response to Arctic warming (Trusel et al., 2018), raising global sea levels and accounting for 60 % of the total ice loss between 1991 and 2015 (Enderlin et al., 2014; van den Broeke et al., 2016). Knowledge of Greenland runoff is required to quantify freshwater input into coastal waters (Bamber et al., 2012; Sejr et al., 2017), which suppresses deep water convection (Böning et al., 2016) and the strength of the Atlantic meridional overturning circulation (Rahmstorf et al., 2015; Swingedouw et al., 2013). Meltwater generated at the surface flows under gravity in a network of supraglacial streams (Smith et al., 2015) and can reach the ice sheet bed through moulins and crevasses, where it may affect ice flow (Palmer et al., 2011; Schoof, 2010; Sundal et al., 2011; Tedstone et al., 2015; Zwally et al., 2002). The total melting is representative of the ice sheet energy balance (van den Broeke et al., 2011); understanding the response of the Greenland Ice Sheet to climatic forcing is required in order to predict sea level rise and freshwater fluxes with confidence (Golledge et al., 2019; Lenaerts et al., 2015).

To explore the ability of CryoSat-2 to monitor runoff from the Greenland Ice Sheet, I converted the time series of elevation change developed in Chapter 4 to estimates of mass change. In the ablation zone, where there is no firn layer, I assume mass change in the summer months occurs as a result of either ice dynamical processes or the melting of ice. Before spatially aggregating the elevation time series, I classify and remove areas of ice dynamical imbalance where CryoSat-2 rates of elevation change between

2011 and 2017 exceed (by more than 0.5 m/yr) rates of elevation change due to surface processes alone (Chapter 4, Figure 4.1). These areas are coincident with observations of fast ice flow at several outlet glaciers during our study period (Joughin et al., 2014; Kehrl et al., 2017; Larsen et al., 2016; Lemos et al., 2018; Moon et al., 2015). Elsewhere, I assume that elevation changes during the summer are driven by surface melting; as a first attempt I convert the resulting volume changes to mass using an ice density of 917 kg/m^3 (Figure 5.4). Because CryoSat-2 does not fully sample the ablation zone during its 30 day sub-cycle, I scale the monthly estimates of mass change according to the proportion of the observed area (40 % of the ablation zone) as an initial approximation of the regional change.

From these early results, I estimate the ablation zone of the Greenland Ice Sheet lost 1861 Gt of ice due to surface melting between 2011 and 2018 (Figure 5.6). Annual runoff peaked at 368 Gt in 2012, during an exceptionally warm summer which saw widespread surface melting across much of the ice sheet (Hanna et al., 2014; Nghiem et al., 2012; Tedesco et al., 2013). In the following year runoff reduced dramatically (227 Gt), as an abrupt shift to a positive phase in the North Atlantic Oscillation (NAO) brought about cooler atmospheric conditions (Bevis et al., 2019). These conditions persisted until 2015 when the NAO returned to negative phase; between 2015 and 2018 runoff increased year-on-year to 282 Gt in 2017.

I evaluate the initial estimates of mass change due to surface melt water runoff using modelled estimates from the RACMO2.3p2 regional climate model, downscaled to a resolution of 1 km (Noël et al., 2018). Runoff in the Greenland Ice Sheet ablation zone was estimated using cumulative anomalies, relative to the 1960-1980 average. Comparing these independent runoff estimates (Figure 5.7) there is good agreement between the cumulative monthly estimates across the ice sheet ablation zone ($R = 0.99$) and the long term trends.

These early results are a promising demonstration of using CryoSat-2 altimetry to monitor ice sheet runoff for the first time. These remotely sensed observations can be used to evaluate regional climate models and understand changes in freshwater flux and ice flow. Because regional climate models are forced by climate re-analyses and

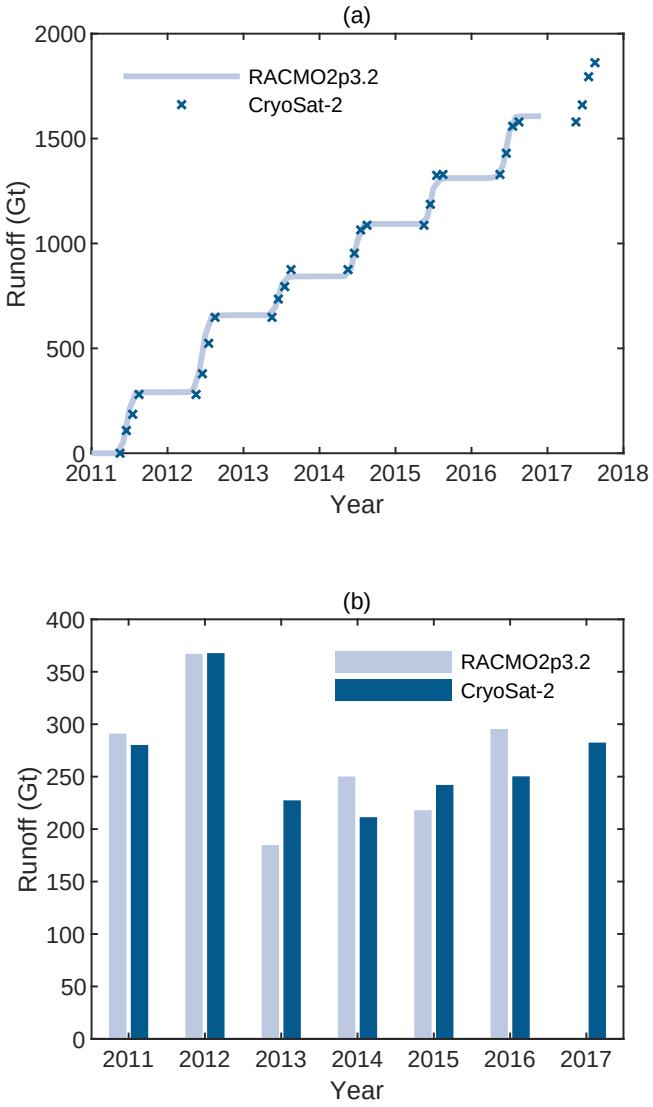

Figure 5.6: (a) Cumulative and (b) annual estimates of runoff between 2011 and 2018 in the ablation zone of the Greenland Ice Sheet from CryoSat-2 altimetry (dark) and regional climate modelling (light).

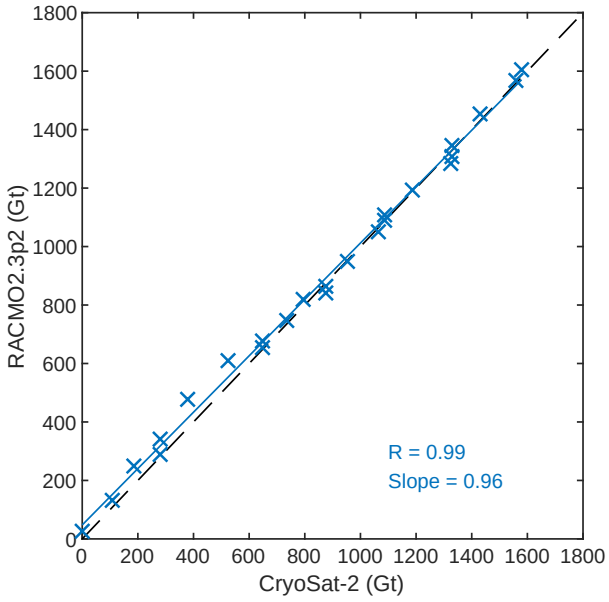

Figure 5.7: Correspondence between cumulative monthly estimates of runoff between 2011 and 2017 in the ablation zone of the Greenland Ice Sheet from CryoSat-2 altimetry and RACMO2.3p2 regional climate modelling. Also shown is a linear regression (solid blue line), the regression slope and correlation coefficient R. The dashed line indicates equivalence.

outputs typically lag a year behind, CryoSat-2 observations can be used to provide up to date, monthly runoff measurements before modelled estimates are available (Figure 5.6). In future, these results can be further improved by extending the time series to the present day and considering the uncertainties introduced by the assumptions used here to account for (1) the effects of ice dynamics on the elevation change signal (2) the volume to mass conversion and (3) the monthly sampling of CryoSat-2. Furthermore, this analysis can be partitioned in order to examine ice sheet runoff within individual ice sheet drainage basins. Such information would be beneficial in understanding the effects of meltwater availability on local variations in glacier flow (e.g (Khazendar et al., 2019)).

5.4 Concluding remarks

Over the past 25 years, satellite radar altimeters have transformed our understanding of the Antarctic and Greenland ice sheets. Measurements of ice sheet surface elevation change have resolved detailed patterns of thinning due to ice dynamical imbalance within individual glacier catchments (e.g. (Flament and Rémy, 2012; Konrad et al., 2017; Shepherd et al., 2001)) and surface melting in response to atmospheric warming (e.g. (Helm et al., 2014; McMillan et al., 2016; Sandberg Sørensen et al., 2018)). Ice losses from Antarctica and Greenland will continue in response to anthropogenic climate change, raise global sea levels (Shepherd et al., 2012), influence oceanic circulation (Caesar et al., 2018) and enhance global temperature variability (Golledge et al., 2019). Continued satellite observations are vital in monitoring contemporary ice sheet losses and evaluating models on which projections of the future are based; the methods and datasets I have developed in this thesis can be used to help achieve these objectives, by contributing towards improved ice sheet elevation and elevation change measurements from satellite radar altimetry. While the focus of this thesis has been upon the CryoSat-2 mission, these methods can be applied to both recently launched and historical radar altimeter missions, ensuring that they have considerable relevance in the future.

References

Agosta, C., Amory, C., Kittel, C., Orsi, A., Favier, V., Gallée, H., van den Broeke, M. R., Lenaerts, J. T. M., van Wessem, J. M., van de Berg, W. J., and Fettweis, X. (2019). Estimation of the Antarctic surface mass balance using the regional climate model MAR (1979–2015) and identification of dominant processes. *The Cryosphere*, 13(1):281–296. 126

Armitage, T. W. K., Wingham, D. J., and Ridout, A. L. (2014). Meteorological origin of the static crossover pattern present in low-resolution-mode CryoSat-2 data over central Antarctica. *IEEE Geoscience and Remote Sensing Letters*, 11(7):1295–1299. 122, 133

Arthern, R. J., Wingham, D. J., and Ridout, A. L. (2001). Controls on ERS altimeter measurements over ice sheets: Footprint-scale topography, backscatter fluctuations, and the dependence of microwave penetration depth on satellite orientation. *Journal of Geophysical Research: Atmospheres*, 106(D24):33471–33484. 122, 132

Bamber, J., van den Broeke, M., Ettema, J., Lenaerts, J., and Rignot, E. (2012). Recent large increases in freshwater fluxes from Greenland into the North Atlantic. *Geophysical Research Letters*, 39(19). 134

Bamber, J. L., Gomez-Dans, J. L., and Griggs, J. A. (2009). A new 1 km Digital Elevation Model of the Antarctic derived from combined satellite radar and laser data – Part 1: Data and methods. *The Cryosphere*, 3(1):101–111. 121, 122

Bevis, M., Harig, C., Khan, S. A., Brown, A., Simons, F. J., Willis, M., Fettweis, X., van den Broeke, M. R., Madsen, F. B., Kendrick, E., Caccamise, D. J., van Dam, T., Knudsen, P., and Nylen, T. (2019). Accelerating changes in ice mass within

Greenland, and the ice sheet's sensitivity to atmospheric forcing. *Proceedings of the National Academy of Sciences*, page 201806562. 125, 135

Böning, C. W., Behrens, E., Biastoch, A., Getzlaff, K., and Bamber, J. L. (2016). Emerging impact of Greenland meltwater on deepwater formation in the North Atlantic Ocean. *Nature Geoscience*, 9:523. 134

Caesar, L., Rahmstorf, S., Robinson, A., Feulner, G., and Saba, V. (2018). Observed fingerprint of a weakening Atlantic Ocean overturning circulation. *Nature*, 556(7700):191–196. 138

Church, J., Clark, P., Cazenave, A., Gregory, J., Jevrejeva, S., Levermann, A., Merrifield, M., Milne, G., Nerem, R., Nunn, P., Payne, A., Pfeffer, W., Stammer, D., and Unnikrishnan, A. (2013). *Sea Level Change*, book section 13, page 1137–1216. Cambridge University Press, Cambridge, United Kingdom and New York, NY, USA. xvii, xviii, 127, 128, 129

Cornford, S. L., Martin, D. F., Graves, D. T., Ranken, D. F., Le Brocq, A. M., Gladstone, R. M., Payne, A. J., Ng, E. G., and Lipscomb, W. H. (2013). Adaptive mesh, finite volume modeling of marine ice sheets. *Journal of Computational Physics*, 232(1):529–549. 126

Cornford, S. L., Martin, D. F., Payne, A. J., Ng, E. G., Le Brocq, A. M., Gladstone, R. M., Edwards, T. L., Shannon, S. R., Agosta, C., van den Broeke, M. R., Hellmer, H. H., Krinner, G., Ligtenberg, S. R. M., Timmermann, R., and Vaughan, D. G. (2015). Century-scale simulations of the response of the West Antarctic Ice Sheet to a warming climate. *The Cryosphere*, 9(4):1579–1600. 121, 129

Davis, C. H. and Ferguson, A. C. (2004). Elevation change of the Antarctic ice sheet, 1995-2000, from ERS-2 satellite radar altimetry. *IEEE Transactions on Geoscience and Remote Sensing*, 42(11):2437–2445. 123, 126, 132

Davis, C. H. and Zwally, H. J. (1993). Geographic and seasonal variations in the surface properties of the ice sheets by satellite-radar altimetry. *Journal of Glaciology*, 39(133):687–697. 122

Enderlin, E. M., Howat, I. M., Jeong, S., Noh, M.-J., Angelen, J. H., and Broeke, M. R. (2014). An improved mass budget for the Greenland Ice Sheet. *Geophysical Research Letters*, 41(3):866–872. 134

Fettweis, X., Box, J. E., Agosta, C., Amory, C., Kittel, C., Lang, C., van As, D., Machguth, H., and Gallée, H. (2017). Reconstructions of the 1900–2015 Greenland Ice Sheet surface mass balance using the regional climate MAR model. *The Cryosphere*, 11(2):1015–1033. 134

Fettweis, X., Hanna, E., Lang, C., Belleflamme, A., Erpicum, M., and Gallée, H. (2013). Brief communication: Important role of the mid-tropospheric atmospheric circulation in the recent surface melt increase over the Greenland ice sheet. *The Cryosphere*, 7(1):241–248. 122

Flament, T. and Rémy, F. (2012). Dynamic thinning of Antarctic glaciers from along-track repeat radar altimetry. *Journal of Glaciology*, 58(211):830–840. 138

Fretwell, P., Pritchard, H. D., Vaughan, D. G., Bamber, J. L., Barrand, N. E., Bell, R., Bianchi, C., Bingham, R. G., Blankenship, D. D., Casassa, G., Catania, G., Callens, D., Conway, H., Cook, A. J., Corr, H. F. J., Damaske, D., Damm, V., Ferraccioli, F., Forsberg, R., Fujita, S., Gim, Y., Gogineni, P., Griggs, J. A., Hindmarsh, R. C. A., Holmlund, P., Holt, J. W., Jacobel, R. W., Jenkins, A., Jokat, W., Jordan, T., King, E. C., Kohler, J., Krabill, W., Riger-Kusk, M., Langley, K. A., Leitchenkov, G., Leuschen, C., Luyendyk, B. P., Matsuoka, K., Mouginot, J., Nitsche, F. O., Nogi, Y., Nost, O. A., Popov, S. V., Rignot, E., Rippin, D. M., Rivera, A., Roberts, J., Ross, N., Siegert, M. J., Smith, A. M., Steinhage, D., Studinger, M., Sun, B., Tinto, B. K., Welch, B. C., Wilson, D., Young, D. A., Xiangbin, C., and Zirizzotti, A. (2013). Bedmap2: improved ice bed, surface and thickness datasets for Antarctica. *The Cryosphere*, 7(1):375–393. 122

Golledge, N. R., Keller, E. D., Gomez, N., Naughten, K. A., Bernales, J., Trusel, L. D., and Edwards, T. L. (2019). Global environmental consequences of twenty-first-century ice-sheet melt. *Nature*, 566(7742):65–72. 134, 138

Gourmelen, N., Escorihuela, M. J., Shepherd, A., Foresta, L., Muir, A., Garcia-Mondéjar, A., Roca, M., Baker, S. G., and Drinkwater, M. R. (2018). CryoSat-2

swath interferometric altimetry for mapping ice elevation and elevation change. *Advances in Space Research*, 62(6):1226–1242. xviii, 131, 132

Hanna, E., Fettweis, X., Mernild, S. H., Cappelen, J., Ribergaard, M. H., Shuman, C. A., Steffen, K., Wood, L., and Mote, T. L. (2014). Atmospheric and oceanic climate forcing of the exceptional Greenland Ice Sheet surface melt in summer 2012. *International Journal of Climatology*, 34(4):1022–1037. 125, 135

Helm, V., Humbert, A., and Miller, H. (2014). Elevation and elevation change of Greenland and Antarctica derived from CryoSat-2. *The Cryosphere*, 8(4):1539–1559. 120, 121, 122, 138

Helsen, M. M., van den Broeke, M. R., van de Wal, R. S. W., van de Berg, W. J., van Meijgaard, E., Davis, C. H., Li, Y., and Goodwin, I. (2008). Elevation changes in Antarctica mainly determined by accumulation variability. *Science*, 320(5883):1626. 121

Joughin, I., Smith, B. E., Shean, D. E., and Floricioiu, D. (2014). Brief communication: Further summer speedup of Jakobshavn Isbræ. *The Cryosphere*, 8(1):209–214. 124, 135

Kehrl, L. M., Joughin, I., Shean, D. E., Floricioiu, D., and Krieger, L. (2017). Seasonal and interannual variabilities in terminus position, glacier velocity, and surface elevation at Helheim and Kangerlussuaq Glaciers from 2008 to 2016. *Journal of Geophysical Research: Earth Surface*, 122(9):1635–1652. 124, 135

Khan, S. A., Kjær, K. H., Bevis, M., Bamber, J. L., Wahr, J., Kjeldsen, K. K., Bjørk, A. A., Korsgaard, N. J., Stearns, L. A., van den Broeke, M. R., Liu, L., Larsen, N. K., and Muresan, I. S. (2014). Sustained mass loss of the northeast Greenland Ice Sheet triggered by regional warming. *Nature Climate Change*, 4:292. 125

Khazendar, A., Fenty, I. G., Carroll, D., Gardner, A., Lee, C. M., Fukumori, I., Wang, O., Zhang, H., Seroussi, H., Moller, D., Noël, B. P. Y., van den Broeke, M. R., Dinardo, S., and Willis, J. (2019). Interruption of two decades of Jakobshavn Isbræ acceleration and thinning as regional ocean cools. *Nature Geoscience*, 12(4):277–283. 137

Khvorostovsky, K. S. (2012). Merging and analysis of elevation time series over Greenland ice sheet from satellite radar altimetry. *IEEE Transactions on Geoscience and Remote Sensing*, 50(1):23–36. 126

Konrad, H., Gilbert, L., Cornford, S. L., Payne, A., Hogg, A., Muir, A., and Shepherd, A. (2017). Uneven onset and pace of ice-dynamical imbalance in the Amundsen Sea Embayment, West Antarctica. *Geophysical Research Letters*, 44(2):910–918. 138

Krabill, W. B. (2016). IceBridge ATM L2 Icessn elevation, slope and roughness version 2, National Snow and Ice Data Center, Boulder, Colorado, USA, available at: https://nsidc.org/icebridge/portal/ (last access January 2017). 121

Kuipers Munneke, P., Ligtenberg, S. R. M., Noël, B. P. Y., Howat, I. M., Box, J. E., Mosley-Thompson, E., McConnell, J. R., Steffen, K., Harper, J. T., Das, S. B., and van den Broeke, M. R. (2015). Elevation change of the Greenland Ice Sheet due to surface mass balance and firn processes, 1960–2014. *The Cryosphere*, 9(6):2009–2025. 124

Larsen, S. H., Khan, S. A., Ahlstrøm, A. P., Hvidberg, C. S., Willis, M. J., and Andersen, S. B. (2016). Increased mass loss and asynchronous behavior of marine-terminating outlet glaciers at Upernavik Isstrøm, NW Greenland. *Journal of Geophysical Research: Earth Surface*, 121(2):241–256. 124, 135

Lemos, A., Shepherd, A., McMillan, M., Hogg, A. E., Hatton, E., and Joughin, I. (2018). Ice velocity of Jakobshavn Isbræ, Petermann Glacier, Nioghalvfjerdsfjorden, and Zachariæ isstrøm, 2015–2017, from Sentinel 1-a/b SAR imagery. *The Cryosphere*, 12(6):2087–2097. 124, 135

Lenaerts, J. T. M., Le Bars, D., van Kampenhout, L., Vizcaino, M., Enderlin, E. M., and van den Broeke, M. R. (2015). Representing Greenland Ice Sheet freshwater fluxes in climate models. *Geophysical Research Letters*, 42(15):6373–6381. 134

Ligtenberg, S., Helsen, M. M., and van den Broeke, M. R. (2011). An improved semi-empirical model for the densification of Antarctic firn. *The Cryosphere*, 5(4):809–819. 124

Ligtenberg, S., Kuipers Munneke, P., Noël, B. P. Y., and van den Broeke, M. R. (2018). Brief communication: Improved simulation of the present-day Greenland firn layer (1960–2016). *The Cryosphere*, 12(5):1643–1649. 124

Lucas-Picher, P., Wulff-Nielsen, M., Christensen, J. H., Aðalgeirsdóttir, G., Mottram, R., and Simonsen, S. B. (2012). Very high resolution regional climate model simulations over Greenland: Identifying added value. *Journal of Geophysical Research: Atmospheres*, 117(D2). 134

Markus, T., Neumann, T., Martino, A., Abdalati, W., Brunt, K., Csatho, B., Farrell, S., Fricker, H., Gardner, A., Harding, D., Jasinski, M., Kwok, R., Magruder, L., Lubin, D., Luthcke, S., Morison, J., Nelson, R., Neuenschwander, A., Palm, S., Popescu, S., Shum, C. K., Schutz, B. E., Smith, B., Yang, Y., and Zwally, J. (2017). The Ice, Cloud, and land Elevation Satellite-2 (ICESat-2): Science requirements, concept, and implementation. *Remote Sensing of Environment*, 190:260–273. 132

Matzler, C. (1996). Microwave permittivity of dry snow. *IEEE Transactions on Geoscience and Remote Sensing*, 34(2):573–581. 122

McMillan, M., Leeson, A., Shepherd, A., Briggs, K., Armitage, T. W. K., Hogg, A., Kuipers Munneke, P., van den Broeke, M., Noël, B., van de Berg, W. J., Ligtenberg, S., Horwath, M., Groh, A., Muir, A., and Gilbert, L. (2016). A high-resolution record of Greenland mass balance. *Geophysical Research Letters*, 43(13):7002–7010. 123, 129, 138

McMillan, M., Muir, A., Shepherd, A., Escolà, R., Roca, M., Aublanc, J., Thibaut, P., Restano, M., Ambrozio, A., and Benveniste, J. (2019). Sentinel-3 delay-doppler altimetry over Antarctica. *The Cryosphere*, 13(2):709–722. 132, 133

McMillan, M., Shepherd, A., Sundal, A., Briggs, K., Muir, A., Ridout, A., Hogg, A., and Wingham, D. (2014). Increased ice losses from Antarctica detected by CryoSat-2. *Geophysical Research Letters*, 41(11):3899–3905. 129, 132

Moon, T., Joughin, I., and Smith, B. (2015). Seasonal to multiyear variability of glacier surface velocity, terminus position, and sea ice/ice mélange in northwest Greenland. *Journal of Geophysical Research: Earth Surface*, 120(5):818–833. 125, 135

Mote, T. L. (2007). Greenland surface melt trends 1973–2007: Evidence of a large increase in 2007. *Geophysical Research Letters*, 34(22). 122

Mouginot, J., Rignot, E., Bjørk, A. A., van den Broeke, M., Millan, R., Morlighem, M., Noël, B., Scheuchl, B., and Wood, M. (2019). Forty-six years of Greenland Ice Sheet mass balance from 1972 to 2018. *Proceedings of the National Academy of Sciences*, page 201904242. 126

Mouginot, J., Rignot, E., Scheuchl, B., Fenty, I., Khazendar, A., Morlighem, M., Buzzi, A., and Paden, J. (2015). Fast retreat of Zachariæ Isstrøm, northeast Greenland. *Science*, 350(6266):1357–1361. 124

Mouginot, J., Scheuchl, B., and Rignot, E. (2012). Mapping of ice motion in Antarctica using Synthetic-Aperture Radar data. *Remote Sensing*, 4(9):2753–2767. 121

Nghiem, S. V., Hall, D. K., Mote, T. L., Tedesco, M., Albert, M. R., Keegan, K., Shuman, C. A., DiGirolamo, N. E., and Neumann, G. (2012). The extreme melt across the Greenland ice sheet in 2012. *Geophysical Research Letters*, 39(20). 122, 125, 135

Nias, I. J., Cornford, S. L., and Payne, A. J. (2018). New mass-conserving bedrock topography for Pine Island Glacier impacts simulated decadal rates of mass loss. *Geophysical Research Letters*, 45(7):3173–3181. 126

Nilsson, J., Gardner, A., Sandberg Sørensen, L., and Forsberg, R. (2016). Improved retrieval of land ice topography from CryoSat-2 data and its impact for volume-change estimation of the Greenland ice sheet. *The Cryosphere*, 10(6):2953–2969. 123

Nilsson, J., Vallelonga, P., Simonsen, S. B., Sørensen, L. S., Forsberg, R., Dahl-Jensen, D., Hirabayashi, M., Goto-Azuma, K., Hvidberg, C. S., Kjaer, H. A., and Satow, K. (2015). Greenland 2012 melt event effects on CryoSat-2 radar altimetry. *Geophysical Research Letters*, 42(10):3919–3926. 122, 123, 126, 132

Noël, B., van de Berg, W. J., van Wessem, J. M., van Meijgaard, E., van As, D., Lenaerts, J. T. M., Lhermitte, S., Kuipers Munneke, P., Smeets, C. J. P. P., van Ulft, L. H., van de Wal, R. S. W., and van den Broeke, M. R. (2018). Modelling

the climate and surface mass balance of polar ice sheets using RACMO2 – Part 1: Greenland (1958–2016). *The Cryosphere*, 12(3):811–831. 129, 134, 135

Palmer, S., Shepherd, A., Nienow, P., and Joughin, I. (2011). Seasonal speedup of the Greenland Ice Sheet linked to routing of surface water. *Earth and Planetary Science Letters*, 302(3):423–428. 134

Pattyn, F., Perichon, L., Durand, G., Favier, L., Gagliardini, O., Hindmarsh, R. C. A., Zwinger, T., Albrecht, T., Cornford, S., Docquier, D., Fürst, J. J., Goldberg, D., Gudmundsson, G. H., Humbert, A., Hütten, M., Huybrechts, P., Jouvet, G., Kleiner, T., Larour, E., Martin, D., Morlighem, M., Payne, A. J., Pollard, D., Rückamp, M., Rybak, O., Seroussi, H., Thoma, M., and Wilkens, N. (2013). Grounding-line migration in plan-view marine ice-sheet models: results of the ice2sea MISMIP3d intercomparison. *Journal of Glaciology*, 59(215):410–422. 126

Pritchard, H. D., Arthern, R. J., Vaughan, D. G., and Edwards, L. A. (2009). Extensive dynamic thinning on the margins of the Greenland and Antarctic ice sheets. *Nature*, 461:971. 129

Rahmstorf, S., Box, J. E., Feulner, G., Mann, M. E., Robinson, A., Rutherford, S., and Schaffernicht, E. J. (2015). Exceptional twentieth-century slowdown in Atlantic Ocean overturning circulation. *Nature Climate Change*, 5:475. 134

Ridley, J. K. and Partington, K. C. (1988). A model of satellite radar altimeter return from ice sheets. *International Journal of Remote Sensing*, 9(4):601–624. 122

Rignot, E., Bamber, J. L., van den Broeke, M. R., Davis, C., Li, Y., van de Berg, W. J., and van Meijgaard, E. (2008). Recent Antarctic ice mass loss from radar interferometry and regional climate modelling. *Nature Geoscience*, 1(2):106–110. 121

Rignot, E., Mouginot, J., and Scheuchl, B. (2011). Ice flow of the Antarctic Ice Sheet. *Science*, 333(6048):1427. 121

Rignot, E., Mouginot, J., Scheuchl, B., van den Broeke, M., van Wessem, M. J., and Morlighem, M. (2019). Four decades of Antarctic Ice Sheet mass balance from 1979–2017. *Proceedings of the National Academy of Sciences*, page 201812883. 126

Ritz, C., Edwards, T. L., Durand, G., Payne, A. J., Peyaud, V., and Hindmarsh, R. C. (2015). Potential sea-level rise from Antarctic ice-sheet instability constrained by observations. *Nature*, 528(7580):115–8. 121

Roemer, S., Legrésy, B., Horwath, M., and Dietrich, R. (2007). Refined analysis of radar altimetry data applied to the region of the subglacial Lake Vostok/Antarctica. *Remote Sensing of Environment*, 106(3):269–284. 126

Sandberg Sørensen, L., Simonsen, S. B., Forsberg, R., Khvorostovsky, K., Meister, R., and Engdahl, M. E. (2018). 25 years of elevation changes of the Greenland ice sheet from ERS, Envisat, and CryoSat-2 radar altimetry. *Earth and Planetary Science Letters*, 495:234–241. 123, 138

Schoof, C. (2010). Ice-sheet acceleration driven by melt supply variability. *Nature*, 468:803. 134

Schröder, L., Horwath, M., Dietrich, R., Helm, V., van den Broeke, M. R., and Ligtenberg, S. R. M. (2019). Four decades of Antarctic surface elevation changes from multi-mission satellite altimetry. *The Cryosphere*, 13(2):427–449. 129

Sejr, M. K., Stedmon, C. A., Bendtsen, J., Abermann, J., Juul-Pedersen, T., Mortensen, J., and Rysgaard, S. (2017). Evidence of local and regional freshening of Northeast Greenland coastal waters. *Scientific Reports*, 7(1):13183. 134

Shepherd, A., Gilbert, L., Muir, A. S., Konrad, H., McMillan, M., Slater, T., Briggs, K. H., Sundal, A. V., Hogg, A. E., and Engdahl, M. (2019). Trends in Antarctic Ice Sheet elevation and mass. *Geophysical Research Letters*. 129

Shepherd, A., Ivins, E. R., A, G., Barletta, V. R., Bentley, M. J., Bettadpur, S., Briggs, K. H., Bromwich, D. H., Forsberg, R., Galin, N., Horwath, M., Jacobs, S., Joughin, I., King, M. A., Lenaerts, J. T. M., Li, J., Ligtenberg, S. R. M., Luckman, A., Luthcke, S. B., McMillan, M., Meister, R., Milne, G., Mouginot, J., Muir, A., Nicolas, J. P., Paden, J., Payne, A. J., Pritchard, H., Rignot, E., Rott, H., Sørensen, L. S., Scambos, T. A., Scheuchl, B., Schrama, E. J. O., Smith, B., Sundal, A. V., van Angelen, J. H., van de Berg, W. J., van den Broeke, M. R., Vaughan, D. G., Velicogna, I., Wahr, J., Whitehouse, P. L., Wingham, D. J., Yi, D., Young, D.,

and Zwally, H. J. (2012). A reconciled estimate of ice-sheet mass balance. *Science*, 338(6111):1183. 129, 138

Shepherd, A. and Nowicki, S. (2017). Improvements in ice-sheet sea-level projections. *Nature Climate Change*, 7(10):672–674. 129

Shepherd, A., Wingham, D. J., Mansley, J. A. D., and Corr, H. F. J. (2001). Inland thinning of Pine Island Glacier, West Antarctica. *Science*, 291(5505):862–864. 138

Simonsen, S. B. and Sørensen, L. S. (2017). Implications of changing scattering properties on Greenland ice sheet volume change from CryoSat-2 altimetry. *Remote Sensing of Environment*, 190:207–216. 123

Slater, T. and Shepherd, A. (2018). Antarctic ice losses tracking high. *Nature Climate Change*. xvii, 126, 127, 129

Smith, L. C., Chu, V. W., Yang, K., Gleason, C. J., Pitcher, L. H., Rennermalm, A. K., Legleiter, C. J., Behar, A. E., Overstreet, B. T., Moustafa, S. E., Tedesco, M., Forster, R. R., LeWinter, A. L., Finnegan, D. C., Sheng, Y., and Balog, J. (2015). Efficient meltwater drainage through supraglacial streams and rivers on the southwest Greenland Ice Sheet. *Proceedings of the National Academy of Sciences*, 112(4):1001. 134

Studinger, M. (2014). Icebridge ATM L4 surface elevation rate of change, Version 1, National Snow and Ice Data Center, Boulder, Colorado, USA, available at: https://nsidc.org/icebridge/portal/ (last access January 2019). 124

Sundal, A. V., Shepherd, A., Nienow, P., Hanna, E., Palmer, S., and Huybrechts, P. (2011). Melt-induced speed-up of Greenland Ice Sheet offset by efficient subglacial drainage. *Nature*, 469(7331):521–4. 125, 134

Swingedouw, D., Rodehacke, C. B., Behrens, E., Menary, M., Olsen, S. M., Gao, Y., Mikolajewicz, U., Mignot, J., and Biastoch, A. (2013). Decadal fingerprints of freshwater discharge around Greenland in a multi-model ensemble. *Climate Dynamics*, 41(3):695–720. 134

Tedesco, M., Fettweis, X., Mote, T., Wahr, J., Alexander, P., Box, J. E., and Wouters, B. (2013). Evidence and analysis of 2012 Greenland records from spaceborne observations, a regional climate model and reanalysis data. *The Cryosphere*, 7(2):615–630. 125, 135

Tedstone, A. J., Nienow, P. W., Gourmelen, N., Dehecq, A., Goldberg, D., and Hanna, E. (2015). Decadal slowdown of a land-terminating sector of the Greenland Ice Sheet despite warming. *Nature*, 526:692. 125, 134

The IMBIE Team (2018). Mass balance of the Antarctic Ice Sheet from 1992 to 2017. *Nature*, 558(7709):219–222. xvii, 127, 129

Trusel, L. D., Das, S. B., Osman, M. B., Evans, M. J., Smith, B. E., Fettweis, X., McConnell, J. R., Noël, B. P. Y., and van den Broeke, M. R. (2018). Nonlinear rise in Greenland runoff in response to post-industrial Arctic warming. *Nature*, 564(7734):104–108. 134

van den Broeke, M., Enderlin, E. M., Howat, I. M., Kuipers Munneke, P., Noël, B. P. Y., van de Berg, W. J., van Meijgaard, E., and Wouters, B. (2016). On the recent contribution of the Greenland Ice Sheet to sea level change. *The Cryosphere*, 10(5):1933–1946. 134

van den Broeke, M., Smeets, C. J. P. P., and van de Wal, R. S. W. (2011). The seasonal cycle and interannual variability of surface energy balance and melt in the ablation zone of the west Greenland Ice Sheet. *The Cryosphere*, 5(2):377–390. 134

van Wessem, J. M., van de Berg, W. J., Noël, B. P. Y., van Meijgaard, E., Amory, C., Birnbaum, G., Jakobs, C. L., Krüger, K., Lenaerts, J. T. M., Lhermitte, S., Ligtenberg, S. R. M., Medley, B., Reijmer, C. H., van Tricht, K., Trusel, L. D., van Ulft, L. H., Wouters, B., Wuite, J., and van den Broeke, M. R. (2018). Modelling the climate and surface mass balance of polar ice sheets using RACMO2 – Part 2: Antarctica (1979–2016). *The Cryosphere*, 12(4):1479–1498. 126, 129

Verron, J., Sengenes, P., Lambin, J., Noubel, J., Steunou, N., Guillot, A., Picot, N., Coutin-Faye, S., Sharma, R., Gairola, R. M., Murthy, D. V. A. R., Richman, J. G., Griffin, D., Pascual, A., Rémy, F., and Gupta, P. K. (2015). The SARAL/AltiKa altimetry satellite mission. *Marine Geodesy*, 38(sup1):2–21. 132, 133

Wingham, D. J., Ridout, A. J., Scharroo, R., Arthern, R. J., and Shum, C. K. (1998). Antarctic elevation change from 1992 to 1996. *Science*, 282(5388):456–458. 123, 129, 132

Zwally, H. J., Abdalati, W., Herring, T., Larson, K., Saba, J., and Steffen, K. (2002). Surface melt-induced acceleration of Greenland Ice Sheet flow. *Science*, 297(5579):218–222. 134